creative commons
COMMONS DEED

저작자표시-비영리-변경금지 2.0 대한민국

이용자는 아래의 조건을 따르는 경우에 한하여 자유롭게

- 이 저작물을 복제, 배포, 전송, 전시, 공연 및 방송할 수 있습니다.

다음과 같은 조건을 따라야 합니다:

저작자표시. 귀하는 원저작자를 표시하여야 합니다.

비영리. 귀하는 이 저작물을 영리 목적으로 이용할 수 없습니다.

변경금지. 귀하는 이 저작물을 개작, 변형 또는 가공할 수 없습니다.

- 귀하는, 이 저작물의 재이용이나 배포의 경우, 이 저작물에 적용된 이용허락조건을 명확하게 나타내어야 합니다.
- 저작권자로부터 별도의 허가를 받으면 이러한 조건들은 적용되지 않습니다.

저작권법에 따른 이용자의 권리는 위의 내용에 의하여 영향을 받지 않습니다.

이것은 이용허락규약(Legal Code)을 이해하기 쉽게 요약한 것입니다.

Disclaimer

dCollection

공학박사 학위논문

Circular Dichroism Modulation based on Plasmon Coupling in Chiral Nanostructures

카이랄 나노구조의 플라즈몬 커플링을 기반한 원편광 이색성 변조

2022년 2월

서울대학교 대학원

재료공학부

김 혜 온

Circular Dichroism Modulation based on Plasmon Coupling in Chiral Nanostructures

지도 교수 남 기 태

이 논문을 공학박사 학위논문으로 제출함

2022년 2월

서울대학교 대학원

재료공학부

김 혜 온

김혜온의 박사 학위논문을 인준함

2022년 2월

위 원 장 김 미 영 (인)

부위원장 남 기 태 (인)

위 원 장 호 원 (인)

위 원 유 필 진 (인)

위 원 이 승 우 (인)

Abstract

Circular Dichroism Modulation based on Plasmon Coupling in Chiral Nanostructures

Hyeohn Kim

Department of Materials Science and Engineering

The Graduate School

Seoul National University

Chiral metamaterials have been actively pursued in the field of nanophotonics due to their exceptional light-matter interactions. For decades, numerous attempts have been conducted to fabricate chiral nanostructure using state-of-the-art lithography techniques and molecular-assembly scaffolds. Possessing this geometric property, inorganic metal nanomaterials could exhibit fascinating physical phenomena which was difficult to be achieved in symmetric nanomaterials. Chiral nanostructures have greatly expanded the design to demonstrate chiroptic effects such as a negative refractive index, sensitive chiral sensing, and broad-band circular polarizer. In order to integrate the fascinating properties of chiral metamaterials into practical devices, it is necessary to achieve precisely defined chiral morphologies and chiroptic properties. However, the requirement for expensive facilities, the

complexity of the process, and the limited resolution had restricted the translation of chiral metamaterials into real devices. Therefore, developing flexible methodologies for nanostructure control is important to address these limitations and provide new directions. Through this study, we propose that the diversification of nanoparticle morphology using peptide molecules and further modulation of the optical response utilizing plasmonic coupling of nanostructures can be a promising alternative to solve the above-mentioned limitations. In this thesis, we present a platform that can modulate the chiroptic response using plasmon coupling through understanding and regulation of the development of chiral nanostructures.

Recent study on the colloidal synthesis of plasmonic nanoparticles using biomolecules suggests that nanoparticles with novel morphology and optical property can be achieved by altering molecules, which are chirality encoders, involved during the synthesis. In addition, the optical response of a single plasmonic particle can be amplified and sensitively modulated using plasmon coupling. When several nanoscale plasmonic particles are adjacent to each other, hybridization of particle resonance is induced, which significantly changes the resonance. To establish new strategies for controlling the morphology and chirality of plasmonic nanostructures, we have first studied previous studies on bio-inspired pathways for complex nanostructures, focusing on the inorganic chirality induced by biomolecules in Chapter 2. Importantly, the interactions at the interface between biomolecules and inorganic surfaces provide an important insight into the evolution of chirality through atomic distortion or macroscopic reconstruction. Chapter 3 describes the experimental procedures, and Chapter 4, 5, and 6 describe the understanding and modulation of the chiroptic response from the two perspectives of single nanoparticles and systemic control.

Advances in nanomaterial engineering have enabled the development of colloidal synthesis methods for precise morphological control at the nanoscale. The use of various halide ions, metal ions and organic molecules as adsorbates can control the crystal facet and nanoparticle morphology by passivating the crystal facet with a specific Miller index. In addition, the seed-mediated method can synthesize high-Miller-index crystal facets with high uniformity, and thus is being used as an important strategy for controlling NP morphology. In this thesis, we have provided a broad understanding of the growth and chirality evolution in gold NPs by adjusting the type of additive molecules. We have analyzed the growth pathway and chirality evolution of the γ-glutamylcysteine- (γ-Glu-Cys-) and cysteinylglycine- (Cys-Gly-) directed gold NPs from a crystallographic perspective. Gold NPs developed into a cube-like structure with protruding chiral wings in the presence of γ-Glu-Cys, whereas the NPs synthesized with Cys-Gly exhibited a rhombic dodecahedron-like outline with elliptical cavity structures, showing different chiroptic responses. Through time-dependent analysis, we reported that γ-Glu-Cys and Cys-Gly generate different intermediate morphologies. γ-Glu-Cys induced concave hexoctahedra-shaped intermediate, whereas Cys-Gly showed concave rhombic dodecahedra-shaped intermediate. These results showed that the chiral structure and resulting chiroptic response can be modulated through understanding the interaction between peptides and gold surfaces.

Molecule-directed synthesis of chiral nanostructure has been mainly studied in plasmonic materials, but attempts to synthesize chiral metal oxides that can be used as chiral catalysts due to their catalytic activity has been suggested as a new direction for expanding the application of chiral materials. Existing studies on the synthesis of chiral metal oxide using molecule have been limited to single amino acids, but sequence expansion with peptides is required to understand the chirality evolution and achieve a scalable synthetic strategy. In this thesis, Tyr-Tyr-Cys

tripeptide including tyrosine and cysteine were selected as peptide ligands and the role of peptide in developing chirality in cobalt oxide was explored. Synthesized chiral cobalt oxide nanoparticles showed a g-factor of 0.01 in the UV–visible region. In addition, the 3D conformation of the peptide ligand on the nanoparticle surfaces was identified by 2D NMR spectroscopy analysis. Furthermore, the sequence effect of Tyr-Tyr-Cys developing chiral cobalt oxide was analyzed, demonstrating that the thiol group and carboxyl group of the Tyr-Tyr-Cys ligand played an important role in chirality evolution. This results suggest that the role of the peptides can vary depending on the interacting material, leading to further variability in chiroptical properties.

The optical signal of a single plasmonic particle can be amplified and sensitively controlled using plasmon coupling. When several nanoscale plasmonic particles are adjacent to each other, hybridization of particle resonance occurs, which significantly changes the resonance. In this context, plasmonic coupling which has been mainly studied in achiral plasmon structures, was applied to chiral plasmonic nanoparticles to control chiroptical properties. In this thesis, we demonstrated the fabrication of metamaterial by coating chiral gold nanoparticles on a substrate and depositing a nanoscale plasmonic metal layer. In order to investigate changes in optical properties due to plasmon coupling, transmission-based and diffuse reflectance circular dichroism (CD) spectroscopy were utilized. Through this, it was confirmed that the resonance position, magnitude, and sign of the CD spectrum were changed by plasmon coupling. In addition, the coupled plasmon mode was significantly changed according to the dimension, distance, and refractive index of the nanostructure. Furthermore, synthesis of chiral gold-silica core-shell NPs enables versatile control of the structure and properties of plasmonic nanoparticles, facilitating their application to tailored plasmon coupling.

In conclusion, by understanding the role of peptides in nanoparticle development, CD manipulation has been achieved at the single nanoparticle level. In addition, a methodology for modulating the optical properties of chiral nanostructures using plasmon coupling has been established. We believe the development of versatile methodology for modulation of the chiroptical response in chiral nanostructures ultimately facilitate integration of the chiral metamaterials into practical optical devices.

Keywords: Circular dichroism, plasmon coupling, peptide, gold nanoparticle, cobalt oxide, nano-structure control

Student Number: 2018-38618

Contents

List of Figures

Chapter 1. Introduction

1.1 Chirality in Nature

Chirality is a geometrical concept that describes an object that lacks mirror symmetry. Biological system has a very sophisticated but efficient strategy for the generation of chirality, making it important to understand this for the successful control of chirality in artificial chiral nanostructure fabrication. For instance, helical and spiral structures found in gastropod shells,[1] and *Callophrys rubi* butterfly has a chiral gyroid structure.[2] Complex chiral formation processes in nature involve the combination of chiral molecular units to represent higher-order chirality collectively.[3–9] As a single chiral molecule could function as a central component of chiral macromolecular structure, the chiral center of the molecule can provide a starting point for chirality evolution. Therefore, chiral encoders of various scales can be used to induce a macroscopic structural asymmetry in living organisms.[10] The asymmetry of Drosophila could be a distinctive example of this hierarchical chirality generation in biology. As shown in Figure 1.1, the overall chirality from the cellular level to organs and organism itself was produced by molecular motor myosin 1D, demonstrating the asymmetric behavior to dictate the gradual evolution of chirality in biological system.[11] The chiral interaction between f-actin and myosin 1D mediates a counterclockwise circular gliding of actin filaments, inducing a directional twist of cells, organelles, organisms as a whole body.

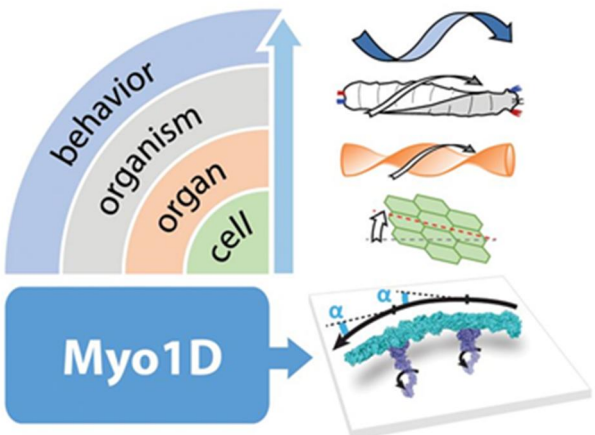

Figure 1.1 Scheme of myo1D chiral activity across multiple organization scales.

This gradual manifestation of chirality in biological features can also be found in the early embryonic stages of the shells of snails and gastropods. Sinistal and dextral *L. stagnalis* embryos have a structure in which they are twisted in opposite directions at an early stage of growth, and develop with opposite rotational patterns in adults. As shown in figure1.2, the mirror-symmetric feature between the dextral and sinistral embryo appears most prominently in cleavage pattern from the 4-cell to the 8-cell stage.[12] To be specific, the directionality in embryo stage, which dextral embryos show clockwise rotation and sinistral embryos show anticlockwise rotation, determines the handedness of adult snails. From the development of hierarchical chirality in biological systems, we could obtain valuable lessons.

Representative examples showed that basic components of biological systems such as organic molecules function as crucial building blocks for chiral structures in bigger size scales. It indicates that the hierarchical assembly of chiral components could develop into a macroscopic chirality. Furthermore, the role of organic molecules or biomolecules can serve not only as a chiral building block, but also as a chiral encoder during chirality evolution. This suggest that the organic molecules and biomolecules can a compelling tool to induce a progressive evolution of chiral features.

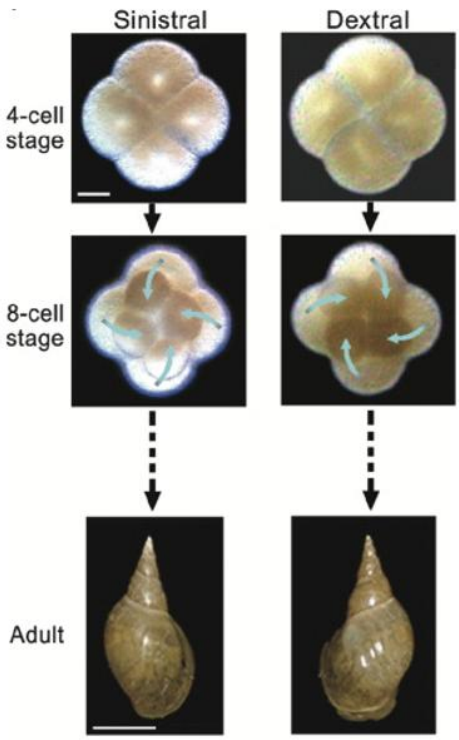

Figure 1.2 Cleavage pattern of the sinistral and dextral *L. stagnalis* embryos and their adult snails.

The chirality in inorganic materials and metals have received less attention compared to the chirality in organic molecules. Determination of chirality in metal and inorganic materials require additional consideration on the position of atomic coordination and planes, whereas in organic molecules, chiral center can be clearly used as a reference point to define the chirality. Therefore, identification of chiral components in metallic and inorganic structures are less straightforward and more difficult than chiral components of organic molecules. However, the interesting property of crystal chirality has attracted attention even before the discovery of chirality in organic molecules. In 1811, different rotation of linearly polarized light was analyzed with the quartz crystals.[13] This study as a starting point, subsequent research directions have expanded from observing and utilizing naturally occurring chiral crystals to controlling and inducing the chirality of crystals, even with those are intrinsically achiral. This field focuses on the study of enantioselective interactions between crystals and chiral organic molecules.

Some of the inorganic crystals which possess helical arrangements along certain crystallographic directions exhibit bulk chirality.[14–18] These crystals which lacks symmetry induce achiral structures, without mirrors, glide planes, an inversion center, and a roto-inversion operator. Although 32 crystallographic point groups exist, only 11 point groups meet this requirement. The most common example is quartz crystal (space group $P3_121$ or $P3_221$). The corner-linked SiO_4 tetrahedra structure is the basic unit of helices. In addition, other inorganic materials such as α-$AlPO_4$ and α-$GaPO_4$ with the tetrahedral phosphate networks also show chirality. Similarly, cinnabar (α-HgS, space group $P3_221$) with crystal structure of helices of repeated Hg and S atoms along the z axis possess chirality (Figure 1.3).[15] This chiral crystals have left- and right-handed variants depending on the orientation of helical atomic arrangements, which occurs in almost equal proportion in nature.

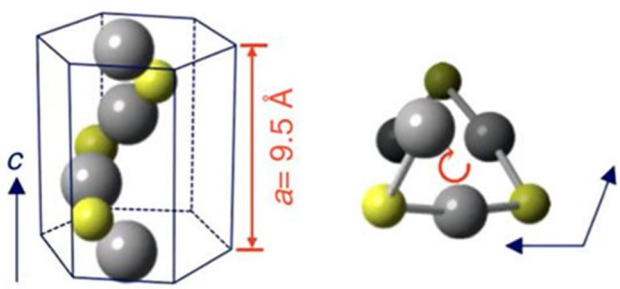

Figure 1.3 Helical arrangement of Hg and S atoms of crystal structure of cinnabar (α-HgS).

Through opposite optical rotation properties or exposed chiral crystal faces of crystal, one can distinguish their handedness. For example, when polarized light passing through the c-axis, the light rotates to the opposite direction depending on the handedness of the quartz, counter-clockwise in left-handed quartz and clockwise in right-handed quartz.[18] However, this relationship between optical rotatory direction and handedness of crystal is not applicable to all chiral crystals. In some cases, opposite relationship could be observed. Another interesting property of crystals with bulk chirality is that the crystal surface structures also contain chirality. While atomic arrangements of crystal faces of quartz are all chiral, some crystal faces such as (111) and (511) facets (Figure 1.4, denoted as *x* and *s* respectively) exhibit observable difference in orientation, with distinguishable left- and right-handed crystals.[16]

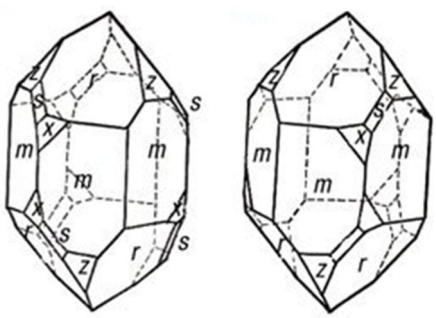

Figure 1.4 Left- and right-handed variants of quartz (SiO_2) crystal. Common crystal surfaces are noted as *m* (100), *r* (101), *s* (111), *x* (511).

1.2 Chiral Plasmonic Nanostructure

Chirality refers geometric property illustrating non-superimposable mirror images of an object with the original structure. These geometric properties are not limited to molecules, but have a wide impact on scientific fields such as chemistry and physics and industries such as pharmaceuticals, medicines, and displays.[19–22] In recent decades, we have developed an understanding of chiral inorganic nanomaterials, which has vastly expanded their applicability in terms of materials, structures and applications. In following section, we will discuss chiral nanomaterials and their unique optical properties, highlighting the need for research on chiral nanostructures.

The geometrical properties of a material's structure can determine the basic properties of a material. Thus, chirality can elicit not only geometrical properties, but also distinct physical properties, especially optical properties. In addition, the symmetry of a material greatly influences its electronic structure, crystallographic surface, chemical bonding, and optical reactivity, and determines the fundamental geometric properties of physical systems. In particular, it is known that chiral structures without mirror symmetry exhibit different responses right- or left-handed circularly polarized light (RCP and LCP). These asymmetric light-matter interactions cause different absorption of RCP and LCP light, resulting in circular dichroism (CD).

Utilizing this circular dichroism, it is possible to obtain the structural, kinetic, and thermodynamic information of materials.[23–25] However, in order to anlyze chirality of naturally existing biomolecules and chiral medium, high concentrations or large volumes of analyte is needed because of their weak chiral optical response. By utilizing plasmonic properties of metallic nanoparticles, we can overcome the issues of the low chirality. The harmonic oscillation in metallic particles concentrates far-field radiation into subwavelength volumes which

indicates a strong light-matter interaction at nano structures. This electric field induced by electron density is dependent on its structures and intrinsic material property as shown in figure 1.5.[26] Difference in shape and material result in distinct optical response which is shown in the color generation of nanoparticle solutions.

As shown in figure 1.7,[27] the sign of polarization state at the end of the circular disk is polarized differently depending on the polarization of the irradiated light. This difference in polarization induces an energy difference, leading to a circular dichroism in the absorption spectrum.

Figure 1.5 Optical properties of gold nanoparticles with different shapes and sizes. Gold nanorods (top), and silica-gold core-shell nanoparticles (bottom).

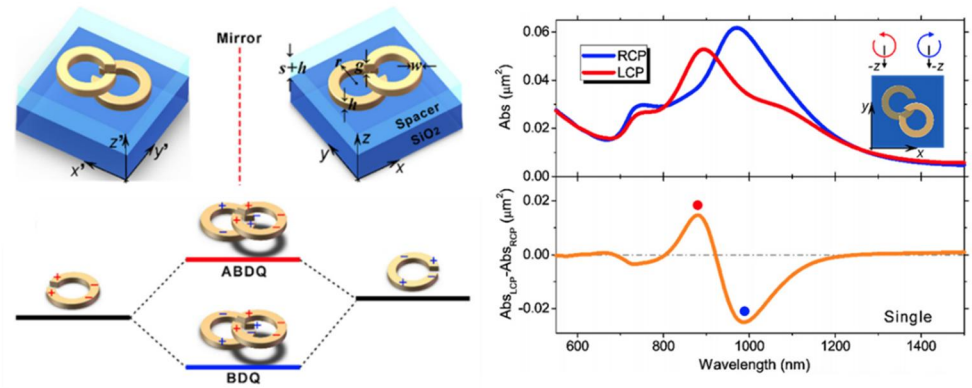

Figure 1.6 Scheme of plasmonic chiral nanodiscs excited by the circularly polarized light. The difference in energy states induces absorption difference between two structures and results in circular dichroism.

Through the above representative examples, it can be seen that the intrinsically chiral plasmon nanostructure can exhibit an exceptional optical response. Studies over the past two decades showed that chiral plasmonic structures can be readily applied to optical applications such as polarization control, negative refractive index, and chiral sensing.[19–22,28,29] As a typical example, the gold helical nanostructure in subwavelength scale exhibits a strong circular dichroism. Figure 1.7 showed that the transmission difference between LCP and RCP dramatically increased when the gold split-ring structure changed to three dimensional helical structure.[27]

Due to their strong light matter interaction and asymmetric structure, exceptional optical properties such as the negative refraction can be achieved by the chiral materials. Chiral materials have different refractive indices between LCP and RCP which and describe as a relation $n_{\pm} = \sqrt{\varepsilon \cdot \mu} \pm \kappa$,[20] where κ is chirality parameter, and + refers to RCP and – refers to LCP. Using the difference in refractive indices, chiral metamaterial demonstrating negative index material in GHz and THz regime was reported as shown in Figure 1.8.[30,31]

In addition, recent studies have reported that the chiral signal of the molecule is amplified, called called the "superchiral field" as shown in Figure 1.9.[32] Chiral plasmonic nanostructure can distorts electromagnetic nearfield, making the electric field and the magnetic field cross-coupled locally to form a twisted field at the microscipoc level (Figure 1.10).[36,37]

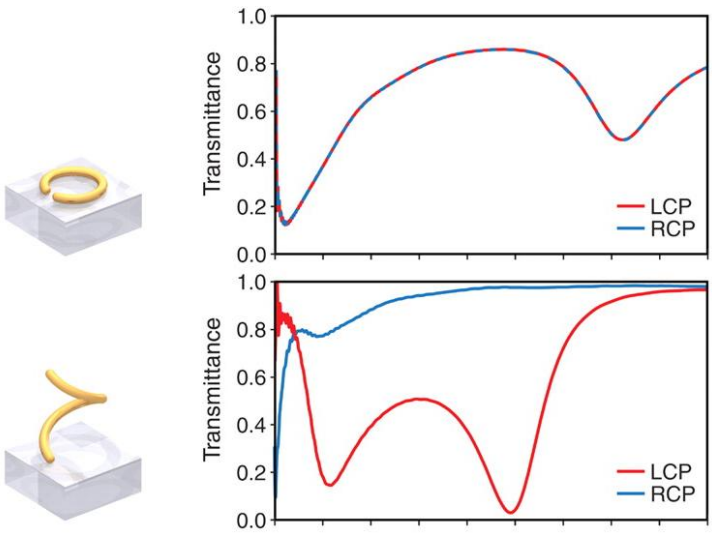

Figure 1.7 Transmittance spectra of LCP and RCP incident light for gold split-ring (top) and 3D helix (bottom).

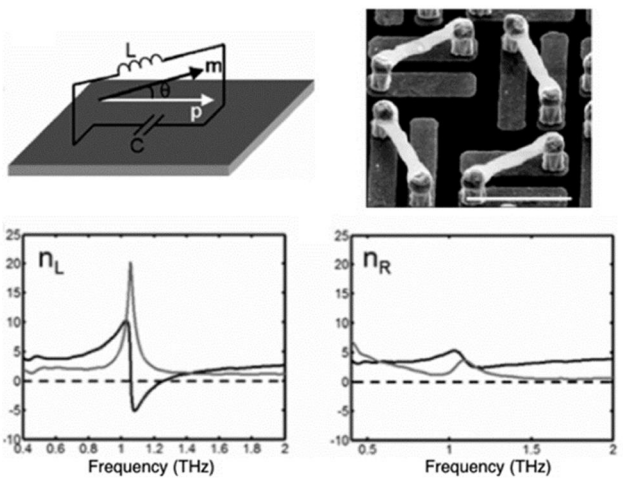

Figure 1.8 The inductor-capacitor circuit mode and the SEM image of the chiral metamaterials. Negative refractive index was achieved by LCP excitation in THz region.

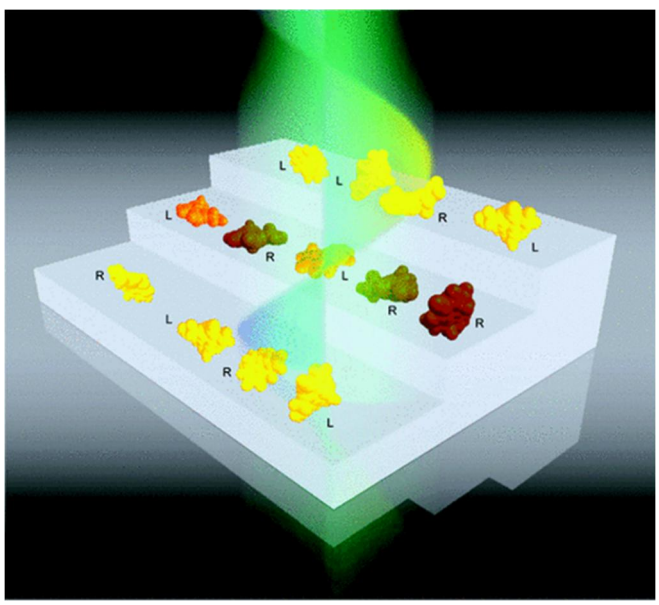

Figure 1.9 Proposed experiment that molecules at the nodal planes of the standing wave are expected to exhibit enhanced chiral asymmetry.

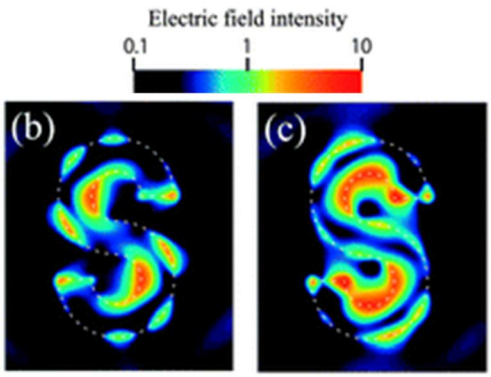

Figure 1.10 Steady state distributions of the electric field intensity for the S-shaped structure estimated using the FDTD simulation under illumination with LCP (left) and RCP light (right).

Furthermore, the chiral metamaterials can extend their applicability to chiral sensing and light control. For example, Kadodwala and coworkers reported the gold gammadion nanostructures that can be used to detect the secondary structure of protein. Using this chiral spectroscopy methodology, the molecular fingerprint which is closely related to the 3D structure of biomolecules can be analyzed (Figure 1.11).[33] Another important direction chiral metastructure can be applied is light control. Geometric phase metasurface can exhibit polarization-selective wavefront control and beam steering through elaborate design of chiral nanoarray.[34,35] In nanostructure arranged in an array, the angle of rotation within a single wavelength scale can be spatially controlled to create a space-variant phase retardation for circularly polarized light. This tilts the wavefront and changes the direction of propagation. The presented array structure can be applied to polarization-selective holographic devices, multiplexed optical communication, because the direction of light diffraction can be determined according to the direction of circular polarization.[36]

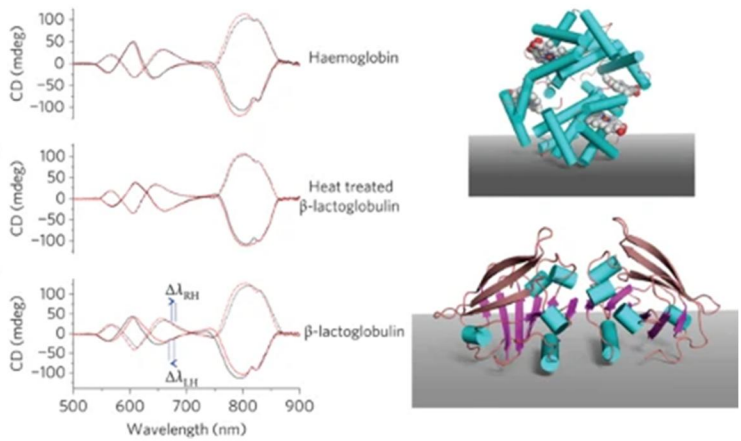

Figure 1.11 Influence of the adsorbed proteins on the CD spectra of the chiral metasurface (left). Peak shifts $\Delta\lambda_{RH}$ and $\Delta\lambda_{LH}$ caused by the adsorption of protein and exhibit different value, indicating that optical dissymmetry occurs in opposite nanostructure. Haemoglobin (top) and β-lactoglobulin (bottom) shown adopting a well-defined arbitrary structure with respect to a surface (right).

In order to efficiently apply the unique properties of chiral plasmoni metamaterials described above to optics, sensing, or catalysts, it is necessary to develop a methodology for fabricating chiral nanostructures with optical properties suitable for the intended use. The potential field of chiral nanostructure application is highly dependent on the developed chiral morphology in nanoscale. Therefore, it is important to understand the methodology for fabricating and controling these chiral nanostructures. In the following section in the introduction chapter, we would light to elaborate some methods fabricating chiral nanomaterials.

1.3 Objective of Thesis

The overall goal of this thesis is to modulate the chiroptic response using plasmon coupling through understanding and regulation of the development of chiral nanostructures. Based on understanding underlying mechanism and influential factors for chiroptic properties of nanomaterials, this work focuses on diversification of nanoparticle morphology using peptide molecules and further modulation of the optical response utilizing plasmonic coupling of nanostructures. The thesis is divided into two parts, Chapters 4 and 5 is for modulation of circular dichroism (CD) based on understanding of peptide ligands in single nanoparticles, and Chapter 6 is for manipulation of the optical properties through plasmon coupling in nanostructure.

In Chapter 2, prior to the main research, previous research trends on fabrication of chiral inorganic nanostructures was introduced. Numerous attempts to fabricate chiral nanostructure using state-of-the-art lithography techniques and molecular-assembly scaffolds have developed inorganic metal nanomaterials exhibiting fascinating physical phenomena which was difficult to be achieved in symmetric nanomaterials. Among them, we have focused on the studies that attempted to realize the chiral structure through the interaction between inorganic interfaces and biomolecules. Biomolecules with intrinsic chirality can be self-assembled in chiral geometries, and achiral plasmonic building blocks can be assembled into chiral assemblies to fabricate chiral nanostructures such as spirals, twisted rods, and asymmetric pyramids. The latter part of this chapter introduces the fabrication of chiral nanostructures through chirality transfer at the interface of biomolecules and high Miller-index plane of inorganic crystal. We believe that understanding and modulation of this interactions at the interface provides an opportunity to tailor the CD response, which is a theoretical background of chiral response modulation using peptides in the following Chapter 4.

In Chapter 3, detailed experimental procedures to develop chiral nanostructures have been discussed. Also, methods to analyze optical properties of the fabricated nanostructures have been discussed in this section

Chapter 4 discuses a broad understanding of the growth and chirality evolution in gold NPs by adjusting the type of additive molecules. Chiral morphology and resulting optical response can be manipulated by changing ligands molecules involved in synthesis. We have analyzed the growth pathway and chirality evolution of the γ-glutamylcysteine- (γ-Glu-Cys-) and cysteinylglycine- (Cys-Gly-) directed gold NPs from a crystallographic perspective. Gold NPs developed into a cube-like structure with protruding chiral wings in the presence of γ-Glu-Cys, whereas the NPs synthesized with Cys-Gly exhibited a rhombic dodecahedron-like outline with elliptical cavity structures, showing different chiroptic responses. Through time-dependent analysis, we reported that γ-Glu-Cys and Cys-Gly generate different intermediate morphologies. γ-Glu-Cys induced concave hexoctahedra-shaped intermediate, whereas Cys-Gly showed concave rhombic dodecahedra-shaped intermediate. This difference in morphology induced a change in their optical signals, showing that the chiral structure and resulting chiroptic response can be modulated through understanding the interaction between peptides and gold surfaces.

In Chapter 3 present that the role of peptides in evolving chirality to materials can vary and be diversified depending on the material. Utilizing Tyr-Tyr-Cys tripeptide ligand, we synthesized chiral cobalt oxide nanoparticles showed a g-factor of 0.01 in the UV–visible region. In addition, the 3D conformation of the peptide ligand on the nanoparticle surfaces was identified by 2D NMR spectroscopy analysis. Furthermore, the sequence effect of Tyr-Tyr-Cys developing chiral cobalt oxide was analyzed, demonstrating that the thiol group and carboxyl group of the Tyr-Tyr-Cys ligand played an important role in chirality evolution. This results

suggest that the role of the peptides can vary depending on the interacting material, leading to further variability in chiroptical properties.

In Chapter 5, the optical signal of plasmonic nanostructure was amplified and sensitively controlled using plasmon coupling. We demonstrated the fabrication of metamaterial by coating chiral gold nanoparticles on a substrate and depositing a nanoscale plasmonic metal layer. In order to investigate changes in optical properties due to plasmon coupling, transmission-based and diffuse reflectance CD spectroscopy were utilized. Through this, it was confirmed that the resonance position, magnitude, and sign of the CD spectrum were changed by plasmon coupling. In addition, the coupled plasmon mode was significantly changed according to the dimension, distance, and refractive index of the nanostructure. Furthermore, synthesis of chiral gold-silica core-shell NPs enables versatile control of the structure and properties of plasmonic nanoparticles, facilitating their application to tailored plasmon coupling.

We believe that manipulating the chiroptical properties of chiral nanostructures by understanding the role of peptides and plasmonic coupling in nanoscale will ultimately facilitate the integration of chiral metamaterials into practical optical devices.

Chapter 2.Fabrication of Chiral Inorganic Nanostructure and Its Optical Properties

2.1 Fabrication of Chiral Nanostructures using Hard Approach

Thanks to tremendous efforts, chiral nanostructures with exceptional optical properties have presented using hard approach and molecular-scaffold based fabrication approach. Thanks to the recent improvement of nano-fabrication techniques, the fabrication utilizing hard approach such as direct laser writing and lithography manifests sophisticated and organized chiral nanostructures. Systematic and sequential nano-patterning has allowed the construction of chiral morphologies with various size and dimension scales.[29,37–42] For example, utilizing electron beam lithography, a layer by chiral structure was demonstrated.[40]

Similarly, layer-by-layer stacking using electron-beam lithography can generate a three-dimensional chiral nanostructure. Recently, chiral oligomer structures was demonstrated by assembling components of chiral structure as shown in figure 2.2.[38] The three-dimensional chiral structure was fabricated by assembling 3 nano-dics to form an L-shape in the first layer, followed by placing foruth nano-disc in the second later. The location of fourth could determine the handedness of the overall structure, inducing chiroptic responses. Sequential stacking of lithographed structure exhibited chiral structure of multi-layers twisted each other which as shown in SEM image (Figure 2.1).

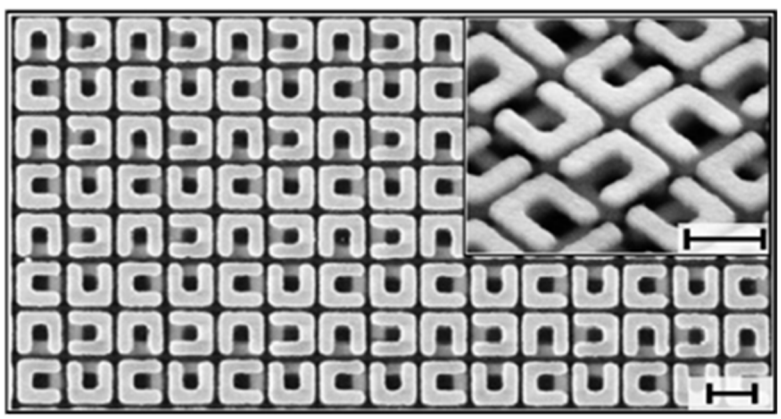

Figure 2.1 Low magnification and high magnification (inset) SEM images of chiral unit cell composed of gold split-ring-resonators. Scale bars are 400 nm.

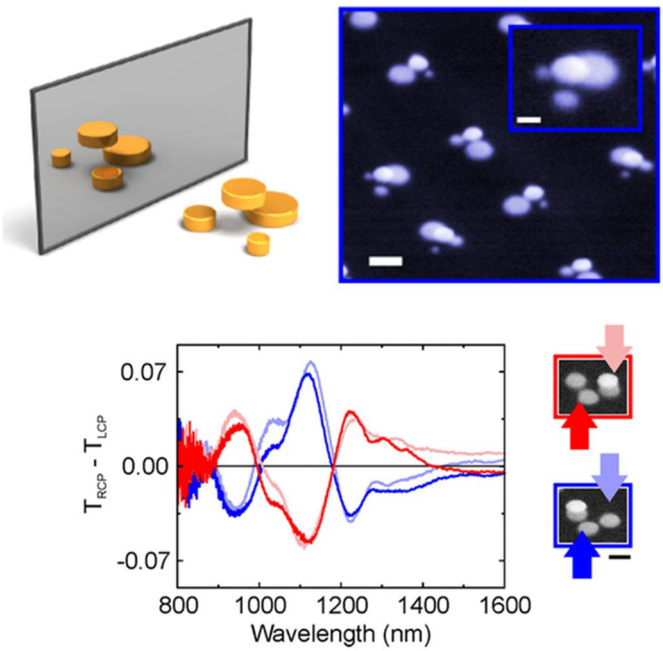

Figure 2.2 SEM images of E-beam lithographed three-dimensional chiral oligomers (top). The scale bar is 100 nm for the inset image and 200 nm for the overview. ΔT spectra of chiral structures for forward and backward illumination (bottom).

Although stacked structure can be fabricated by repeated lithography technique, hard approach show limitations on fabricating genuine 3D chiral structures. To overcome the limitations of flexible design and fabrication through z-axis, a method for fabricating a chiral nanostructure extended in the z-axis direction was demonstrated by direct laser writing as shown in Figure 2.3.[37] Through successive two-photon direct laser writing and electroplating, Gansel and co-workers demonstrated three dimensional helical structure. The constructed chiral helical structures showed helical nanostructure possessing uniformly rotated helical turns around the vertical axis. In addition to direct laser writing, fabrication methods such as colloidal nanohole lithography, glancing angle deposition, and on-edge lithography can be used to fabricate chiral nanostructures.[43–45] These top-down fabrication methods holds many probabilities for creating complex 3D nanostructures at the nanoscale.

Through the above representative examples, we could see that the fabrication of three dimensional chiral structures by top-down approach is advantageous for the development of complex chiral structures, but there are also inherent limitations. Despite advances in lithography technology, the relatively low spatial resolution is a major hindrance for generating sub-wavelength chiral nanomaterials for practical applications. Unlike aqueous-based syntheses, which can utilize isotropic media, top-down fabricated structures are always fixed at interfaces which contains various types of media. In addition, since the manufacturing process is too complicated and requires a lot of cost and process time, it has limitations in application from an industrial point of view.

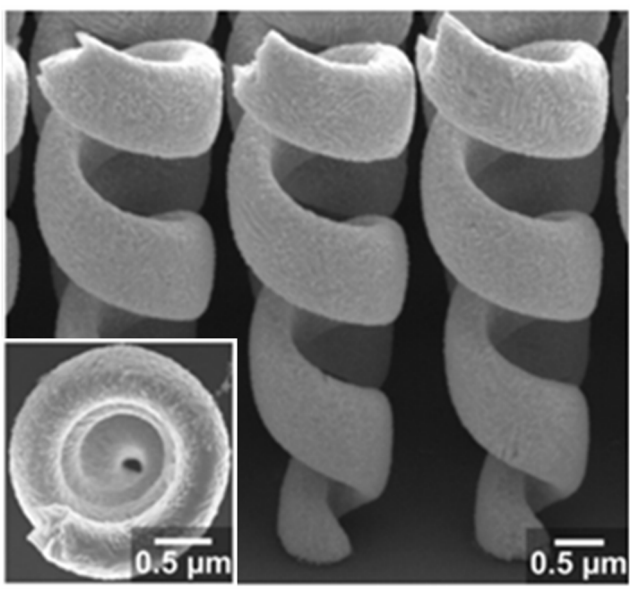

Figure 2.3 Top (inset) and side view SEM images of gold-helix metamaterials fabricated by direct-laser writing.

2.2 Biomolecule-Directed Chiral Nanostructure

Chirality can evolve through synthetic method using molecular scaffold and even single biomolecules such as amino acid, and DNA. In nature, amino is the smallest building blocks possessing intrinsic chirality. This building blocks are often utilized to transfer chirality from molecular scale to macroscopic morphology. Chiroptic response can be induced from distortion in atomic conformation due to enantio-specific interaction between chiral biomolecules and inorganic surface. In this section, we highlight recent studies of understanding interface behavior in between chiral molecules and inorganic surfaces. Importantly, ability of amino acids and peptides can evolve chirality from microscopic atomic conformation to macroscopic chiral morphology.

2.2.1 Biomolecule-Conjugated Inorganic Nanoparticles

The origins of chiral properties of inorganic and metal materials are not limited to crystal or surface chirality. Even achiral crystals can exhibit chiral properties by interaction with surrounding chiral organic molecules at optically active range of metals. From electronic coupling between organic molecules and local electric field of metal or inorganic crystals, this kind of induced chirality often emerge.[46,47] Optical inorganic nanocrystals with excitonic optoelectronic properties or metal nanoparticles with localized surface plasmon are often selected as materials for coupling with chiral molecules. The most significant results are chiroptical properties. These properties can be represented by circular dichroism (CD) which refer enantio-selective absorption for circular polarized light, and optical rotatory dispersion (ORD), which refer optical rotation of linear polarized light.

Chiroptical properties at visible range have fascinated researchers from various fields due to their potential application in novel technologies. For example, amplification and detection of molecular circular dichroism signal can be realized by induced chirality on plasmonic metal nanomaterials at visible range. It is critical to detect molecular chirality in industrial sectors where bimolecular enantiomers exhibit totally different effects, such as pharmaceutical, medical, catalytic and chemical industries. In addition, chiral absorption and emission of optical nanomaterials have been analyzed as possible application for metamaterials. Such metamaterials exhibit extraordinary properties which is not observed in common bulk materials.[20,48–50] In this regard, underlying mechanisms and practical applications on induced chirality of achiral crystals have been largely researched.

Localized Surface Plasmon Resonance (LSPR) is oscillation of electron near the plasmonic nanoparitlcle surface, when there is light illumination. These resonating field is concentrated at the surface of plasmonic nanoparticles and decayed exponentially with increasing distance from its surface. Therefore, researchers have focused on the surface of plasmonic nanoparticles in order to transfer local electric field energy from plasmonic nanoparticles to organic molecules. Representatively, through conjugation of molecules to nanoparticle surfaces, this strategy can be realized. Gautier et al. showed opposite chiroptical signals can be generated by simple gold nanoclusters upon the attachment of ligand onto their surface. When conjugated ligand was exchanged from L form to D form (R form to S form), inversion of CD signal was observed (Figure 2.4). Similarly, Govorov et al. theoretically supplemented the experimental result showing using of

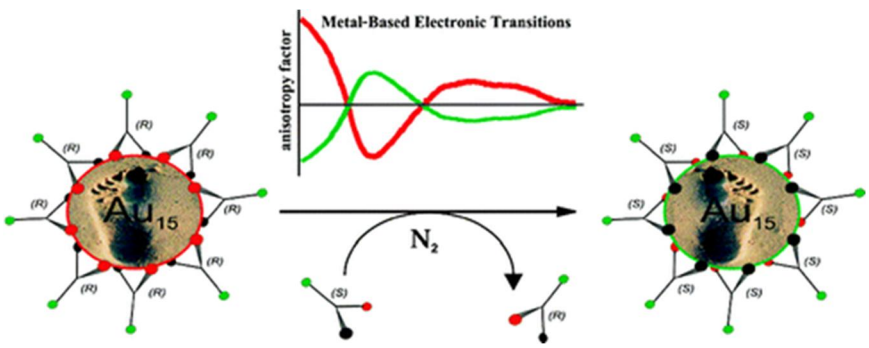

Figure 2.4 CD response of chiral thiol-molecule conjugated gold nanoclusters

plasmon resonance for amplifying chiroptical signals by interacting with chiral molecules. Two viable explanations were suggested. One is that plasmon resonance influencing E-field distribution of chiral molecules. The other is that the molecular dipole inducing changes in optical responses of metal-molecule complex. Based on proposed explanations, researches have been further conducted to use plasmonic nanomaterials for measurement and amplification of chirality of molecules. Furthermore, they have focused on providing potential design principle for various plasmonic inorganic-organic hybrid materials.

Through utilization of morphologically various nanoparticles, illumination of different relations between inorganic nanoparticles and organic molecules has been the other stream of researches. Gregorio et al. showed CD signals at their plasmon resonance range was induced by silver nanocube with glutathione ligand. Through oxidation reaction of thiol group attached onto silver nanocube surface, origin of CD signal was confirmed. In detail, detachment of ligand eliminated the existing chiroptical response. Levi-belenkova et al. also utilized silver nanocube, and showed induced chiroptical signal using polyproline-2 based helical peptides as chirality inducer. Induce of chiroptical signal in silver nanocube-peptide hybrid structure was proposed to be resulted from multi-pol mode interaction between organic molecule and inorganic silver nanocube surface (Figure 2.5). This claim was difficult to be understood with conventional understanding, that simple dipole mode interaction between plasmonic nanoparticles and molecules. Silver nanocube structure has much more complicated structures with different electric field distribution, whereas conventional understanding only considers the simple spherical structure. Although studies about interaction between plasmonic nanostructures and chiral molecules have been highlighted, it is difficult to completely understand and utilize this concept.

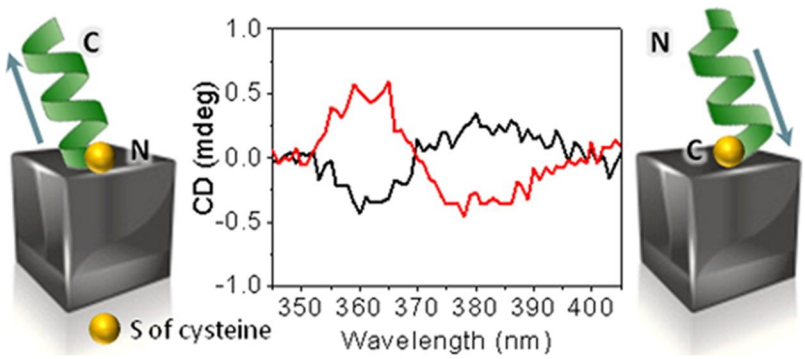

Figure 2.5 Silver nanocubes conjugated with peptide and their CD signals for opposite handedness of peptide molecules.

In order to achieve various chiroptical properties, induced chirality of the inorganic crystal has been analyzed on quantum dots, rods or wells. Extensive works have been done on II-VI semiconductor nanomaterials, such as CdS and CdSe.[51–60] Various reports showed that CD was observed when chiral molecules, typically cysteine,[51,53–55,59] are attached on achiral crystals. As demonstrated by experimental and calculation results, the CD can be understood as the result of electronic coupling between dielectric nanocrystals and chiral molecule rather than structural chirality. Govorov et al. theoretically predicted that the circular dichroism resulted from coupling between chiral molecules and achiral dielectric nanoparticles.[61] Experimental results demonstrated that circular dichroism can be induced throug controlling chirality of attached ligands on achiral quantum dots. Xiaoqing Gao et al. also presented that induced chirality on CdSe nanoplatelets utilizing L- and D-cysteine ligands.[52] Opposite circular dichroism was observed for L- and D-cysteine. In addition, distinguishable spectrum depending on crystal structure was observed. In detail, wurtzite showed three upward circular dichroism peaks when L-cysteine was used as ligand in visible range. On the other hand, zinc-blende showed one downward and two upward (Figure 2.6). Experimental results which describes coupling of the electric dipole transition moments of CdSe nanoplatelets and cysteine were further understood by DFT calculation on non-degenerate coupled-oscillator model. The difference in CD depending on crystal structure exhibits that orbital of CdSe is coupled with cysteine, and shows excitonic circular dichroism.

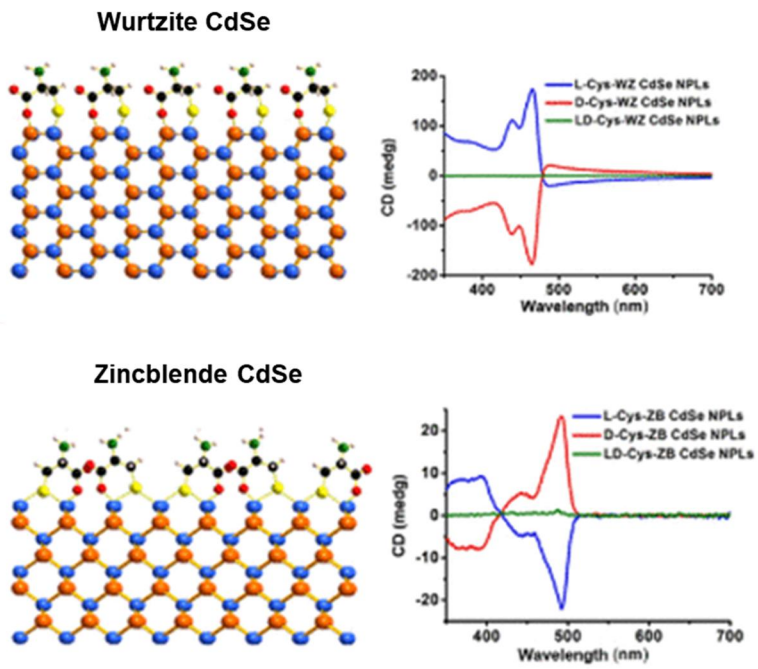

Figure 2.6 Interface of wurtzite CdSe nanoplatelets conjugated with cysteine and their CD signal for different enantiomers (top). Interface of zincblende CdSe nanoplatelets conjugated with cysteine and their CD signal for different enantiomers (bottom).

2.2.2 Chirality Development by Biomolecule-Induced Local Distortion

Another interesting strategy inducing chiroptical signal in inorganic materials is to utilize distortion of local atomic conformation on inorganic material's surface by organic-inorganic interaction. Chirality from atomic distortion is different from organic molecule induced chiroptical signal, because their origin of chirality is directly from material itself. In this section, representative theoretical and experimental backgrounds and examples of chirality evolution by local distortion will be summerized, respect to material types.

Plasmonic materials have often been selected as ideal material to observe chiroptical response. T.Gregory schaff et al. reponsted chiroptical response generated through deposition of monolayer of glutathione molecules onto gold cluster at 1998. Similarly, Jadzinsky et al. synthesized and analyzed atomic structure of p-mercaptobenzoic acid (p-MBA) conjucated gold nanoparticles through powder X-Ray Diffraction analysis. p-MBA treated gold nanoparticles showed chiral arrangement of atomic configuration within a unit cell scale (Figure 2.7). The study of chiral adsorption patterns, such as the formation of localized distortions on surfaces, has allowed many researchers to interpret previous studies of chiral evolution from inorganic materials treated with chiral molecules.

In addition to chirality transfer from organic molecules to plasmonic materials through local distortion, methods and strategies to apply the concepts to semiconducting materials were enthusiastically researched due to the excellent optical and electrical properties of semiconducting materials. By attaching L & D penicillamine molecules onto surface of CdS nanoparticles, Micheal et al.

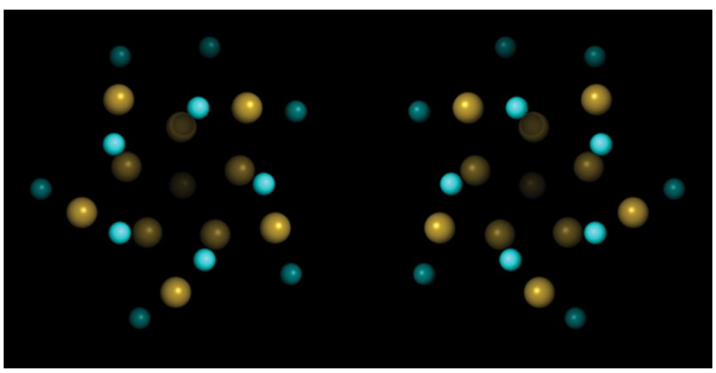

Figure 2.7 Top view of p-MBA capped chiral gold nanoparticles along their cluster axis for two different enantiomers.

synthesized Cadmium Sulfide (CdS) nanoparticles. Adsorbed penicillamine induce different chirality to CdS nanoparticles, and the optical activity was measured by CD measurement. The CD spectrum showed totally inversed signal for L & D penicillamine treated CdS nanoparticles. Also, 0 circular dichroism signal was observed for CdS nanoparticles treated with racemic penicillamine molecules. In addition, these induced chirality of inorganic nanomaterials by local distortion was shown to be sustained by attachment of any types of ligand. It was maintained in the presence of achiral ligand, demonstrating that it could stabilize the distorted surface. This chiral memory effect can overcome the previous existing stability issue of bottom-up synthesized nanomaterials.

Similarly, Nakashima group fabricated thiolated ligand adsorbed CdTe nanoparticles in order to give local distortion on CdTe nanoparticle surfaces (Figure 2.8). After observing the optical activity of CdTe nanoparticles, ligand exchange from chiral molecules to achiral one maintained the chiroptical activity of pre-synthesized CdTe nanoparticles. Yunlong Zhou et al. analyzed chirality transfer through local distortion of surface by inspection of atomic configuration and structure of inorganic material surface. CdTe nanomaterials covered with L & D cysteine molecules showed chiroptical response through atomic distortion. Calculated results corresponded to opposite atomic conformation for this L & D enantiomers. This finding allows understanding in local chiral distortion obtained from chiral organic molecules, and gives strong evidences to previous researches and hypothesis on chirality generation by atomic distortion in inorganic nanomaterials.

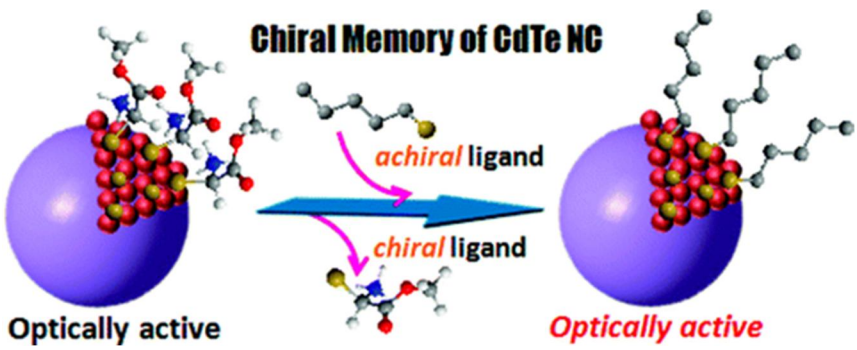

Figure 2.8 Schematic of chiral memory effect in chiral CdTe nanoclusters.

Furthermore, this reserach provided a ground point for further works on relationship between nanostructures or atomic configuration and the degree of optical responses. As an extension of this theory and analysis, Shuang Jiang et al. used two different chiral molecules to enhance and control the optical activity of nanomaterials. In their study, they synthesized a chiral ceramic material (tungsten oxide hydrate nanoparticles) with two different amino acids, proline and aspartic acid. When this material adheres to the surface of ceramic nanoparticles, it is expected that several degrees of localized deformation will occur. As a result, the degree of local distortion and optical activity differed according to the intrinsic chirality of molecules adsorbed on the surface of inorganic nanomaterials.

Chirality through atomic configuration was evolved with higher dimension of controllability, in the case of magnetic materials. Conventionally, material properties especially chirality was a permanent feature of nanomaterials after fabrication or synthesis unless applied with irreversible chemical treatment. However, controllability of handedness on atomic scale was allowed when external magnetic field induce local distortion on inorganic materials. Representatively, Yeom et al. characterized L & D cysteine induced chiral paramagnetic cobalt oxide nanoparticles under external magnetic field. These cobalt oxide nanoparticles originally showed strong chiroptical responses (Figure 2.9). When there is external and non-invasive magnetic field, local atomic configuration was controlled to modulate the chiroptical signal (Figure 2.10). Although there are methodologies to change chirality of already fabricated nanoparticles through irreversible chemical treatment, real-time tuning of chirality through external magnetic field showed versatile potential of chiral nanomaterials application in industry.

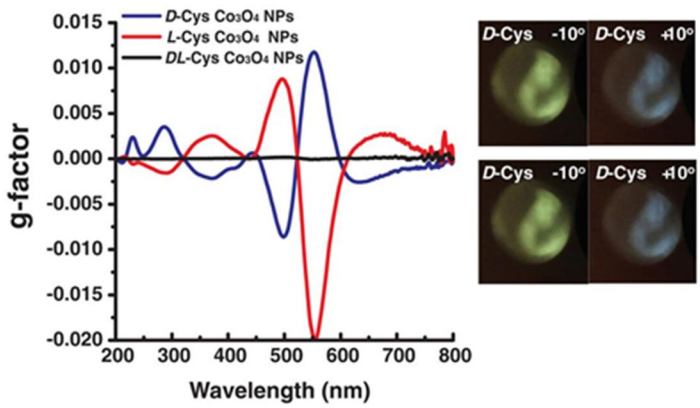

Figure 2.9 *g*-factor spectra of L, D and racemic cysteine treated Co_3O_4 NPs (left), and visualization of ability to rotate polarization of light for Co_3O_4 NPs (right).

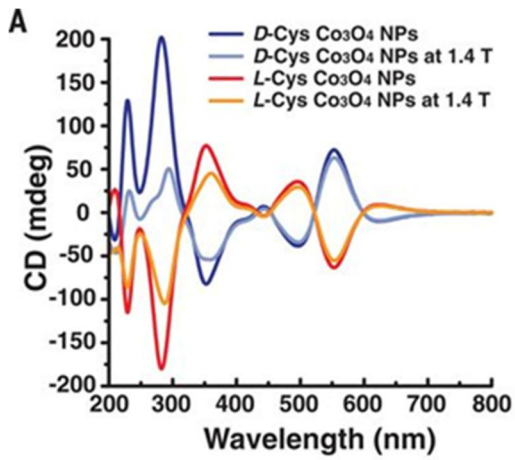

Figure 2.10 Changes in circular dichroism spectra of L-Cys and D-Cys Co3O4 NPs under magnetic field.

In this section, representative studies and recent advances in chirality transfer from organic molecules by local distortion of inorganic materials was discussed. In the following section, evolution of macroscopic morphology change in nanomaterials induced by chiral molecules and the relation between macro-structures and their chiroptical responses will be summarized.

2.2.3 Biomolecule-Directed Chiral Morphology

The exceptional properties of biological molecules to induce reconstruction of inorganic surfaces enable macroscopic changes in the nanomaterial morphology. Through encoding of biological molecules, sophisticated 3D chiral morphology of inorganic nanostructures can be obtained, thus maximizing the chiroptic activity between RCP and LCP.[50,62] In this section, we discuss the evolution of chiral morphology and chiroptical response in single nanostructure level, and macroscopically hierarchical chiral structures made of single chiral units in semiconducting materials. Furthermore, we highlight single plasmonic chiral nano-morphology with exceptional optical activity.

From enantioselective adsorption of chiral molecules on its crystal surfaces, macroscopic chirality of inorganic materials could evolve.[63,64] Especially materials which possess crystallographic chirality exhibits advantage in efficiently tailoring chiral shape and optical properties. Adsorption of amino acid on [21$\bar{3}$1] trigonal scalenohedon calcite structure has been reported.[65,66] Calcite crystal possess intrinsic chiral selectivity on its crystal surface due to their pairs of mirror symmetric adjacent facets. Teng and co-workers showed that the addition of aspartic acid dramatically affect the growth of calcite, exhibiting adsorbed layer aligned on the crystal facets change the surface energy.[67] In the early 2000s, Hazen and co-workers experimentally demonstrated the selective adsorption of D- and L-amino acids on calcite.[65] When immersed in the racemic aspartic acid solution, adjacent scalenohedral faces of calcite crystals equivalent to (21$\bar{3}$1) and (31$\bar{2}$1) plane showed a selective adsorption of D- and L-aspartic acid molecule up to 10%, while the achiral surface exhibited no adsorption difference. This selective adsorption takes place on the kinks along the steps preferentially, showing preferential adsorption of

one enantiomer on chiral terraced surfaces.

Enantio-specific binding of the amino acids can lead to macroscopic crystal shape modifications through changing the free energies of step-edges. This binding could lead to chiral deformation in macroscopic lengths scales.[68] Chiral morphology development by encoding of chiral biomolecules has been presented in several semiconducting materials such as potassium dichromate,[69] seleniumcinnabar (α-HgS),[15] and tellurium.[70] These materials have unique chiroptical properties owing to their morphological chirality from the enantio-specific binding of biomolecules. CD response of semiconducting materials is originated from the chiral morphology, whereas the CD activity in metal nanostructures is originated from the structural and plasmonic property.[70,71] Materials with chiral spatial orientations could exhibit scattering-based chiroptical properties owing to their chiral interface, leading to selective reflection and transmission of one-handedness of circularly polarized light.

Recently, Wang and coworkers presented chiral construction of cinnabar mercury sulfide nanocrystals. The twisted shape originated from surface deformation by D-, L- penicillamine molecules (Figure 2.11). Cinnabar α-HgS lattice with a space group of $P3_221$ has atomic scale primary chiral unit. In this report, the handedness of morphology induces by epitaxial synthesis depend mainly on the type of chiral molecules involved during the growth rather than the crystallographic chirality of the initial seed nanoparticles. For example, initial seed crystallographic chirality could be directly portrayed on the final morphology upon the addition of precursor atoms without chiral molecules in the epitaxial synthesis. However, the handedness of chiral molecules determines the chirality of atomic conformation of the surface with chiral biomolecules. Consequently, morphology transfer occurs from handed biomolecule to the overall nanostructures at larger length scale. Ben-Moshe and coworkers reported

chiral selenium and tellurium nanocrystals synthesized by enantio-selectively oriented adsorption of chiral biomolecules. As shown in Figure 2.12, chiral tellurium nanoparticles synthesized in the presence of glutathione have twisted ridges and triangular protrusions at the ends. In addition, different shapes of tellurium nanoparticles were obtained using different biomolecules such as cysteine and penicillamine. Chiral nanocrystals are generated by initial formation of chiral atomic clusters and attachment of generated clusters in an oriented ordering. The thiolate ligand molecule determines the morhpology and stability of the Te complex thereby affecting the growth kinetics.

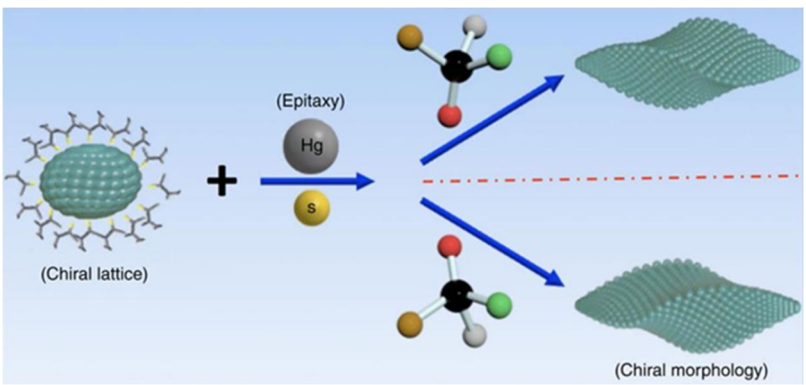

Figure 2.11 Schematic of two-step growth process involving D- and L-penicillamine, to develop chiral morphology of α-HgS nanostructure.

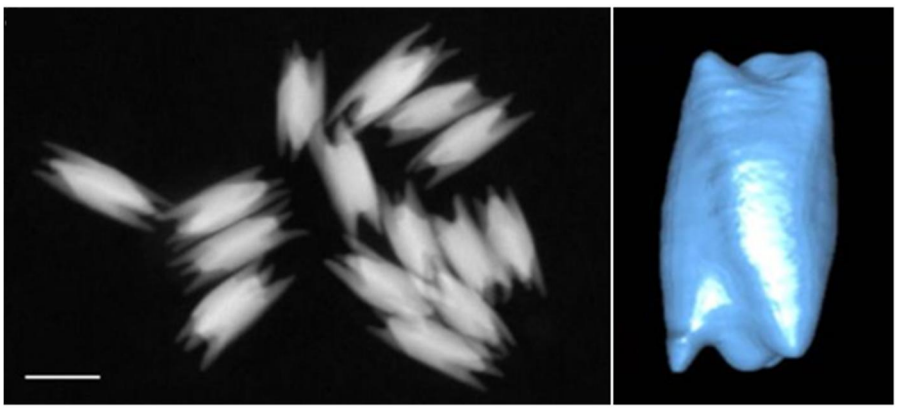

Figure 2.12 Dark-field STEM image (left) and tomographic reconstruction image (right) of chiral tellurium nanoparticle. Scale bar is 100 nm.

Through self-assembly of chiral molecule and inorganic materials, extending chiral structure generation from atomic scale to microscale is possible. Bio-mineralization of nanoscale calcium carbonate building blocks with enantiomeric amino acids could generate large scale chiral vaterite with counterclockwise or clockwise toroids.[72,73] Jiang and co-workers demonstrated that tilting of subunit induced by attached chiral additives induce cascade tilting of adjacent subunits, resulting in macroscopic chiral structure.[72] In addition, self-assembly of CuO[74] and ZnO[75] film with hierarchical chiral structure has been presented. Duan and coworkers demonstrated flower shaped CuO nanostrtucture which possess hierarchical chirality utilizing an amino alcohol as a symmetry-breaking agent. Nanopetals in the flower shaped CuO nanostructure are made of several subnanopetals which are stacked in a left- and right- handed helical structure. Also, the flower-like CuO nanoparticles formed with amino alcohol with opposite chirality showed the same structure in the opposite direction (Figure 2.13).[74] A year after, Wang and coworkers presented hierarchical chiral superstructure of self-assembled ZnO film. The film exhibited large optical activity due to light scattering and absorption in the chiral hierarchical structures (Figure 2.14). Asymmetric attachment of L- and D-methionine with Zn^{2+} ions that acts as a symmetry breaking agent induces chiral hierarchical ZnO nanostructure on quartz substrate. ZnO films generated helical nanoplates as a primary chiral structure while helical stacking of aggregates formed secondary and tertiary chiral structure. ZnO nanoplates stacked in opposite direction of the handedness of the primary unit attributed to the bending of the nanoplates, in the presence of symmetry breaking molecules. Microscaled secondary and tertiary structure generated scattering-based CD signals, whereas absorption based CD was induced by the primary chirality of helical structures in ZnO films.

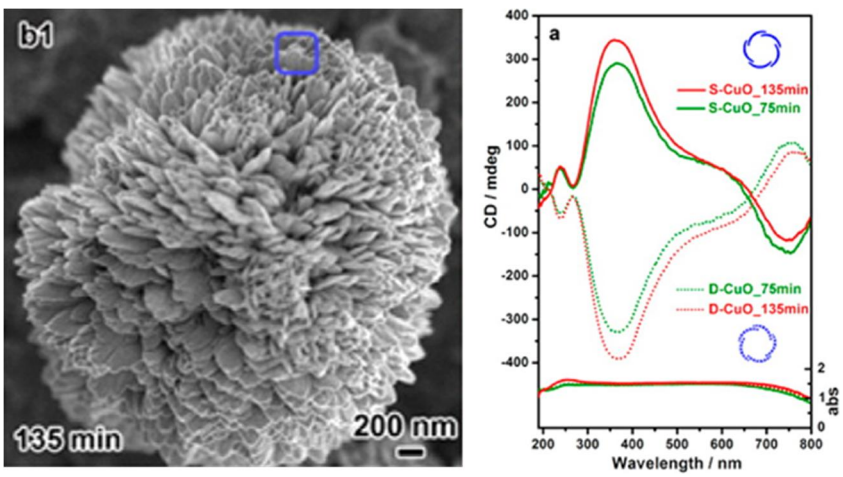

Figure 2.13 SEM image of peony-like CuO nanoflowers synthesized with (*S*)-(−)-2-amino-3-phenyl-1-propanol (left). UV–vis absorption and CD spectra of the chiral CuO nanoflowers (right).

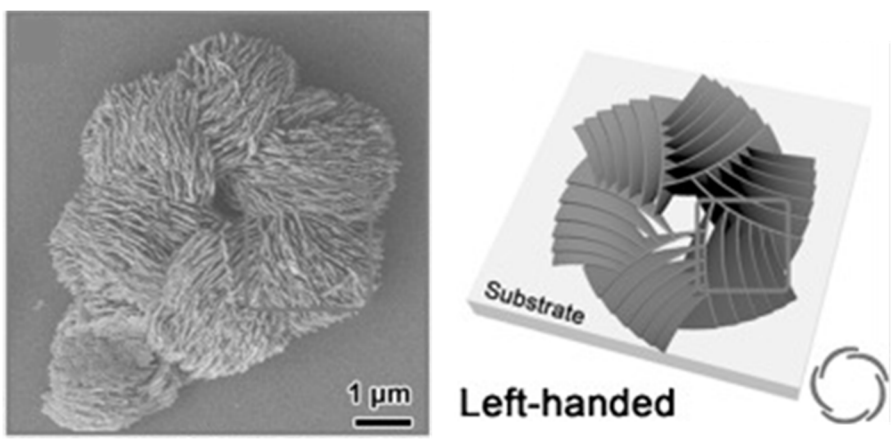

Figure 2.14 SEM image (left) and schematic drawing (right) of the hierarchical chirality in L-chiral ZnO films.

Chirality transfer from molecular structure to macroscopic crystals can be expanded to plasmonic materials in nanoscale.[47,76–79] Preferential attachment of the biomolecules enabled morphology manipulation of metal surfaces in a single particle level, whereas earlier studies have focused on the chiral structure of self-assembled plasmonic nanoparticles and its optical responses.[80–84] Due to the plasmonic properties, single plasmonic nanoparticles which possess chiral morphology could generate strong chiroptical response at its plasmon frequency. Based on Drude model, Fan and co-workers demonstrated computational modal analysis of plasmon resonances of a chiral nanocrystal. They reported that chiral twister with helical surface showed the strong CD responses at the main plasmonic resonance. Crystal surface with low Miller index undergoes reconstruction to expose chiral high Miller index planes upon adsorption of chiral molecules on the surface. The chiral distortions of plasmonic nanocrystal generated splitting and mixing of plasmonic modes inducing strong optical chirality.

Using amino-acid and peptide and high-index facets, chiral nanoparticle can be induced through aqueous based seed-mediated method. In this strategy, the generation of high-index facets is important. These high-index facets containing chiral kink sites, can determine their chirality by the orientation of their low-index components as shown in Figure 2.15.[85,86] For example, in the case of hexoctahedron-shaped gold nanoparticle, equal ratio of R and S high-index surface can be expressed throughout the nanoparticle as shown in Figure 2.16.[87]

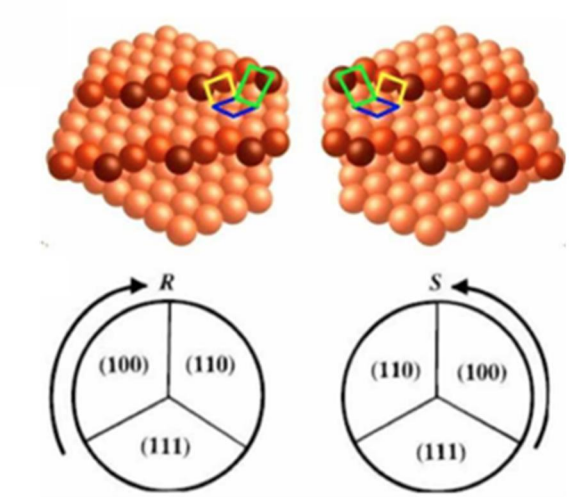

Figure 2.15 Schematic of inorganic surface chirality which chirality is determined by the rotation direction of the low-index components on the kink sites

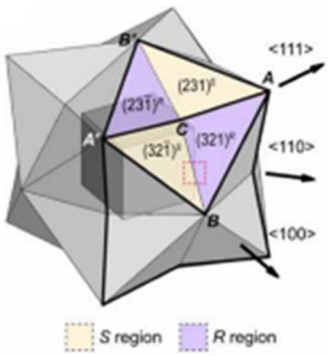

Figure 2.16 Schematic of chiral high-index surface on {321} facet-exposed hexoctahedron nanoparticle.

Recently, exceptional chiroptical response of chemically synthesized chiral gold nanoparticles in nanometer scale was experimentally demonstrated using cysteine and cysteine containing peptide as a chiral shape modifier.[87] Synthesized nanoparticle exhibited mirror symmetry in its nanomorphology respect to the chirality of chiral shape modifier. Also, its chiroptical response showed a perfect mirror symmetry with absorption peaks matched in visible range (Figure 2.17).[87] As mentioned above, surface chirality can exists even for highly symmetric fcc metal crystals faces which lack of mirror symmetry. All {hkl} ($h \neq k \neq l \neq 0$) high-Miller-index facets are non-superimposable and denoted as R(S) depending its surface atomic configuration. This intrinsic chirality of crystal planes can host enantioselective interaction between molecules to plasmonic inorganic materials. Therefore, it is important to provide chiral atomic sites for successive chirality transfer from molecular to plasmonic material. In order to precise control the exposed high-index facets, seed-mediated synthesis was implemented using organothiol additive as shape modifier.[88,89] In the absent of chiral additives, cube seed nanoparticle develops into stellated hexoctahedron with 48 identical exposed high-index planes exhibiting $4/m\bar{3}2/m$ point group symmetry. In the presence of the chiral molecule, a preferred interaction between peptide with the generated chiral facet mitigate the growth. This gradually shifts the R-S boundary during growth proceed, resulting in an asymmetric growth. This asymmetric growth lead to break of mirror and inversion symmetry generating 432-point group

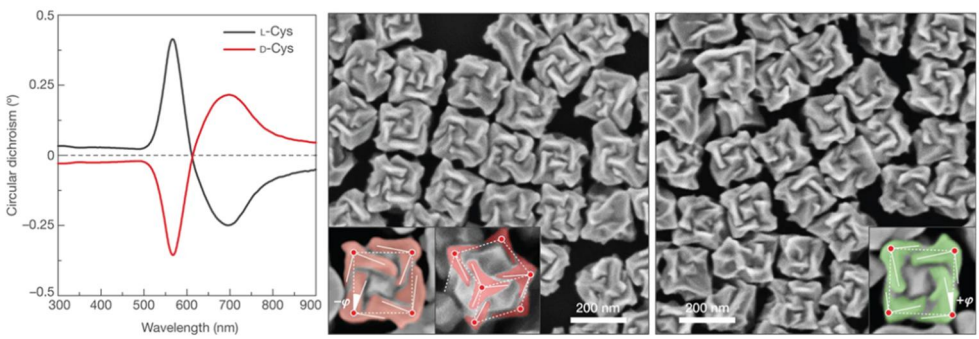

Figure 2.17 Chiral morphology of gold nanoparticle. CD spectra of chiral helicoids synthesized with L- and D-cysteine (left). SEM images of chiral gold synthesized with L- and D-cysteine (right).

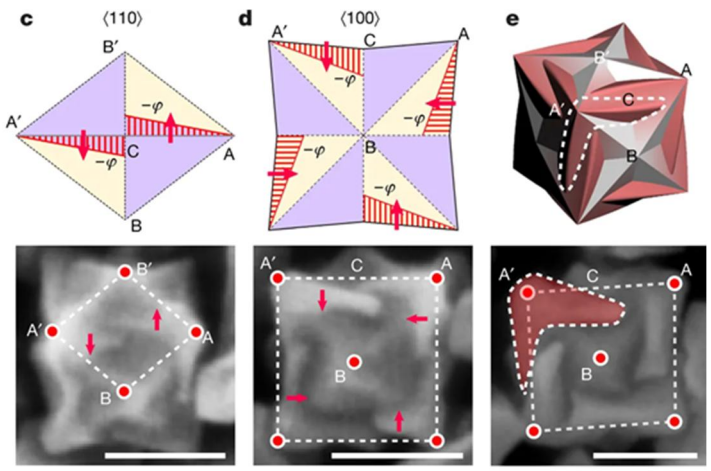

Figure 2.18 Schematic (top) and corresponding SEM images (bowwom) when L-cysteine molecule involved during synthesis. A'C and AC edges shifts in opposite direction generating chiral feature.

symmetry. When L-cysteine molecule involved during synthesis, A'C and AC edges shifts in opposite direction when viewed from (110) direction (Figure 2.18).[87] To be specificy, the outer edges of nanoparticle A'C and AC shifts to the center of the nanoparticle in clockwise rotation generating chiral morphology when viewed from (100) direction. On the other hand, usage of D-cysteine resulted in counterclockwise rotation of edges.

Importantly, different chiral morphology could be generated when chanding chiral molecule from cysteine to cysteine containing glutathione (GSH) molecule induced. As shown in Figure 2.19, growth under addition of L-GSH molecule resulted in curved AB'and A'B edges and protrusion of A'B' and AB edges in (110) direction. When viewed from (100) direction, we could clearly observe clockwise rotation of inner edges A'B and AB generating a pinwheel like structure.[87] Furthermore, we could tune the chiral morphology and resulting chiroptical response through control of seed morphology. Incorporation of GSH molecule and {111} facet enclosed gold octahedron seed generated cube-shaped chiral nanoparticle containing four high-curved gaps on each six facets with pinwheel-like structures, named 432 helicoid III. 432 helicoid III nanoparticle showed an outstanding chiroptical activity g-factor of 0.2 (Figure 2.20).[87] Possessing this high intrinsic chiroptical response, 432 helicoid III can exhibit direct visualizations of macroscopic color conversions when polarization conditions were changed as shown in Figure 2.21.[87] This bottom-up synthetic route introduced in Chapter 2, which uses chiral biomolecules to generate chiral structures, has potential for chiral nanoparticle formation and its applicability in practical devices such as chiral sensing, active color display, holography, and negative refractive index materials.

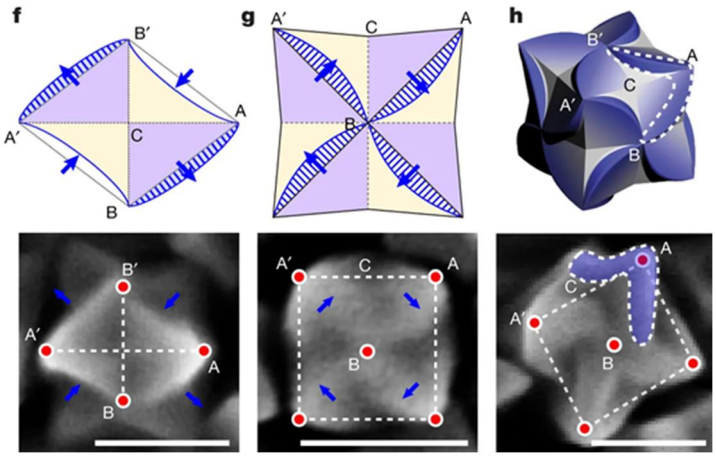

Figure 2.19 Schematic (top) and corresponding SEM images (bowwom) when L-glutathione molecule involved during synthesis.

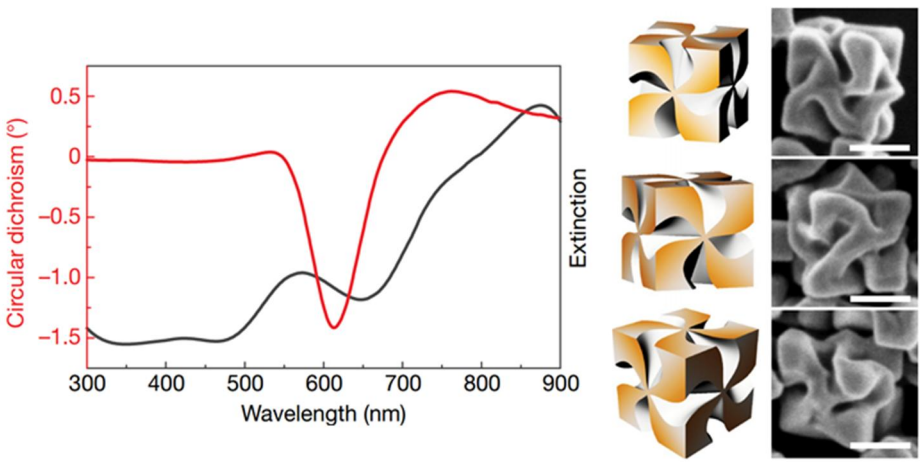

Figure 2.20 CD and extinction spectra of 432 helicoid III nanoparticle (left). Schematic and corresponding SEM images of 432 helicoid III nanoparticle (right). Scale bar is 100 nm.

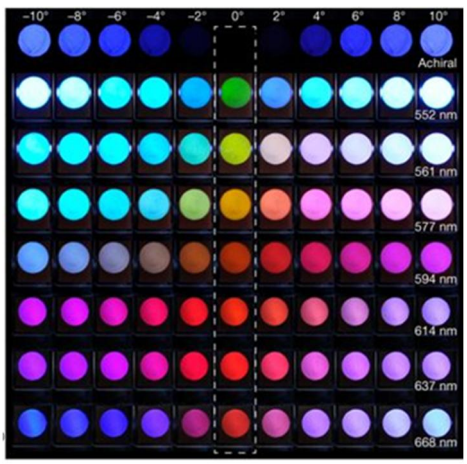

Figure 2.21 Transmitted color of 432 Helicoid III particle and achiral particle solutions with different size under cross-polarized conditions. Gradual color tuning observed by rotating the analyzer.

Chapter 3. Experimental Procedures

3.1 Synthesis of Chiral Gold Nanoparticles

Chemicals

Hexadecyltrimethylammonium bromide (99%) was purchased from Acros. Hexadecyltrimethylammonium chloride (98%), L-ascorbic acid (AA, 99%), tetrachloroauric(III) trihydrate ($HAuCl_4 \cdot 3H_2O$, 99.9%), sodium tetrahydridoborate ($NaBH_4$, 99%), and potassium iodide (KI, 99.5%) were purchased from Sigma-Aldrich. Dipeptides, γ-L-glutamyl-L-cysteine (98%, Bachem) and L-cysteinylglycine (85%, Sigma-Aldrich) were obtained commercially and used without further purification. High-purity deionized water (18.2 MΩ cm) was used in all of the procedures.

Synthesis of gold octahedron nanoparticles

Gold octahedron nanoparticles were synthesized as previosly reported.[90] Spherical gold seed (~2.5 nm) was prepared by mixing 250 μl of 10 mM gold chloride trihydrate, 450 μl of 20 mM $NaBH_4$ solution, and 10 ml of 100 mM CTAC solution. The solution was kept at 30°C for 2 hours. The growth solution for gold octahedron nanoparticles was prepared by mixing 9.5 ml of 100 mM CTAC, 250 μl of 10 mM gold chloride trihydrate, and 5 μl of 10 mM potassium iodide solution. The growth was started by the injection of 220 μl of 40 mM ascorbic acid solution and 55 μl of diluted spherical seed solution. The growth continuced for 15 minutes in 30°C water bath. The solution was centrifuged twice (12,000rpm 3min) and redispersed in 1 mM CTAB solution for future use.

Synthesis of chiral nanoparticles

The growth solution for chiral nanoparticles was prepared by adding 800 µl of 100 mM CTAB and 100 µl of 10 mM gold chloride trihydrate into 3.95 ml of deionized water to form an $[AuBr4]^-$ complex. Au^{3+} was then reduced by the rapid injection of 475 µl of 100 mM ascorbic acid solution. With the addition of 5 µl of dipeptide solution and 50 µl of seed solution, the nanoparticle growth was started. The growth continuced for 2 hours in 30°C water bath. For a typical synthesis, 2 mM of γ-Glu-Cys solution and 0.15 mM of Cys-Gly solution were used to encode chirality onto the nanoparticles. The nanoparticle solution was centrifuged three times (6000rpm 60s) and redispersed in 1 mM CTAB for further characterization.

3.2 Synthesis of Chiral Cobalt Oxide Nanoparticles

Chemicals

All peptides (98%) were purchased from BeadTech Inc. (Korea) and used without further purifications. Cobalt(II) chloride hexahydrate (97%) was purchased from Junsei (Japan). Sodium citrate tribasic dehydrate (99%), sodium borohydride ($NaBH_4$, 98%) were purchased from Sigma-Aldrich. All aqueous solutions were prepared using high-purity deionized water (18.2 MΩ cm^{-1}).

Synthesis of chiral cobalt oxide nanoparticles

Chiral cobalt oxide nanoparticles were synthesized through a solution-based growth method. For typical synthesis, 0.5 ml of 0.1 M $CoCl_2$, 0.75 ml of 0.1 M Na citrate, and 6.25 ml of 0.01 M YYC aqueous solution were added to 1.875 ml of deionized water. After stirring at RT for 30 min, 0.625 ml of 0.1 M $NaBH_4$ was injected followed by aging under stirring for 2 h at room temperature. As the reaction proceeded, the pink color of the growth solution gradually turned brown. The synthesized nanoparticles were analyzed after dialysis using a 1 kDa MWCO membrane.

Synthesis of achiral cobalt oxide nanoparticles

Achiral cobalt oxide nanoparticles were synthesized through a hydrothermal method. Cobalt(II) acetate tetrahydrate (1 g) was dissolved in 50 ml of ethanol under stirring at 45 °C for 10 min, followed by dropwise addition of 6.6 ml of ammonia solution (25%). The mixture was transferred into Teflon-lined autoclave and maintained at 150 °C for 3 h. After synthesis, the crude solution was mixed with 200 ml of acetone and centrifuged twice at 135000 rpm for 20 min. The

final product of nanoparticles was dispersed in deionized water for further analysis.

3.3 Synthesis of Chiral Gold-Silica Core-Shell Nanoparticles

Chemicals

Tetraethyl orthosilicate (TEOS, 99%) was purchased from Sigma-Aldrich and mPEG-SH (MW 5,000) was purchased by Biochempeg. All aqueous solutions were prepared using high-purity deionized water (18.2 MΩ cm−1).

Synthesis of chiral gold-silica core-shell nanoparticles

Before silica coating, 0.3 mL of 0.25 mM mPEG-SH aqueous solution was added under vigorous stirring to 10 mL of pre-synthesized helicoid solution, and the reaction was continued for 30 min. The mixture was centrifuged twice at 6000 rpm for 5 min and redispersed in ethanol. For silica coating, 1.2 mL of mPEG-SH capped helicoid solution was injected to 1 mL of DI water followed by addition of 2.3 mL of ethanol and 0.42 mL of 2 M NH_4OH solution. The reaction was started by the addition of 90 μL of TEOS solution (40 vol % in IPA) under vigorous stirring. After 2 h, the particle solution was centrifuged three times, and dispersed in ethanol for further characterization.

3.4 Optical Characterization of Chiral Nanostructures

Optical Characterization

Circular dichroism (CD) spectra of chiral nanoparticles were obtained using a J-815 spectropolarimeter instrument (JASCO). Kuhn's dis-symmetry factor (g-factor) was calculated from the measured CD value and extinction using:

$$g\text{-factor} = 2\frac{A_L - A_R}{A_L + A_R}$$

SEM images were taken with SIGMA (Zeiss) and SUPRA 55VP (Zeiss).

Magnetic circular dichroism (MCD) spectra were measured with a J-815 spectropolarimeter instrument (JASCO) equipped with a 1.6 T (tesla) permanent magnet by using both the parallel and anti-parallel fields. Transmission electron microscopy (TEM) image was taken with JEM-2100F system (JEOL, Tokyo, Japan).

NMR spectroscopy

NMR spectra were collected at 298 K on Bruker Avance III HD 800 MHz spectrometer equipped with a z-gradient triple resonance cryoprobe. The NMR samples were prepared in deionized water with 10% (v/v) D_2O. NMR data were processed using the TopSpin3.5pl7 (Bruker) program, and analyzed using the NMRFAM-SPARKY program.[91] 2D TOCSY and 2D NOESY correlation experiments were used to assign the amide, alpha, and beta protons of the Tyr-Tyr-Cys peptides. Inter-proton distance restraints were obtained from the NOE spectra, and the classified distance ranges by the NOE peak intensities were used for structure calculation. Structures were calculated by simulated annealing using the

program CYANA 3.0.[92] The final 20 lowest-energy structures were visualized using PyMOL (Schrodinger, LLC).

Chapter 4. Dipeptide-Directed Chiral Gold Nanoparticles

4.1 Introduction

Metamaterials presenting high circular dichroism are practical interest as well as fundamental significance. In recent years, chiral metamaterials are highly demanded in various fields including optics, display, and sensing, due to their strong light-matter interaction.[93–97] Based on the unique optical properties and delicate structure, chiral metamaterials have extended the light manipulating abilities to negative refractive index,[98] control of angular momentum of light[99,100], holographic display,[101,102] and chiral sensing.[103–106] To elicit this unique properties, various attempts have been made to fabricate tailored chiral plasmonic metamaterials. Until now, methodologies such as top-down patterning[107,108] and nanosphere lithography[44,109] have been used for the fabrication of sophisticated chiral metamaterials including three-dimensional features. As another approach for chiral structure, utilizing helical self-assembly scaffold such as DNA[110–112], peptide[113], and cholesteric liquid crystal materials[114] have been demonstrated. However, despite numerous efforts, the complexity of the process and difficulty of control in below a hundred nanometer-scale still persist, and there is a need for a facile method for tailored chiral structure.

Recent advances in nanoparticle engineering enabled facile and scalable method for precise morphological control at nanoscale.[115–124] In particular, colloidal synthesis of noble metal nanoparticles has been extensively studied to tailor the morphology of nanoparticles. In colloidal methods, noble metal nanoparticles can be composed of well-defined crystal facets, whose surface atomic structures,

represented by Miller-indices, determine the morphology.[125] To control the crystal facets and nanoparticle morphology, surface absorbates that passivate the crystal facets with specific Miller-indices have been adopted. Various halide ions, metal ions and organic molecules have been reported to selectively expose various crystal facets with low- to high-Miller-indices. In addition, seed-mediated growth method has been exploited as an important strategy to control nanoparticle morphology.[76,90,126–128] Starting from small seed nanoparticles with well-defined low-Miller-index crystal facets, more complex morphologies composed of high-Miller-index crystal facets could be synthesized with high uniformity. Understanding the transition of Miller-indices during the synthesis and its correlation with morphology is the key to design the nanoparticles with desired properties.

Recently, we proposed a novel synthesis method to realize chiral morphology on gold nanoparticles by seed-mediated colloidal growth using amino acid and peptide as shape modifiers. Starting from 50-nm-sized low-Miller-index seed nanoparticles, cysteine and glutathione were introduced into the growth solution, resulting in chiral helicoid morphology. Synthesized chiral nanoparticles has named 432 helicoid series due to its unique 432 point group symmetry with broken mirror and inversion symmetry. The morphologies of 432 helicoid were formed by the interaction between the chiral molecules and the high-Miller-index facets formed during the growth process. The enantioselective adsorption of chiral molecules on asymmetric kink sites of high-Miller-index facets induced asymmetric growth between the facets with opposite chirality. An important advantage of this strategy is its excellent flexibility in tuning chiral shape as well as sophisticated shape control on the nanoscale. We have reported totally different structures of chiral gold nanoparticles by adjusting the synthesis parameters such as seed morphology and type of additive molecules to provide a broad understanding of the growth and

chirality evolution in gold nanoparticles. These results show not only the scalability of the strategy using chiral additives due to the presence of numerous chiral molecules in nature, but also that the resulted morphology can be systematically understood based on crystallographic analysis.

In this Chapter 4, the synthesis of chiral gold nanoparticles was reported using dipeptide gamma-glutamyl-cysteine (γ-Glu-Cys) and cysteinylglycine (Cys-Gly) as shape modifier.[129] We analyzed the growth pathway and chirality evolution of dipeptide-directed gold nanoparticles in crystallographic perspective. In the presence of γ-Glu-Cys, nanoparticle developed into a cube-like structure with protruded chiral wing with 4-fold symmetry. On the other hand, nanoparticle synthesized with Cys-Gly showed a rhombic dodecahedron-like outline, with largely curved edges and elliptical cavities in each face. Furthermore, three-dimensional geometric models of dipeptide-directed nanoparticles were constructed to provide crystallographic understanding of the chiral morphology of nanoparticles. Through time-dependent analysis, we observed that γ-Glu-Cys and Cys-Gly generated different intermediate morphologies, which were concave hexoctahedron and concave rhombic dodecahedron, respectively. Cys-Gly-directed nanoparticles were named as 432 helicoid V, due to their unique shape and growth pathway.

4.2 Solution-Based Synthesis of Dipeptide-Directed Chiral NPs

Chiral gold nanoparticles were synthesized by seed-mediated growth method, utilizing the enantioselective interaction between generated high-Miller-index facets and chiral dipeptides (Figure 4.1).[129] In this growth method, low-Miller-index-facet-exposed gold nanoparticles were prepared as seed nanoparticles. As a first step, 50-nm-sized octahedron shaped gold nanoparticles with {111} facet enclosed were prepared from 2-nm-sized spherical nanoparticles using the preferential attachment of iodine to {111} crystal facets. In the next step, the octahedron seed nanoparticles were grown for 2 hours in the growth solution consisting of the gold precursor, hexadecyltrimethylammonium bromide (CTAB), ascorbic acid, and dipeptide additives. During the growth, CTAB surfactant stabilized the {100} plane of gold nanoparticle, and ascorbic acid promotes growth along [111] direction as a reducing agent.[90,130] The competition between the effect of CTAB and ascorbic acid in the presence of the gold precursor exposed the high-Miller-index facets on the surface of the gold nanoparticles. The addition of chiral additives during the growth process induced the development of chiral structure. The enantioselective interaction of the chiral molecule with chiral kink sites caused asymmetric growth of high-Miller-index facets exposed on gold nanoparticles. This surface-level asymmetry induced by chiral dipeptides resulted in three-dimensional chiral morphology of gold nanoparticles.

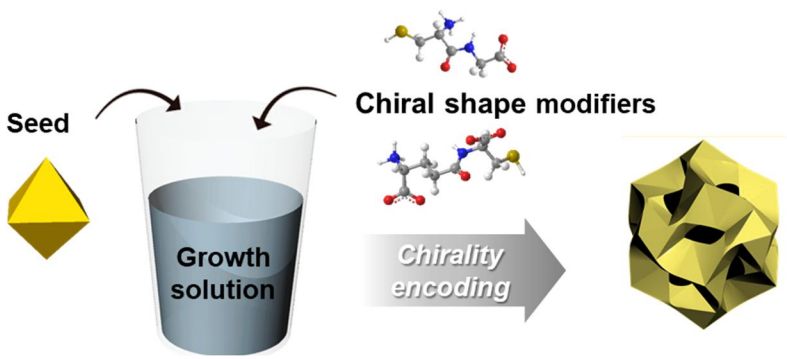

Figure 4.1 Scheme of seed mediated synthesis using octahedron seed nanoparticles as seeds. Dipeptides were injected into the growth solution as a chiral ligand.

The chiral dipeptides acted as shape modifiers and greatly influenced the final shape of synthesized gold nanoparticles. Depending on the type of chiral additive molecules added in the growth process, the gold nanoparticles underwent different morphological evolution, resulting in significantly distinguishable chiral morphologies and degree of chiral deformation. Previously, we reported synthesis of chiral morphology using an amino-acid and a tripeptide, cysteine and glutathione (GSH). As the molecules changed, there was a difference in the growth direction shifting the different boundaries of the common hexahedron shaped gold nanoparticle which is due to the difference in adsorption angle of cysteine and GSH to the high-Miller-index facet. Using cysteine and GSH, chiral gold nanoparticles with 432 symmetry have been synthesized with a marked difference in their chiral shape and named 432 helicoid I, II, III, and IV, demonstrating that additives play a pivotal role in evolution of chiral structure. In this study, dipeptides gamma-glutamyl-cysteine (γ-Glu-Cys) and cysteinylglycine (Cys-Gly) was used as shape modifier for synthesizing chiral gold nanoparticles (Figrue 4.2). As shown in Scheme 1b, γ-Glu-Cys is a sequence with gamma glutamyl functional group attached to N-terminus of cysteine, and Cys-Gly is a sequence with glycine group attached to C-terminus of cysteine. γ-Glu-Cys and Cys-Gly have intermediate sequences between cysteine and GSH (γ-Glu-Cys-Gly) for which chiral shape evolution has been reported, and are also an intermediates involved in the GSH biosynthetic pathway.[131] In a biosynthesis pathway, glutamate and cysteine are combined by the enzyme to form γ-Glu-Cys, which is then combined with glycine to yield GSH. Outside the cell, GSH is broken down to generate Cys-Gly and γ-glutamyl moiety. Studying the effect of dipeptide in chiral morphology evolution will be the cornerstone for understanding and ultimately designing the relationship between peptide sequences and chiral shape development.

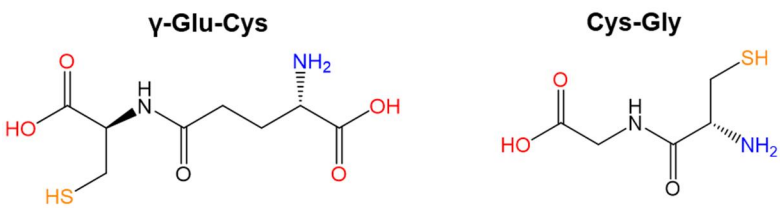

Figure 4.2 Structure of dipeptides, gamma-glutamyl-cysteine (γ-Glu-Cys) (left) and cysteinylglycine (Cly-Gly) (right).

Two dipeptide-directed gold nanoparticles exhibited completely different chiral morphology from each other. The following scanning electron microscopy (SEM) images represent chiral NPs synthesized using γ-Glu-Cys and Cys-Gly. The low magnification SEM images (Figure 4.3) shows that synthesized chiral gold nanoparticles exhibited uniform chiral shape and size of 150 nm.[129] As shown in Figure 1a, the nanoparticles synthesized using γ-Glu-Cys have a cube-like outline with protruded vertices. On the other hand, the NPs synthesized using Cys-Gly exhibit a rhombic dodecahedron-like outline, which is consisting of 12 rhombus and 24 edges. The morphological differences of two nanoparticles resulted in diverging chiroptic response. To observe chiroptical properties of synthesized particles, circular dichroism (CD) was measured and converted to Kuhn's dis-symmetry value (g-factor) as shown in Figure 4.4.[129] Nanoparticles synthesized with γ-Glu-Cys showed a positive main peak at wavelength 550 nm with g-value of 0.02. On the contrary, nanoparticles synthesized with Cys-Gly exhibited a negative main peak at 620 nm with g-value of 0.02. To fully understand the different chiral development driven by dipeptides, detailed analysis of chiral morphology from crystallographic perspective has been conducted as follows: morphology analysis, growth pathway analysis, and dipeptide-concentration-dependent analysis.

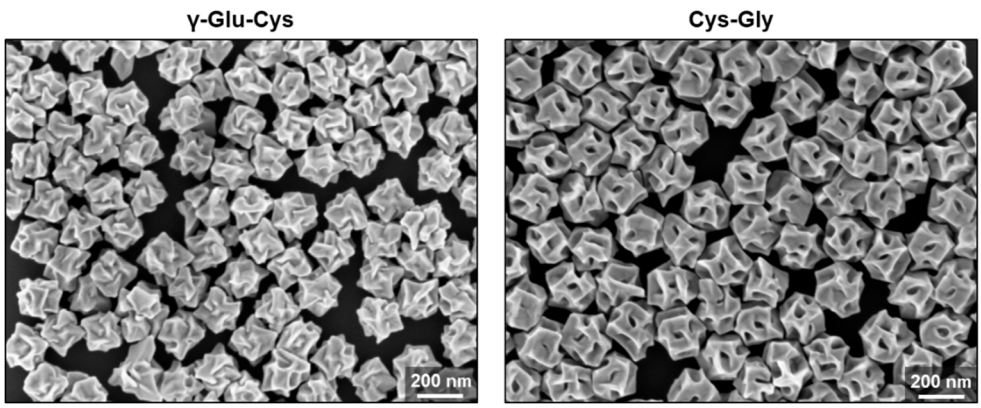

Figure 4.3 SEM images of chiral NPs synthesized using γ-Glu-Cys (left) and Cys-Gly (right). The scale bars are 200 nm.

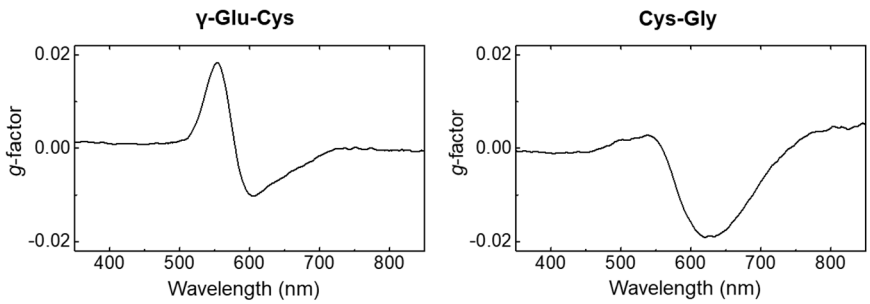

Figure 4.4 Dissymmetric factor spectrum of γ-Glu-Cys- (left) and Cys-Gly-directed nanoparticles (right). The difference in morphologies of the two nanoparticles exhibited diverging chiroptic responses in which γ-Glu-Cys showed a positive main peak and Cys-Gly showed a negative main peak.

4.3 Morphology Analysis of γ-Glu-Cys- and Cys-Gly-directed NPs

To understand the chiral morphology of synthesized nanoparticles, we contructed three-dimensional model of γ-Glu-Cys-directed 432 helicoid I and Cys-Gly-directed 432 helicoid V. The models were constructed based on the shape of nanoparticles from various crystallographic orientations, observed by SEM. Nanoparticles with 432 point group symmetry have 4-fold, 3-fold, and 2-fold symmetry axes on [100], [111], and [110] directions, respectively. The morphology observed in each direction shows the feature of each symmetry constituting the nanoparticles, providing the necessary information to understand the entire geometry. To construct the models that satisfies 432 symmetry, we first constructed a 2-fold rhombus face that corresponds to one-twelfth of all surfaces, and rotated it around 4-fold and 3-fold axes. The models of γ-Glu-Cys- and Cys-Gly-directed nanoparticles showed their clearly distinguishable morphologies despite the same point group symmetry.

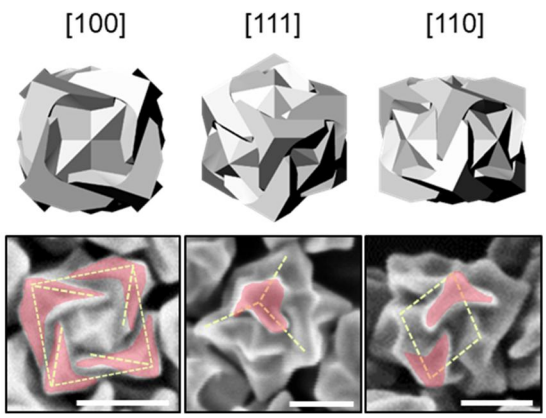

Figure 4.5 Schematics and corresponding SEM images of nanoparticles synthesized with γ-Glu-Cys, as viewed along [100] (left), [111] (middle), and [110] (right) directions. To highlight chiral features, the protruded wings were colored red and tilted edges were highlighted with yellow-dotted lines. Scale bars are 100 nm.

The γ-Glu-Cys-directed nanoparticles exhibited cube-like morphology with twisted and protruded tripod edges at each vertex, which is characteristic of 432 helicoid I (Figure 4.5).[129] These structures can be understood as splitting and tilting of the edges connecting two vertices, which break the mirror symmetry and result in chiral morphology. Along the [100] direction, the four edges tilted toward the center of cubic face form the 4-fold morphology (Figure 4.5, left). Along the [111] direction, three edges extending from a vertex are tilted clockwise and form the 3-fold morphology (Figure 4.5, middle). When viewed in the [110] direction, a pair of edges facing opposite direction from each other form the 2-fold chiral morphology (Figure 4.5, right). On the contrary, Cys-Gly-directed nanoparticles synthesized using Cys-Gly exhibited a unique chiral structure of twisted rhombic dodecahedron with elliptical cavities at the center of each faces, which has not been reported previously (Figure 4.6). The chiral morphology of Cys-Gly-directed nanoparticles was characterized by a set of arched edges surrounding a 2-fold symmetric cavity. From [100] view and [111] view, these edges are arched to clockwise and anti-clockwise respectively, composing the pinwheel-like 4-fold and 3-fold morphology (Figure 4.6, left and middle).[129] Along the [110] direction, the edges facing each other are bent in the same direction, inward or outward, forming the 2-fold morphology (Figure 4.6, right). We named this nanoparticle synthesized using Cys-Gly as 432 helicoid V, owing to its point group symmetry and unique morphology.

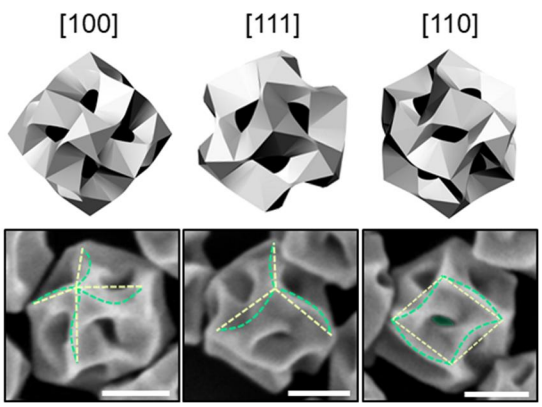

Figure 4.6 Schematics and corresponding SEM images of nanoparticle synthesized with Cys-Gly, as viewed along [100] (left), [111] (middle), and [110] (right) directions. The green-dotted lines on the SEM images depict that the edges of the particle are highly curved with respect to the rhombic dodecahedron outline (yellow-dotted line). The chiral cavity viewed along [110] direction was colored green. Scale bars are 100 nm.

4.4 Time-Dependent Analysis of Chiral Morphology Development

To understand the different morphology evolution of dipeptide-directed nanoparticles, intermediate morphologies during nanoparticle growth were analyzed in detail. Figure 4.7 shows time-dependent SEM images of gold nanoparticles grown in the presence of γ-Glu-Cys and Cys-Gly.[129] Both particles started from octahedron with exposed {111} facets and grew to rhombic dodecahedron with exposed {110} facets after 4 minutes. Then preferential growth of edges and vertices of rhombic dodecahedron resulted in concave nanoparticles with high-Miller-index surface facets. After 20 minutes of growth, the difference in the morphologies directed by γ-Glu-Cys and Cys-Gly became noticeable. When γ-Glu-Cys was presence, a pair of tilted edges were formed at [110] direction. As the growth proceeds, these edges continued to elongate and thicken, forming the final twisted wing-like chiral structure. On the contrary, for Cys-Gly case, a tilted concave valley surrounded by curved edges of rhombic dodecahedron was formed after 20 minutes. As these edges protruded and arched further, a pinwheel-like morphologies at the [100] and [111] vertices were generated, and the tilted valleys changed into elliptical cavities.

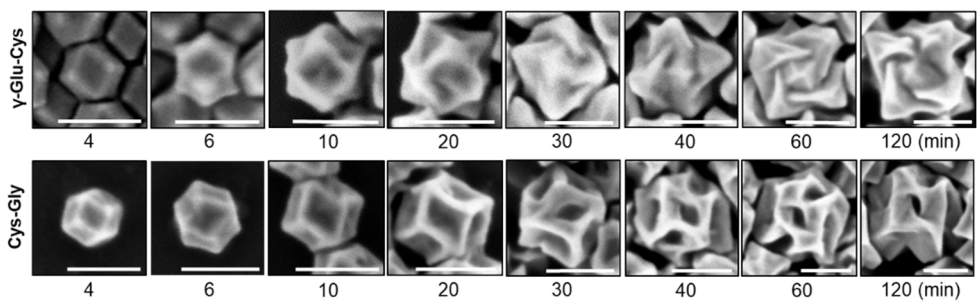

Figure 4.7 SEM images of γ-Glu-Cys- (top) and Cys-Gly- (bottom) induced chiral nanoparticles depending on the growth time. Scale bars are100 nm.

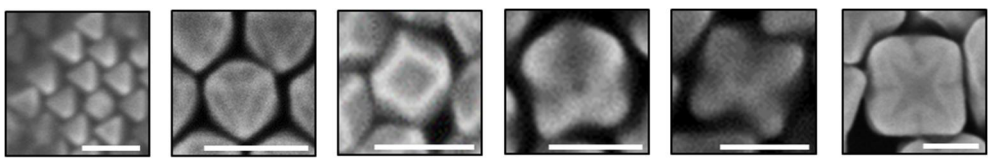

Figure 4.8 SEM images of the time-dependent growth of octahedron nanoparticle without chiral additive. Octahedron nanoparticle grows into rhombic dodecahedron and further grows into hexoctahedron.

At the intermediate stage of growth, the chiral morphology of γ-Glu-Cys-directed nanoparticles was developed as the mirror symmetry between high-Miller-index facets is broken. In our growth solution without peptide additives, octahedron seeds were grown to concave hexoctahedron nanoparticles (Figure 4.8),[129] which consist of 48 triangular facets belonging to same high-Miller-index family. As shown on the left in Figure 4.9, a concave hexoctahedron has the same area for every crystal facet, thus having achiral $4/m\,\bar{3}\,2/m$ point group symmetry. When γ-Glu-Cys was presence in the growth solution, its enantioselective interaction to chiral kink sites induce different growth rate for high-Miller-index facets with opposite chirality. As a result, the mirror symmetry between adjacent facets with opposite chirality was broken. As shown on the right side of Figure 4.9, in rhombus ABA'B', the BC and B'C boundaries were tilted toward yellow-colored ABC and A'B'C planes, increasing the area of cyan-colored AB'C and A'BC planes and forming the new red-patterned BCD and B'C'D' planes. The 12 equivalent rhombus of the concave hexoctahedron changed in the same manner, breaking the mirror symmetries in the particle and changing the point group symmetry to 432. This seires of changes form the characteristic chiral tilted edges of 432 helicoid I (Figure 4.9, bottom).[129]

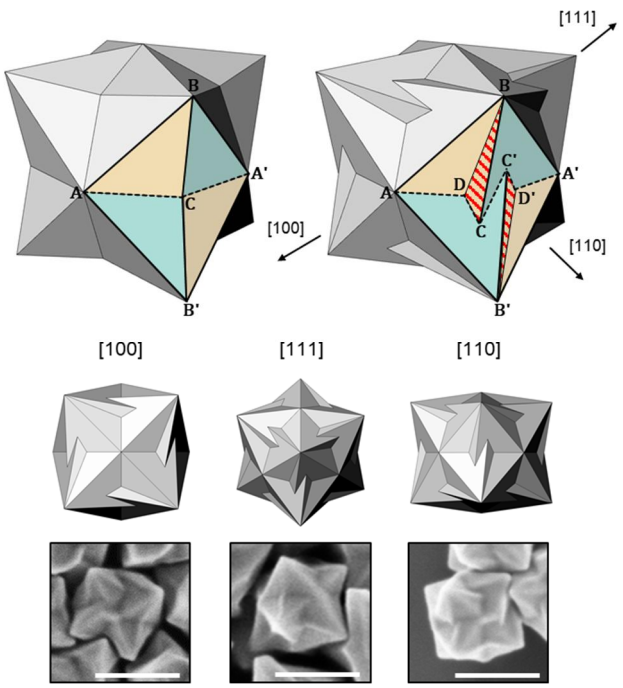

Figure 4.9 Schematics of intermediate morphologies during nanoparticle growth in the presence of γ-Glu-Cys (top). Adjacent facets with opposite chirality were colored yellow and cyan. Convex edges are indicated by solid lines and concave edges by dotted lines. Schematics and corresponding SEM images of intermediate morphologies of chiral nanoparticles with γ-Glu-Cys, as viewed along [100], [111], and [110] directions (bottom). Scale bars are 200 nm.

On the contrary, 432 helicoid V showed a completely different growth pathway from ordinary growth condition, and developed chiral morphology based on concave rhombic dodecahedron (Figure 4.10).[129] A concave rhombic dodecahedron is defined by 48 surface facets belonging to a high-Miller-index family, which is identical to a concave hexoctahedron. Therefore, two polyhedrons have the same point group symmetry of $4/m\,\bar{3}\,2/m$. The difference between the two polyhedrons can be found in the concavity of the edges; concave rhombic dodecahedron has concave AC and BC edge in rhombus ABA'B', while concave hexoctahedron has concave AC edge and convex BC edge (Figure 4.9 and 4.10). Asymmetry growth between surface facets with opposite chirality changed the point group symmetry and developed the chiral morphology of 432 helicoid V. However, the surface facets with increasing area for the two particles were different, and the 432 helicoid V increases the area of ABC and A'B'C and newly forms ACD and A'C'D' planes. In this process, the CC' edge, which was previously unobservable, was developed as a characteristic concave and tilted valley structure of 432 helicoid V. The straight boundaries of rhombus ABA'B' were also deformed so that AB and A'B' edges arched inward and AB' and A'B edges arched outward. These edges composed the 4-fold and 3-fold pinwheel-like structure, which was observable from [100] and [111] directions, respectively (Figure 4.10, bottom). As the growth proceeded, these edges enlarged and protruded, forming the cavity structure of 432 helicoid V.

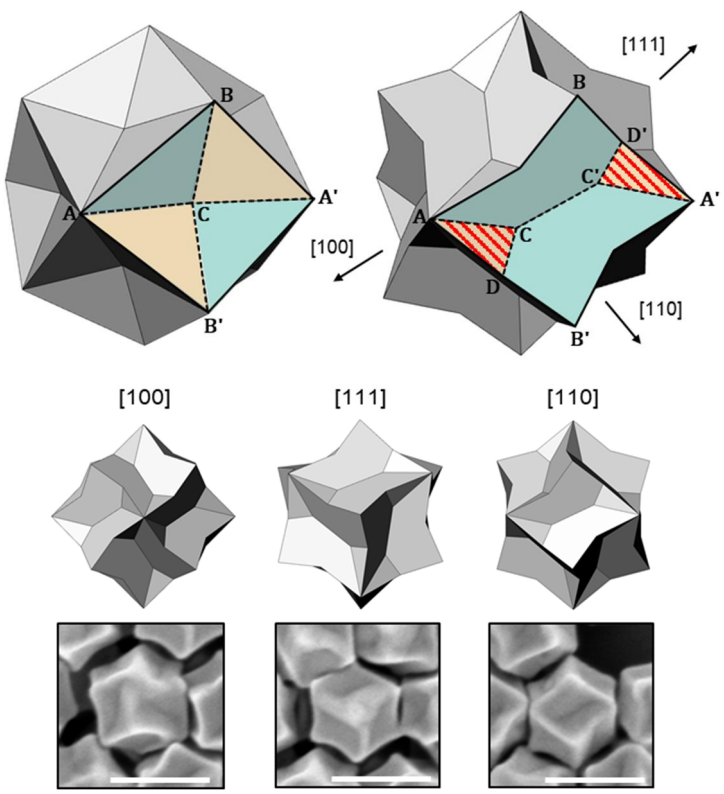

Figure 4.10 Schematics of intermediate morphologies during nanoparticle growth in the presence of Cys-Gly (top). Adjacent facets with opposite chirality were colored yellow and cyan. Convex edges are indicated by solid lines and concave edges by dotted lines. Schematics and corresponding SEM images of intermediate morphologies of chiral nanoparticles with Cys-Gly, as viewed along [100], [111], and [110] directions (bottom). Scale bars are 200 nm.

From the growth of γ-Glu-Cys- and Cys-Gly-directed nanoparticles, it was observed that 1) the chiral morphologies were formed by extension of crystal facets with certain chirality, 2) the surface Miller-indices of exposed facets were maintained during morphological evolution, 3) different chiral morphologies were induced *via* different intermediate morphologies, which depend on the peptide sequences. In detail, the chiral morphology of γ-Glu-Cys- and Cys-Gly-directed nanoparticles were formed on high-Miller-index faceted particles, by preferential growth of the facets with certain chirality. Interestingly, the Miller-indices of these facets remained unchanged during the growth, and consisted the final chiral morphology of 432 helicoid I and V. This suggests that the role of peptides on the formation of chiral morphology is selective passivation and exposure of certain high-Miller-index facets. Moreover, γ-Glu-Cys and Cys-Gly induced different surface Miller-indices and intermediate morphologies. This clearly shows that the molecular structure of dipeptides determine the interaction with high-Miller-index facets, supporting the proposed mechanism.

4.5 Concentration-Dependent Chiral Morphology and Chiroptical Responses

Based on the understanding of the chiral morphology evolution, the effect of peptide concentration on chirality expression was explored. Changes in peptide concentration can directly affect the morphology by controlling asymmetric input, such as local strain and steric hindrance on certain growth direction.[132] Depending on the peptide concentration, the degree of chiral deformation changes, i.e. the degree of twist, protrusion of the edges, and the development of chiral structures such as wings and gaps. To explore the effect of dipeptide concentration on chiral shape evolution, the degree of chiral deformation and the resulting chiroptical signal were investigated by varying peptide concentration injected during the synthesis.

Chiral morphologies of nanoparticles synthesized with γ-Glu-Cys at various concentration from 1 to 4 μm were investigated by SEM analysis, as shown in Figure 4.11.[129] To compare the chiral structure depending on the molecular concentration, the protruding vertices seen at three view point were connected by yellow dotted line, and the trace of chiral wing was colored in red. The chiral NP synthesized by injection of 1 μM γ-Glu-Cys exhibits edges that were split into two and twisted, breaking the mirror symmetry, thus generating chirality. Increasing molecular concentration to 2 μM generated clear wing structures bent with greater curvature. When viewed from [110] direction and [111] direction, the 2-fold and 3-fold symmetry of this chiral wings are observed. Further increase in concentration resulted in dendritic structure due to the over grown arms indicating that optimum concentration exists for chiral structure. At high peptide concentrations, the weak bonding of amine and carboxylic groups would be interfered thus decreasing enantioselectivity. To observe chiroptical properties of synthesized particles at

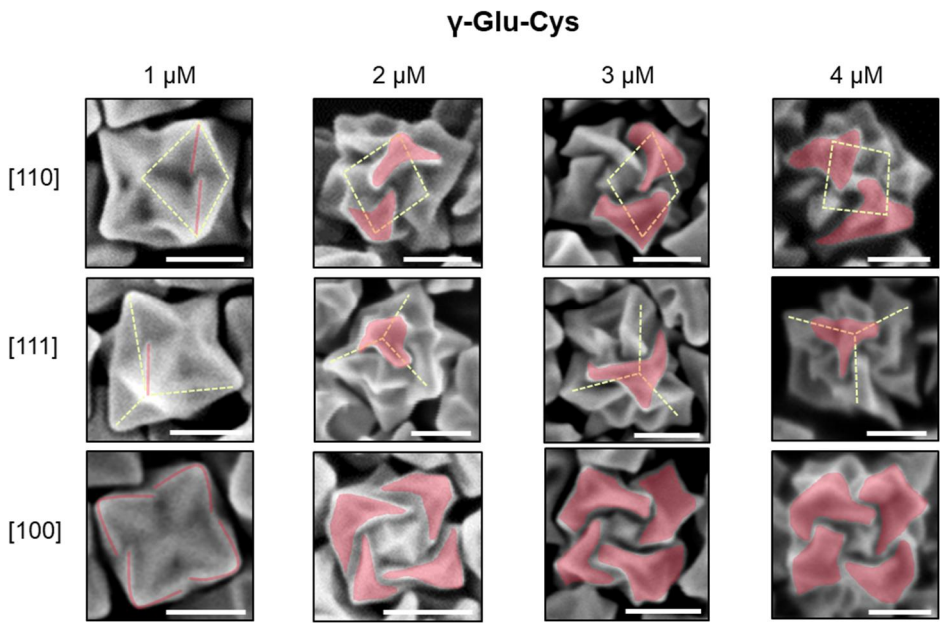

Figure 4.11 SEM images of nanoparticle synthesized in the presence of γ-Glu-Cys at various concentration from 1 to 4 μM. The particles are viewed from [110], [111], and [100] directions. Scale bars are 100 nm.

various γ-Glu-Cys concentration, *g*-factor spectra were measured as shown in Figure 4.12 and 4.13.[129] Nanoparticles with clear chiral motif synthesized with 2 μM of γ-Glu-Cys showed the largest *g*-value of 0.02 and a positive main peak at wavelength 550 nm. Further increase in concentration of γ-Glu-Cys resulted in reduced CD signal, which is due to the decreased chirality of dendritic structure. The optimum peptide concentration that led to the highest *g*-value was 2 μM for γ-Glu-Cys, similar to 5 μM for previously reported glutathione case and higher than 0.1 μM for cysteine case.[87]

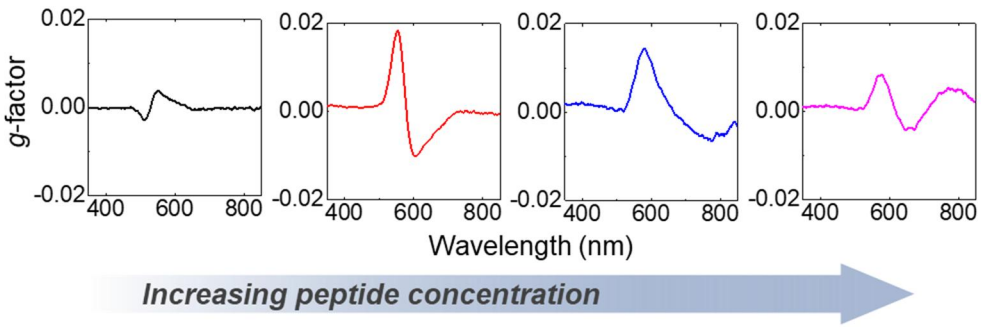

Figure 4.12 The g-factor spectra of nanoparticles synthesized in the presence of γ-Glu-Cys at various concentration from 1 to 4 μM.

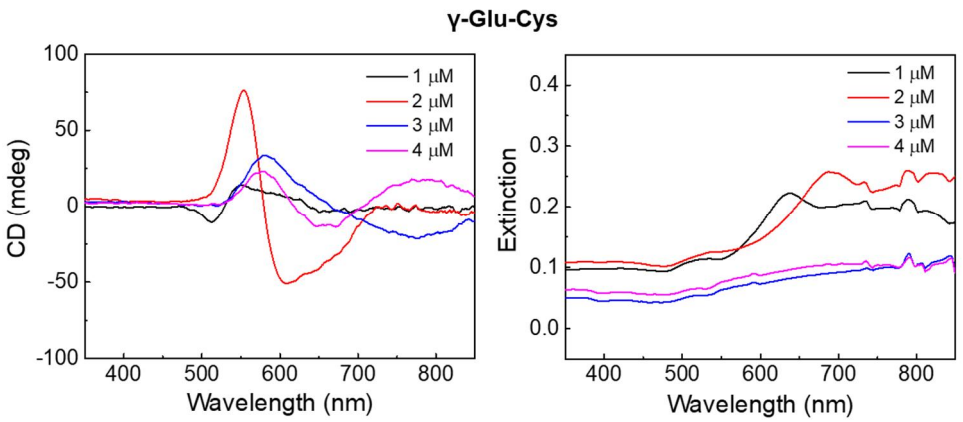

Figure 4.13 Effect of dipeptide concentration on chiroptical response of chiral nanoparticles. CD spectra (left) and extinction spectra (right) of nanoparticles synthesized with γ-Glu-Cys at various concentration from 1 to 4 μM.

In contrast to the effects of γ-Glu-Cys concentration on morphology, the concentration of Cys-Gly during the growth affects the degree of chiral deformation where the edges are bent and cavities are formed. Figure 4.14 shows SEM images of chiral nanoparticles synthesized with Cys-Gly at various concentration from 0.05 to 0.18 μM.[129] For better understanding and direct comparison of the effect of molecular concentrations on chiral shape edges are indicated by dotted green lines and the cavity is colored green. In the presence of 0.05 μM Cys-Gly, NPs exhibit pinwheel-like chiral structures with counterclockwise rotation when viewed from [111] and clockwise rotation in [100] direction. Observation from the [110] aligned view also shows concave boundary in the middle of rhombus which is tilted breaking the mirror symmetry. As the molecular concentration increased from 0.05 μM to 0.1 and 0.15 μM, the curvature of the bent edges increased, resulting in significantly twisted edges. In addition, the tilted valley in the [110] aligned view at low concentration developed into an elliptical cavity structure. These highly curved edges and cavity structures generated an enhanced chiroptical response, resulting in the highest *g*-factor of 0.02 for 432 helicoid V with a negative peak main peak at 620 nm at 0.15 μM concentration (Figure 4.15 and Figure 4.16).[129] This optimum concentration is comparable to previously reported cysteine case, and lower than γ-Glu-Cys and glutathione cases.[87] As the peptide concentration further increased to 0.18 μM, the curved edges were overgrown, resulting in randomly distorted edges. Due to the dendritic structure, the *g*-value of the main peak decreases and red-shift in the 0.18 μM case.

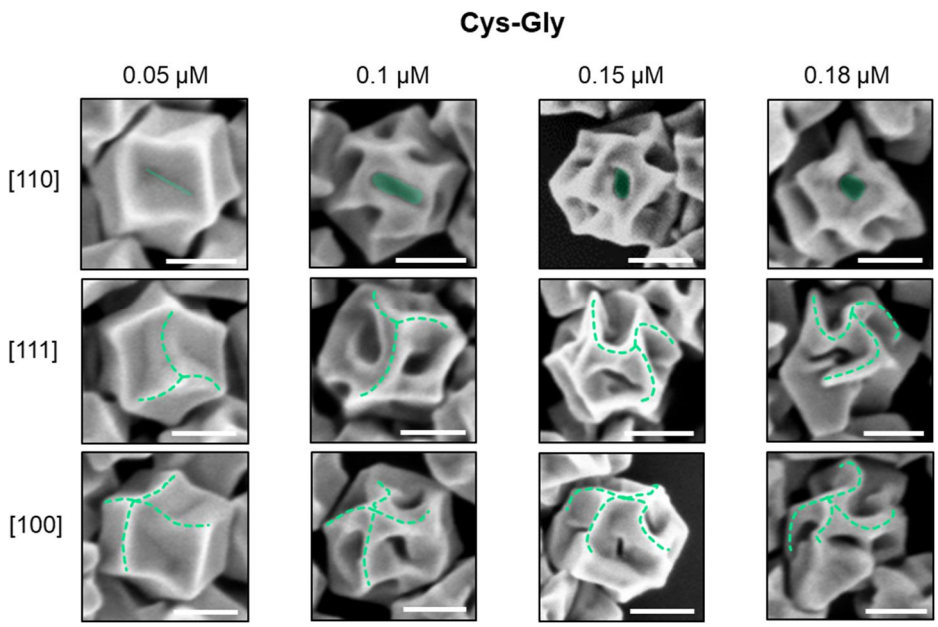

Figure 4.14 SEM images of nanoparticle synthesized in the presence of Cys-Gly at various concentration from 0.05 to 0.18 µM. The particles are viewed from [110], [111], and [100] directions. Scale bars are 100 nm.

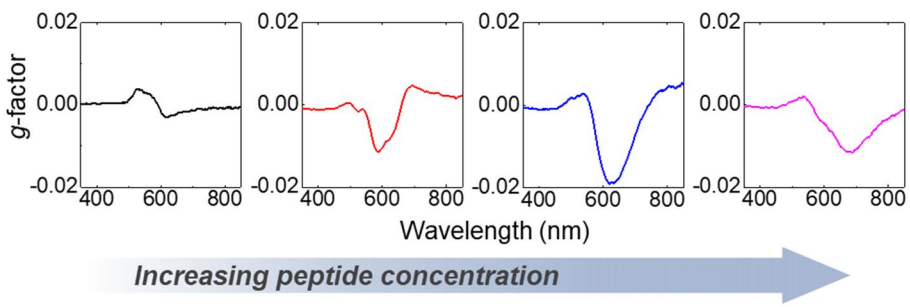

Figure 4.15 The g-factor spectra of nanoparticles synthesized in the presence of Cys-Gly at different concentration from 0.05 to 0.18 μM.

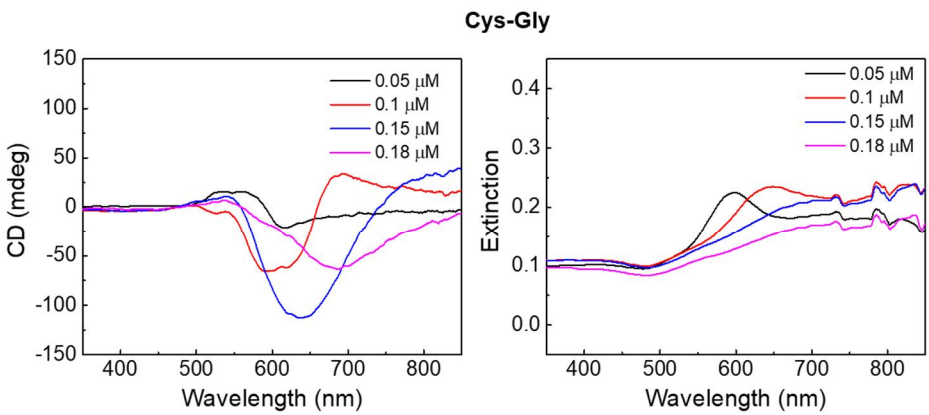

Figure 4.16 Effect of dipeptide concentration on chiroptical response of chiral nanoparticles. CD spectra (left) and extinction spectra (right) of nanoparticles synthesized with Cys-Gly at various concentration from 0.15 to 0.18 μM.

Furthermore, to clearly compare chirality expression using two dipeptides, we analyzed the surface coverage of γ-Glu-Cys and Cys-Gly for octahedral seed nanoparticles in the growth solution. To convert the dipeptide concentration to the surface coverage, we estimated the concentration of the nanoparticles to be 1.53×10^9 ml^{-1} using previous method.[87] Accordingly, the optimum dipeptide surface coverage that expresses the optimal chirality is 0.15 nmol mm^{-2} in the case of γ-Glu-Cys, and 0.011 nmol mm^{-2} in the case of Cys-Gly.

Sophisticated chiral structure and enhanced chiroptic properties of nanoparticles originated from the synergetic interplay between crystal growth and chirality formation. Previously, we have demonstrated a determinant role of CTAB and ascorbic acid on nanoparticle growth. In our growth solution, CTAB preferentially passivates {100} facet while ascorbic acid forms kinetically driven shape by affecting gold ion reduction rate. Consequently, the combinations of CTAB and ascorbic acid induce diverging crystallographic direction and morphology.[125,133]

Competing with this crystal growth, peptide determines the kinetics of chiral deformation. At low peptide concentration, the decreased kinetics of chiral deformation compared to crystal growth resulted in under-developed chiral features. At optimum concentration, chiral deformation was expedited thus generating chiroptic responses and clear chiral features. The excessive interaction between peptide and gold surface at higher concentration resulted in overgrown or dendritic morphologies. These correlations explored suggest that the evolution of chiral structure with enhanced chiroptical properties can be achieved by understanding and coordinating the cooperative interplay of crystal growth and chirality formation.

4.6 Sequence Effects

Taken together, we propose the role of each amino acid in the investigated peptides during the process of the chiral morphology evolution. The optimum concentration can reflect the binding affinity between peptides and high-Miller-index planes of gold surface. The fact that the optimum concentration of γ-Glu-Cys was about ten times higher than cysteine and Cys-Gly but slightly lower than GSH suggests that the flexible γ-peptide linkage in N-terminal can significantly weaken the binding. Another observation is that glycine in C-terminal can change the growth mechanism from the 432 helicoid I pathway observed in cysteine and γ-Glu-Cys cases to the 432-helicoid-III-like pathway. But it is worthy to mention that the initial pathway similar to 432 helicoid III gradually diverged to a new pathway, defined here as 432 helicoid V. From this experimental evidence, we postulate that the glycine in C-terminal can play an important role in directing the growth of particle toward more concave morphology, which eventually develops to the chiral cavity structure.

4.7 Conclusion

In summary, we demonstrated the synthesis of three-dimensional chiral gold nanoparticles using dipeptide γ-Glu-Cys and Cys-Gly. The geometry of dipeptide-directed nanoparticles was analyzed and modeled from a crystallographic perspective. The dramatic difference of two dipeptides on chiral development were analyzed in terms of the final morphology, growth pathway, and peptide concentration. The representative morphology of γ-Glu-Cys-directed nanoparticles showed a cube-like outline with protruded chiral wing with 4-fold symmetry. On the other hand, the nanoparticle synthesized in the presence of Cys-Gly exhibited a rhombic dodecahedron-like outline, with curved edges and elliptical cavities on each face. Cys-Gly-directed nanoparticles with chiral morphology was named as 432 helicoid V, owing to its unique growth pathway and morphology. Resulting from the morphological differences, two nanoparticles displayed diverging chiroptic response as γ-Glu-Cys produced a positive main peak and Cys-Gly produced a negative main peak. Intermediate morphology anslysis indicated gold nanoparticles synthesized with γ-Glu-Cys followed an intermediate morphology of concave hexoctahedron, while the nanoparticle synthesized with Cys-Gly formed a concave rhombic dodecahedron. These two clearly distinct intermediate morphologies provided a separate starting point for chiral development. The analysis of the effect of peptide sequences on chiral shape development suggests the infinite scalability of peptide incorporation during nanoparticle growth. In addition, the crystallographic modeling of the chiral morphology of nanocrystals provides the foundation for understanding the three-dimensional structure of chiral nanomaterials and resulting chiroptic response to ultimately design morphologies and properties for versatile applications.

Chapter 5. Peptide-Directed Chiral Cobalt Oxide Nanoparticle

5.1 Introduction

Metamaterials and properties for versatile applications. Chiral inorganic nanomaterials have been in the limelight of fundamental understanding of the relationship between chirality and physical properties since the discovery of the different rotations of linearly polarized light in quartz crystal in 1811.[134] Due to the strong light-matter interaction, there has been increasing demand for chiral inorganic nanomaterial in various fields such as optics, bio-sensing, and display. In recent years, the development of such chiral inorganic nanomaterials has been expanding to the realization of exceptional abilities to manipulate light presenting negative refractive index,[20,98] holographic displays,[101,102] and control of angular momentum of light.[99,100,135] Although the fundamental studies and technological fabrication of chiral nanomaterials have been mainly focused on metals, chiral metal oxide nanomaterials which can control the light and biochemical reactions have triggered huge interests owing to their applicabilities.[136–139] Considering the catalytic activity and biocompatibility,[140] development of chiral metal oxide nanomaterials could open up versatile applications for biomimetic catalysts and medical devices.

Recent two decades, controllable and scalable methods of synthesizing chiral inorganic nanoparticles have been actively pursued using biomolecules including amino acids,[75,76,141–143] peptides,[70,144,145] and DNA.[111,112,128,146] In the biological system, chiral structures develop utilizing chirality transfer from molecules to crystals, and beautiful examples of which can be found in snails,

gastropods, and butterfly wings.[2,147] By mimicking chirality transfer of the nature, various nanomaterials such as chiral gold cluster,[148] CdS,[149] CdTe,[150] ZnO,[75] and Co_3O_4[137] were developed by peptides and biomolecules, typically cysteine and glutathione. These nanocrystals with chirally distorted lattice exhibited chiroptic signal even in visible range of light. Recently, we developed a synthesis platform for chiral gold nanoparticles using cysteine and cysteine-containing peptides that strongly interact with inorganic surfaces.[87,129,133] Utilizing the enantio-selective interaction of the peptides, synthesized nanoparticles showed mirror-imaged structural chirality and resulting chiroptic responses according to the handedness of the chiral ligand used during the synthesis.

In order to understand and design the mechanism by which the peptide evolves chirality in nanocrystals, it is important to understand the binding and configuration of the peptide on the crystal surface. The exceptional ability of peptide that interacts with the inorganic surfaces results in the reconstruction of local atomic conformation and evolves a macroscopic chiral structure.[151] The functional groups of peptides including the amine groups, thiol groups, and carboxylic groups interact with the inorganic surface forming strong and weak bonding. These interactions cause local distortion of the inorganic materials to develop a chiral structure, generating chiroptic responses even in the visible range of light. Considering the role of peptide as a chirality inducer, the configuration and binding properties of peptides are highly important in chirality evolution using the peptide-inorganic interaction.[125,152] In this context, many efforts have been made to analyze the surface state of the ligand using DFT and molecular dynamics simulation.[137,138,140] Yeom et al. fabricated a chirally distorted Co_3O_4 crystal using L-, D-cysteine molecule, and analyzed the CD response through computational study using a model nanoparticle.[137] In addition, Le et al. analyzed the orbital

couplings between the chiral ligands and cysteine-decorated molybdenum oxide nanoparticles utilizing time-dependent density functional theory (TDDFT) simulation,[138] and Jiang et al. demonstrated that the packing of WO_3 lattice was distorted after L-, D-aspartic acid was adsorbed on the surface through molecular dynamics simulation.[140] Despite these efforts, there was lacking experimental and direct evidence showing the configuration of peptide on the surface for in-depth understanding.

Existing studies on chiral metal oxides have focused on the expression of chirality using a single amino acid. However, in order to understand the mechanism of chirality development and to achieve scalable chiroptic responses, sequence expansion to peptides is an essential step. In this regard, peptides including tyrosine and cysteine, which have received a lot of attention recently due to their versatile applicability as self-assembled structures and peptide-inorganic hybrid materials,[153–156] are suitable candidates for the development of chiral functional peptide-based materials. Tyrosine with phenolic functional group is an important amino acid in controlling the structural conformation in proteins, and its redox-active property promotes the charge transport by proton-coupled electron-transfer reactions in natural systems.[157,158] The thiol side chain in cysteine also serves an important structural role in many proteins.[159] Inspired by the fascinating properties of tyrosine and cysteine, our group developed an assembling motifs composed of short peptides with tyrosine and cysteine to investigate their structure and potential applications.[160] The detailed structure of the YYACAYY dimer which was assembled into macroscopic 2D nanosheets was revealed by 2D nuclear magnetic resonance (NMR) spectroscopy. In the revealed structure, the phenolic groups of tyrosine were facing towards the solvent to form a α-helical secondary structure, and cysteine provided folding stability through disulfide bridges which were

essential for assembly. Based on the tremendous potential of tyrosine and cysteine as structural and functional materials, we believe that peptide composed of tyrosine and cysteine can be applied to the development of chiral functional peptide-based materials. Furthermore, we intend to discuss the structure of peptides that impart unique characteristics to materials thorough 2D NMR study.

In Chapter 5, we report the synthesis of chiral cobalt oxide nanoparticles using Tyr-Tyr-Cys peptide ligand. The L-, and D-Tyr-Tyr-Cys-directed cobalt oxide nanoparticles exhibited mirror-symmetric chiroptic responses with a dis-symmetry factor (g-factor) of 0.01 in the UV and visible light regions. Through the control of synthetic parameters Tyr-Tyr-Cys, citrate, and $NaBH_4$, the mechanism of particle formation was analyzed, and synthetic conditions were optimized. In addition, the 3D structure of the Tyr-Tyr-Cys ligand on the surface of the nanoparticle was determined by 2D nuclear magnetic resonance (NMR) spectroscopy. This result inferred that the thiol group and carboxylic group of Tyr-Tyr-Cys were aligned in a single direction and strongly interacted with the nanoparticle surfaces, thereby providing in-depth understanding of the configuration and binding of the peptide ligand. Furthermore, through the sequence effect studies, the pivotal role of the C-terminal carboxylic group of Tyr-Tyr-Cys to develop nanoparticles was analyzed. In addition, the use of peptide ligands of different sequences produced dissimilar chiroptic responses, suggesting the important role of the peptide functional group as well as the scalability of chiral nanomaterial synthesis using peptides. Owing to the intrinsic chirality and magnetic properties of the chiral cobalt oxide nanoparticles, the chiroptic properties which were considered a permanent feature of the material could be modulated by an external magnetic field.

5.2 Synthesis of Chiral Cobalt Oxide Nanoparticles using Tyr-Tyr-Cys

Chiral cobalt oxide nanoparticles were synthesized through a solution-based growth method, exploiting the structure-guiding properties of the peptide ligand (Figure 5.1).[161] Cobalt chloride, sodium citrate, and Tyr-Tyr-Cys were used as a cobalt ion source, cobalt ion stabilizer, and a chirality inducer, respectively. Possessing cysteine which provides high affinity metal binding due to its thiol group, and tyrosine with a redox-active phenolic group that facilitates proton-mediated electron transport, Tyr-Tyr-Cys is a suitable candidate for a peptide ligand. To synthesize chiral cobalt oxide nanoparticles, a growth solution was prepared by mixing cobalt chloride and sodium citrate stabilizing the Co(II) ion. The color of the solution was pink because of the cobalt divalent ion. To encode chirality, Tyr-Tyr-Cys was added to the growth solution and stirred for 30 minutes. The reaction started with the addition of $NaBH_4$ reducing agent. As the reaction proceeded, the pink color of the growth solution gradually turned brown. The reaction continued for 2 hours at room temperature under stirring. The thiol group and carboxylic group of Tyr-Tyr-Cys strongly bind to the cobalt oxide surface to develop nanoparticles. During the nanoparticle formation, the interaction between Tyr-Tyr-Cys and the surface chirally distorts the local atomic conformation of the nanoparticle surfaces generating chirality.

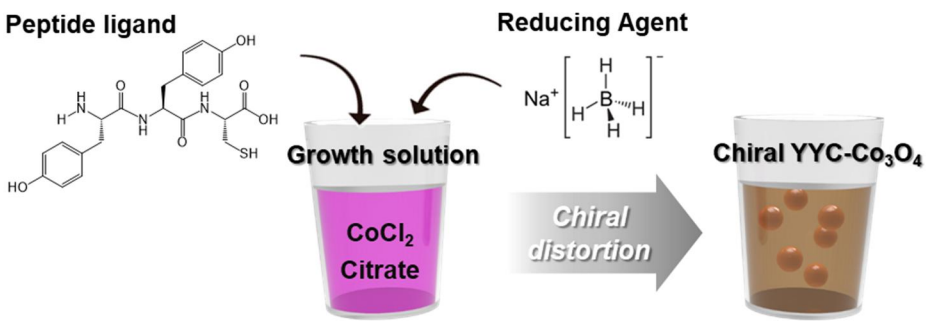

Figure 5.1 Schematic of solution based synthesis for developing chiral cobalt oxide nanoparticles using peptide ligand and reducing agent. Tyr-Tyr-Cys was injected into the growth solution as a chirality encoder.

Utilizing Tyr-Tyr-Cys ligand, chiral cobalt oxide nanoparticles with chiroptic properties were synthesized. Transmission electron microscopy (TEM) image in Figure 5.2 further confirmed that nanoparticle of about 5 nm in size were synthesized using a peptide ligand.[161] Circular dichroism (CD) and absorbance spectra of the chiral cobalt oxide nanoparticles were evaluated in the ultraviolet and visible region. Chiral cobalt oxide nanoparticles showed clear chiroptic responses with 5 positive and negative peaks as shown in Figure 5.3.[161] This distinct optical spectrum showed clear difference from previously reported chiral cobalt oxide synthesized using a single amino acid.[137] Nanoparticles synthesized using L-, and D-Tyr-Tyr-Cys ligands showed the perfect mirror-symmetric CD signal with coincident peak positions and zero crossing points. In detail, CD peaks at 260, 290 and 350 nm in the UV region and peaks at 550 and 640 nm in the visible region originated from LMCT with a small fraction of intraparticle Co(II)→Co(III) d-d transitions were observed.[137] When converted to Kuhn's dis-symmetry value, g-factor, chiral cobalt oxide nanoparticles showed maximum g-value of 0.01 at the wavelength of 640 nm (Figure 5.4).[161] L-, and D-YYC-directed nanoparticles showed almost the same absorbance spectra with the strong absorbance peak at 274 nm and a shoulder at 280 nm from the absorption of the tyrosine residue of Tyr-Tyr-Cys ligand with a small fraction of O(II)→Co(II) transition (Figure 5.5).[161–164] In addition, chiral cobalt oxide nanoparticles had characteristic peaks at 303 and 363 nm by ligand to cobalt charge transfer with small fraction of O(II)→Co(III) transition.[165–167]

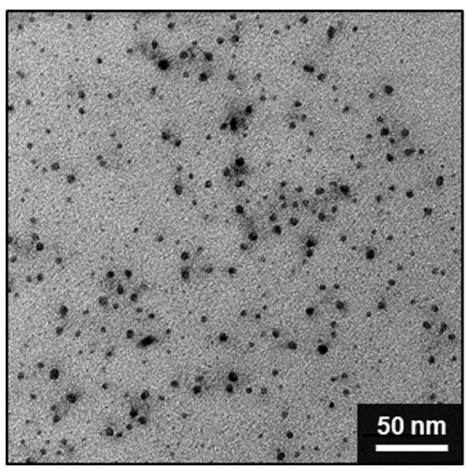

Figure 5.2 TEM image of synthesized chiral cobalt oxide nanoparticles. Scale bar is 50 nm.

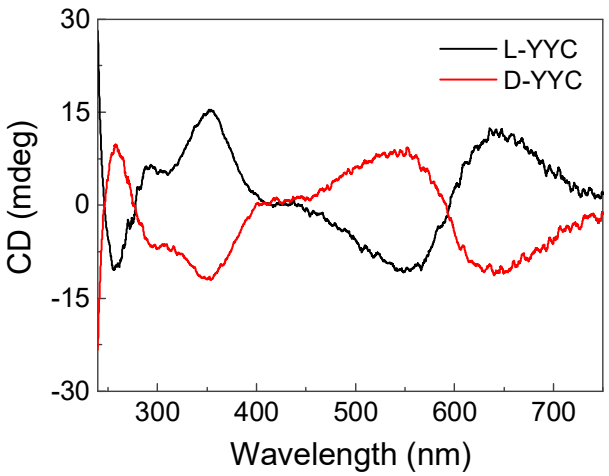

Figure 5.3 Circular dichroism spectra of L- (black line) and D-Tyr-Tyr-Cys-directed chiral nanoparticles (red line). The nanoparticles synthesized using Tyr-Tyr-Cys enantiomers showed mirror-symmetric CD responses.

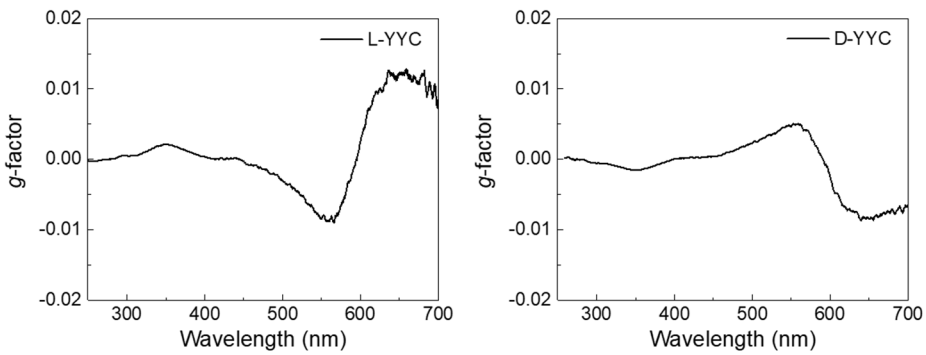

Figure 5.4 *g*-factor spectrum of the nanoparticles synthesized with L- (left) and D-Tyr-Tyr-Cys (right). The chiral cobalt oxide nanoparticles exhibited maximum g-value of 0.01 at the wavelength of 640 nm

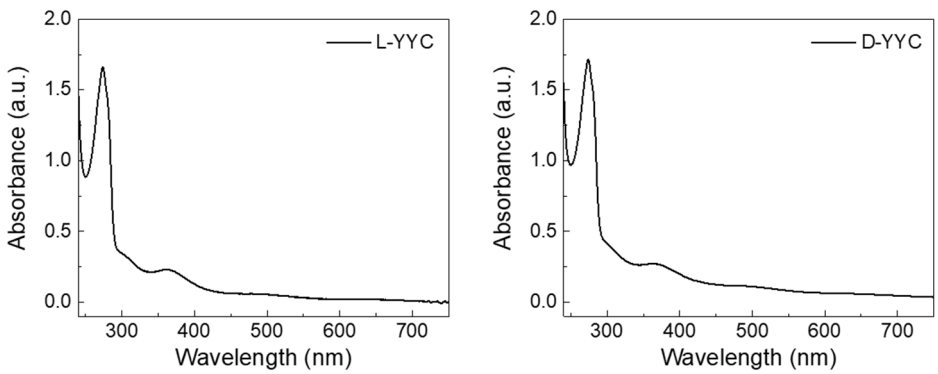

Figure 5.5 Absorbance spectrum of the nanoparticles synthesized with L- (left) and D-Tyr-Tyr-Cys (right).

5.3 Effect of Synthetic Parameters on Chirality Development of Chiral Cobalt Oxide Nanoparticles

To understand the underlying mechanism of the chiral nanoparticle formation and optimize the synthesis conditions, synthesis parameters were controlled during the growth. The molar concentrations of sodium citrate, Tyr-Tyr-Cys peptide ligand, and sodium borohydride were adjusted while the concentration of cobalt ion in the growth solution was fixed at 5 mM. First, Tyr-Tyr-Cys ligand which imparts chirality to the nanoparticles plays an important role in nanoparticle formation. In the absence of Tyr-Tyr-Cys, the solution appeared pinkish, indicating that no cobalt oxide nanoparticles were produced (Figure 5.6).[161] At 3.75 mM, the growth solution exhibited a light brown color, and above 5 mM, characteristic absorption peaks at 303 and 363 nm of cobalt oxide nanoparticles were observed, showing that the cobalt oxide nanoparticles were successfully synthesized. The color of the solution became light at higher concentrations, suggesting that the yield of nanoparticles decreased. The CD response in Figure 5.6 increased as the concentration increased, showing the highest value with distinct peaks at 5 mM Tyr-Tyr-Cys. At higher concentrations, the CD value decreased as the particle yield decreased. The highest g-factor of 0.011 was achieved at Tyr-Tyr-Cys concentration of 6.25 mM. At higher concentrations, the g-factor was saturated and the yield was reduced.

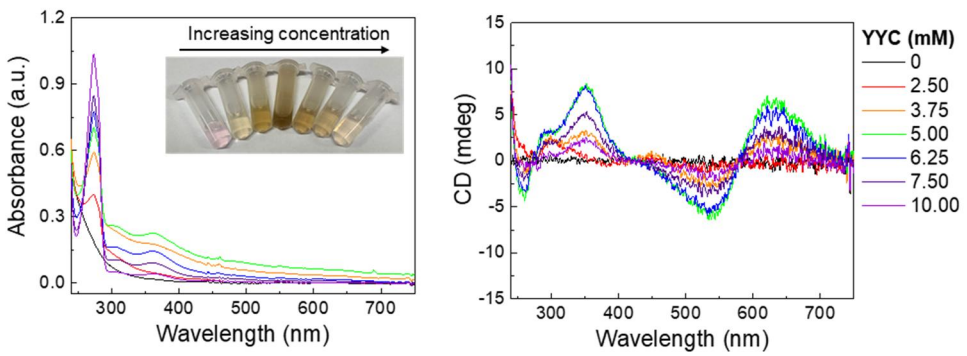

Figure 5.6 Effect of synthetic parameters on chirality development of chiral cobalt oxide nanoparticles. The molar concentrations of Tyr-Tyr-Cys were adjusted while the concentration of cobalt in the growth solution was fixed at 5 mM. Absorbance spectra (left) and CD spectra (right) of nanoparticles synthesized using Tyr-Tyr-Cys at various concentrations from 0 to 10 mM.

The concentration of sodium borohydride ($NaBH_4$), which used as a reducing agent during the synthesis, also greatly influences the yield and synthesis kinetics of the chiral cobalt oxide nanoparticles. At low concentrations of less than 3.75 mM, particles are hardly formed, resulting in a transparent solution with CD signal close to zero (Figure 5.7).[161] As the $NaBH_4$ concentration increased to 7.5 mM, the particle yield increased and the characteristic absorption peaks of cobalt oxide nanoparticles at 303, 363 nm appeared and increased. The CD signal in Figure 1d increased with increasing $NaBH_4$ concentration and produced the highest value at 7.5 mM. At 10 mM $NaBH_4$, the yield of the nanoparticles increased but the chirality of the particles decreased. Further increase in concentration largely changed the kinetic for particle formation. Particularly noteworthy, at high $NaBH_4$ concentration of above 20 mM, the characteristic absorption of cobalt oxide nanoparticle at 303, 363 nm disappeared and a divergent CD signal was generated, suggesting that nanoparticles with different properties were synthesized.

Citrate is not essential for the formation of nanoparticles, but it modulates the yield and g-factor of the nanoparticle by affecting the reduction of cobalt cation during the synthesis. As shown in Figure 5.8 the particle solution turned dark brown showing the characteristic absorption spectrum even at low citrate concentrations.[161] When citrate is in the growth solution, it affects the reduction of cobalt cation, reducing the yield of the nanoparticles. It is observed that as the concentration of citrate increased, the color of the solution changed from dark brown to light brown and the absorption peaks in UV-vis region were reduced. The overall shape of CD spectrum remained similar in the 0 to 10 mM citrate concentration range (Figure 5.8). The CD responses decreased slightly as the citrate concentration increased to 5 mM and slightly increased when the concentration further increased to 10 mM. The chirality index, g-factor, showed the highest value

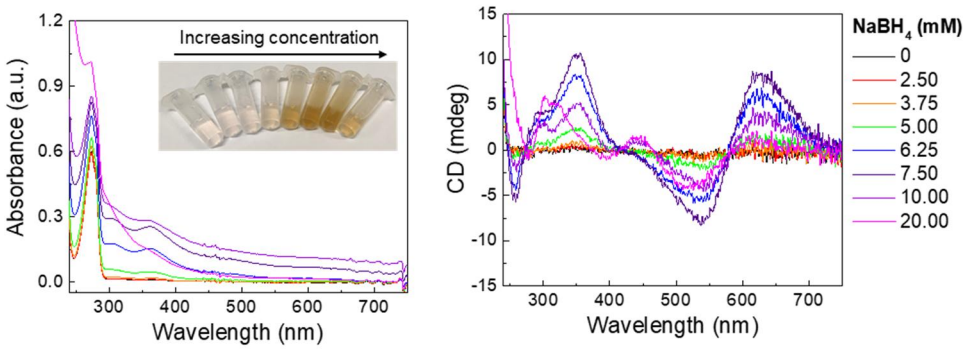

Figure 5.7 Effect of synthetic parameters on chirality development of chiral cobalt oxide nanoparticles. The molar concentrations of sodium borohydride were adjusted while the concentration of cobalt in the growth solution was fixed at 5 mM. Absorbance spectra (left) and CD spectra (right) of nanoparticles synthesized at various $NaBH_4$ concentrations from 0 to 20 mM.

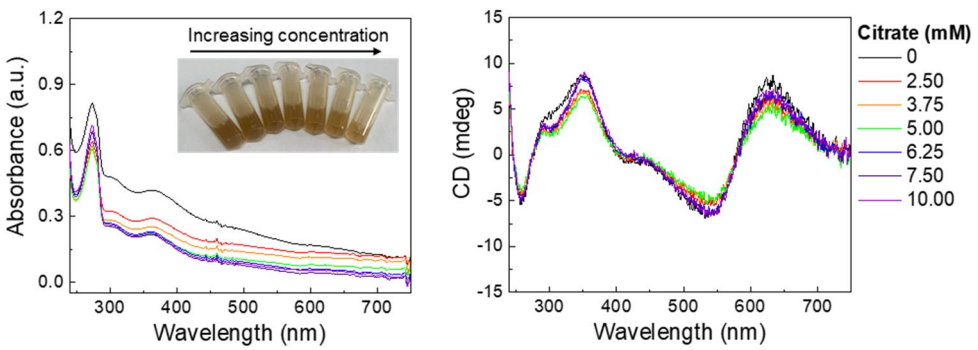

Figure 5.8 Effect of synthetic parameters on chirality development of chiral cobalt oxide nanoparticles. The molar concentrations of citrate were adjusted while the concentration of cobalt in the growth solution was fixed at 5 mM. Absorbance spectra (left) and CD spectra (right) of nanoparticles synthesized at various citrate concentrations from 0 to 10 mM. The images of the synthesized nanoparticle solutions were shown in the inset.

when the citrate concentration was 7.5 mM. Higher concentrations are expected to interfere with particle formation, decreasing the g-value. Taken together, in chiral cobalt oxide nanoparticle synthesis, Tyr-Tyr-Cys peptide and sodium borohydride initiate the synthesis and generate nanoparticles. Citrate affects the reduction of cobalt cations to control the particle yield and g-factor. The optimized synthesis condition for the highest chiroptic properties with g-factor of above 0.01 was found under 5 mM cobalt ion, 7.5 mM citrate, 6.25 mM Tyr-Tyr-Cys, and 6.25 mM $NaBH_4$.

5.4 3D Conformation of Tyr-Tyr-Cys Ligand

The tertiary interaction between Tyr-Tyr-Cys (or Y1-Y2-C3) peptides and cobalt oxide nanoparticles was investigated by NMR analysis. The intact peptides showed only one set of correlation peaks in Hα-NH, Hβ-NH, and NH-NH region of 2D TOCSY spectrum (Figure 5.9, magenta), suggesting that intact peptides have dynamic random structures.[161] However, after treatment with cobalt oxide nanoparticle, the NMR spectra of the peptides showed dramatic changes. First, a large number of new cross peaks were appeared. Also, among them at least 7 unambiguously distinguishable sets of Tyr-Tyr-Cys cross peaks were identified (Figure 5.9, other colors). Second, the proton resonances showed sizable pseudocontact shifts, which are well known as the changes in chemical shifts due to the close contact to paramagnetic center, in this case, Co^{2+}.[168] This observation clearly demonstrated that the peptides directly interacted with cobalt oxide nanoparticles, and as a result, the peptide structures were stabilized forming several different conformers.

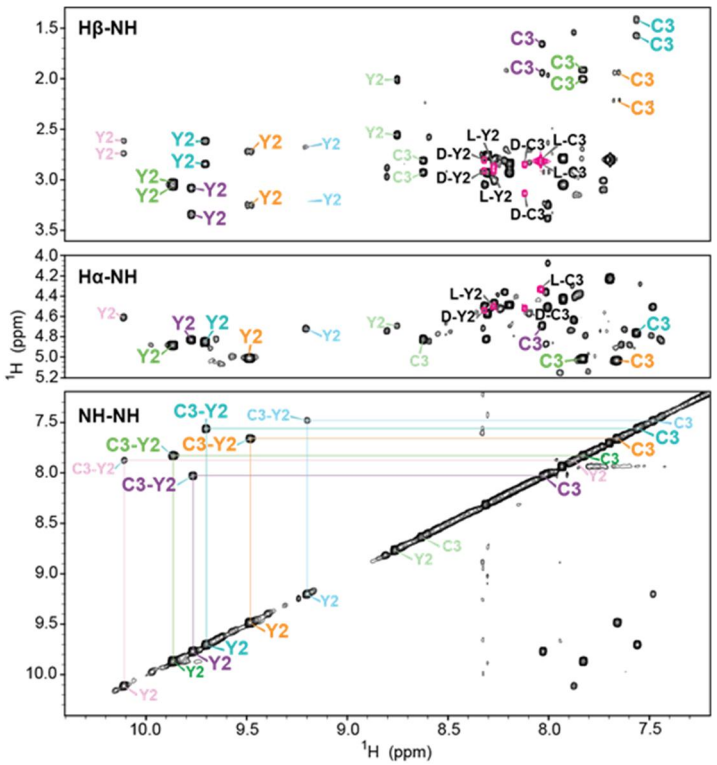

Figure 5.9 2D NOESY (NH-NH) and TOCSY (Hα-NH and Hβ-NH) spectrum.

Next, to examine the structural characteristics of Tyr-Tyr-Cys peptides and the binding interaction mode to cobalt oxide nanoparticle, we determined the solution structures of the peptides. Among the more than seven sets of identified Tyr-Tyr-Cys NOE peaks, the four sets that showed a distinct pseudocontact shift with clear NOE peaks were used for 3D structural calculations. The 20 lowest energy structures of all four conformers were well converged with a backbone r.m.s.d. of < 0.2 Å, respectively (Figure 5.10).[161] The Y1 of structure 4 was relatively less converged due to the lack of NOE restraints. To figure out how Tyr-Tyr-Cys interacts with cobalt oxide nanoparticle, the lowest energy structures of each conformation set were aligned through the alpha carbon atoms of each residue (Figure 5.11).[161] All amide nitrogen and carboxylic oxygen of the backbone as well as thiol of Cys faced toward the same direction. Since cobalt has great affinity to nitrogen, it is strongly suggested that the tertiary interaction of peptide with cobalt oxide nanoparticles is through the backbone interface including thiol of Cys. The side chains of Y1 and Y2 pointed toward the upper direction, but the directions of phenol ring of Y1 are different. The angle of the aromatic ring of Tyr1 between set 3 and set 4 was measured to be ~ 90 degrees (Figure 5.11), therefore we suggest that the slightly different peptide structures might play a role as a building block of cobalt oxide nanoparticles.

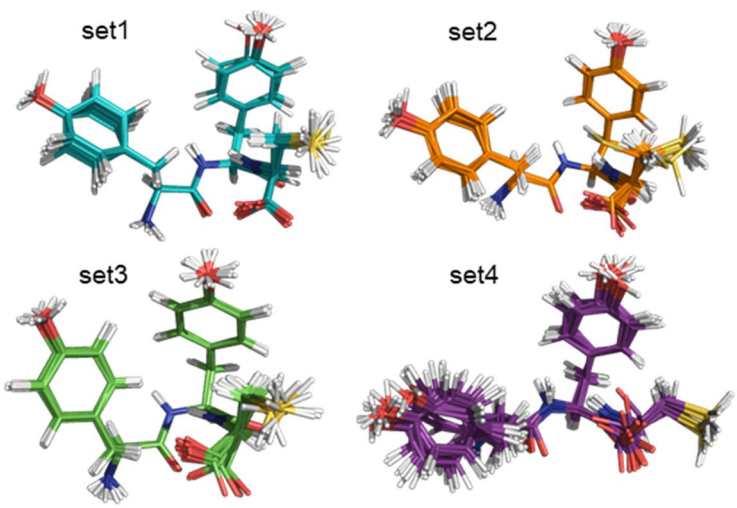

Figure 5.10 Superimposition of the 20 lowest energy conformations of the four representative conformation sets. The colors of the elements C, N, O, H, and S in the structures are green, blue, red, white, and yellow, respectively.

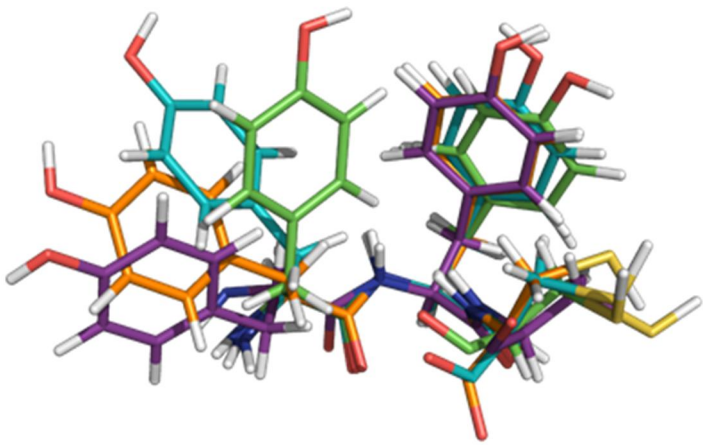

Figure 5.11 Superimposition of the lowest energy conformations of each conformation set, which are aligned for the α carbon of backbone.

5.5 Sequence Effect of the Tyr-Tyr-Cys

Based on our understanding on the configuration of Tyr-Tyr-Cys decorating nanoparticle, the sequence effect was explored to investigate the role of Tyr-Tyr-Cys in developing nanoparticles. First, in order to explore the role of the N-terminal and C-terminal of Tyr-Tyr-Cys in developing chiral nanoparticles, L-Tyr-Tyr-Cys ethyl ester with a blocked carboxylic acid group and *N*-acetyl-L-Tyr-Tyr-Cys with a blocked amine group were used for synthesis. Along with the NMR data presented above, the terminal blocking experiment suggests that the thiol group and the carboxylic group of Tyr-Tyr-Cys play an important role in the chiral nanoparticle evolution. As shown in Figure 5.12, blocking the C-terminal of the peptide prevented the formation of the chiral cobalt oxide nanoparticles, resulting in the disappearance of the CD response.[161] The absorbance spectrum of the C-terminal-blocked case showed that the characteristic LMCT peak disappeared due to low nanoparticle yield with a large scattering in visible-IR range by peptide aggregates (Figure 5.12). When the N-terminal of the peptide was blocked, a CD response similar to Tyr-Tyr-Cys-directed nanoparticle was obtained, while chirality was not observed when the C-terminal was blocked. N-blocked Tyr-Tyr-Cys-directed nanoparticles showed a similar absorbance spectrum to Tyr-Tyr-Cys-directed nanoparticles matching the characteristic peaks at 274, 303, and 363 nm. Detailed observations revealed that the CD peaks in the UV region of the N-blocking coincided with Tyr-Tyr-Cys-directed nanoparticles, but the CD peaks in the visible region were blue-shifted. This result indicates that the N-terminal amine group of Tyr-Tyr-Cys is not dominant in developing chiral nanoparticles, but appears to participate in chirality evolution altering the CD spectrum.

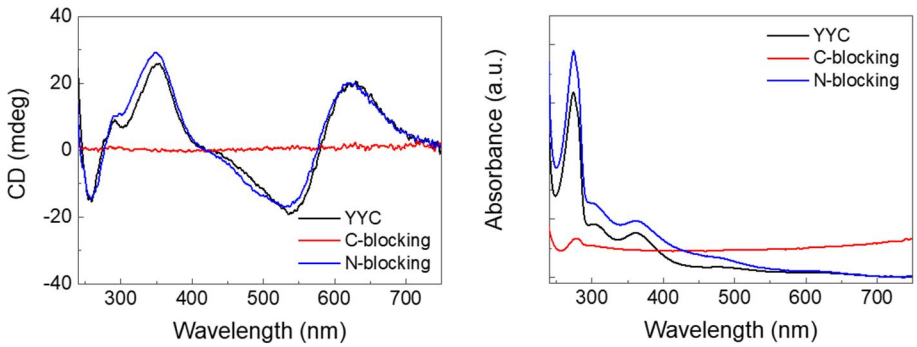

Figure 5.12 CD spectra (left) and absorbance spectra (right) of the nanoparticles synthesized with Tyr-Tyr-Cys (black line), C-terminal (red line), and N-blocked Tyr-Tyr-Cys (blue line). For the C- and N-blocking experiment, L-Tyr-Tyr-Cys ethyl ester and *N*-acetyl-L-Tyr-Tyr-Cys were used, respectively.

To provide an in-depth understanding on the role of Tyr-Tyr-Cys peptide in chiral nanoparticle development, Cys-Tyr-Tyr and cysteine ligands were used for the synthesis and compared to Tyr-Tyr-Cys. Tyr-Tyr-Cys-directed cobalt oxide exhibited a characteristic CD spectrum in UV and visible range. However, when Cys-Tyr-Tyr and cysteine were involved as a chirality inducer, CD responses different from Tyr-Tyr-Cys was obtained. When Cys-Tyr-Tyr was added instead Tyr-Tyr-Cys, a CD spectrum with similar peak positions at 260, 290, 350 nm but different shape was obtained in the UV region (Figure 5.13).[161] Also, it exhibited a unique spectrum with a positive CD peak at 480 nm and a negative peak at 560 nm in the visible region. In case of cysteine, a continuous spectrum of negative peaks near 290 nm, positive peaks at 350 nm, positive peaks near 500 nm, and negative peaks near 550 nm was observed, which is considered to be similar to Cys-Tyr-Tyr case. In addition, nanoparticles synthesized using Cys-Tyr-Tyr and cysteine had unique absorption spectra different from Tyr-Tyr-Cys (Figure 5.13, right). When Cys-Tyr-Tyr was used, a unique absorbance spectrum appeared with peak at 274 nm with 280 nm shoulder corresponding to the absorption of tyrosine residues and peak at 340 nm originated from LMCT.[162,166,167] For cysteine-directed nanoparticles, absorption peaks at 260 nm corresponding to the absorption of cysteine and peak at 340 nm derived from LMCT were observed.[169] The thiol group and amine group and carboxyl group of the peptide interact with the inorganic surfaces. Therefore, it is expected that the configuration of the ligand on the interface will be different, depending on the spatial location of functional groups. We suppose that in the case of cysteine and Cys-Tyr-Tyr, where both amine groups are exposed, thiol groups and amine groups bind to NP surface, by order of binding affinity, resulting in different chiroptic properties from Tyr-Tyr-Cys.

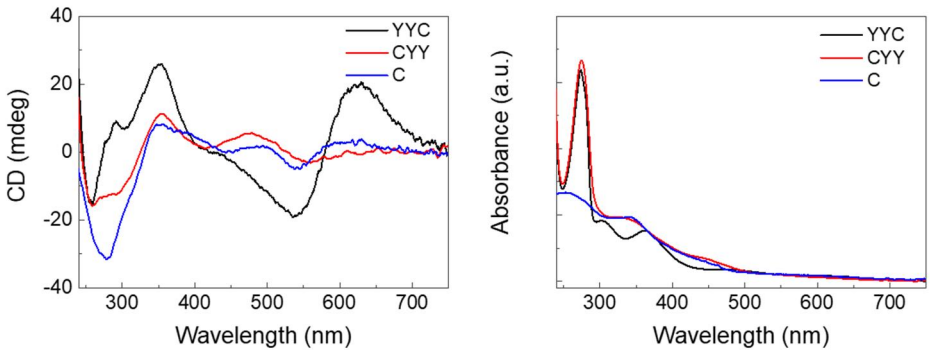

Figure 5.13 The sequence effect of Tyr-Tyr-Cys ligand in chiral cobalt oxide nanoparticles development. CD spectra (left) and absorbance spectra (right) of nanoparticles synthesize with Tyr-Tyr-Cys (black line), Cys-Tyr-Tyr (CYY, red line), and cysteine (C, blue line).

5.6 Magnetic Circular Dichroism in Chiral Cobalt Oxide Nanoparticles.

The chiroptic response of the synthesized cobalt oxide nanoparticle which is paramagnetic at room temperature can be modulated by an external magnetic field. For the first time in chiral cobalt oxide nanoparticles, CD and magnetic circular dichroism (MCD) were analyzed according to the presence and direction of a magnetic field and compared with achiral cobalt oxide nanoparticles. CD spectra of chiral cobalt oxide nanoparticles synthesized with Tyr-Tyr-Cys were measured in the presence of magnetic field of 1.6 T in parallel (forward) and antiparallel (backward) directions of light propagation. In order to evaluate a pure magnetic contribution on circular dichroism, MCD spectra except natural CD obtained without external magnetic field to total CD was depicted in Figure 5.14 and 5.15.[161] The MCD of the chiral cobalt oxide nanoparticles showed a strong negative peak at a position of the absorption maximum of 274 nm. It also exhibited a relatively small positive peak at 390 nm and a negative peak at 508 nm, which are expected to be originated from ligand to cobalt transfer and d-d transition of Co(II) and Co(III), respectively.[170,171] When the direction of the magnetic field was reversed, the sign of these three peaks were reversed showing a symmetrical spectrum.

The strong MCD signal in the UV region of the peptide-directed nanoparticles was achieved by utilizing the absorption of tyrosine residues through peptide-inorganic hybridization. To further analyze, achiral cobalt oxide nanoparticles were synthesized through a hydrothermal method, and the MCD spectra were measured and compared with chiral cobalt oxide nanoparticles (Figure 5.16).[161] Achiral nanoparticles showed broad absorbance peaks from UV

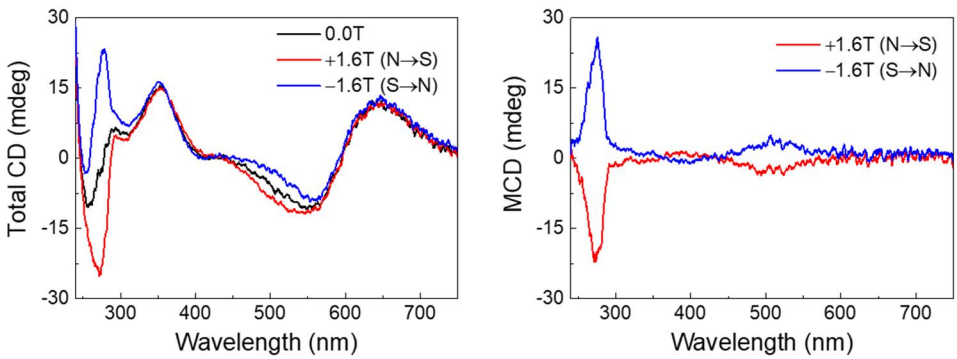

Figure 5.14 Magnetic circular dichroism in chiral cobalt oxide nanoparticles. Total CD spectra (left) and MCD spectra (right) of L-Tyr-Tyr-Cys-directed chiral cobalt oxide nanoparticles. The MCD measurement was conducted under an external magnetic field of 1.6 T in the forward (red line) and backward directions (blue line) of the light propagation. The MCD spectrum was obtained through subtracting the natural CD from the total CD spectrum.

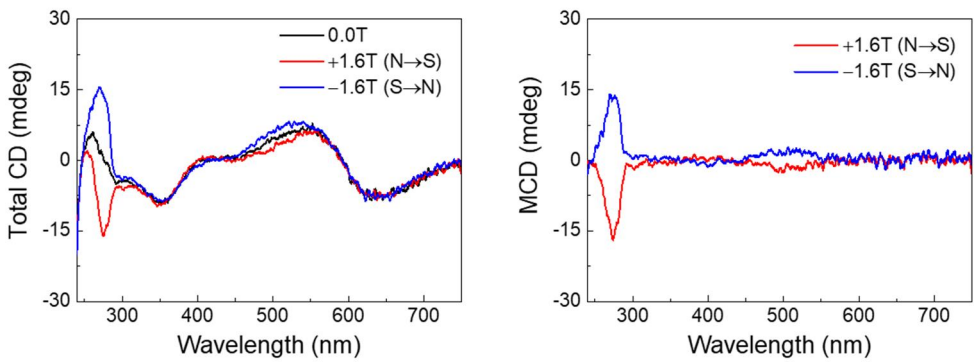

Figure 5.15 Magnetic circular dichroism in chiral cobalt oxide nanoparticles. Total CD spectra (left) and MCD spectra (right) of D-Tyr-Tyr-Cys-directed chiral cobalt oxide nanoparticles. The MCD measurement was conducted under an external magnetic field of 1.6 T in the forward (red line) and backward directions (blue line) of the light propagation. The MCD spectrum was obtained through subtracting the natural CD from the total CD spectrum.

to 300 nm corresponding to O(II)→Co(II) transition, and at 340 to 600 nm and around 700 nm which were originated from O(II)→Co(III) transition (Figure 5.16, left). [161,172,173] The achiral nanoparticles did not exhibit a natural CD response in the absence of a magnetic field. When an external magnetic field was applied, it showed broad MCD peaks which were symmetric according to the magnetic field direction due to the intrinsic magnetic properties of cobalt oxide (Figure 5.16, right). Due to the absence of strong absorption of tyrosine residue in the UV region, the magnitude of the MCD signal was about 10 times smaller than that of chiral cobalt oxide nanoparticles, demonstrating that the MCD signal can be improved via peptide-inorganic hybridization. Chiral cobalt oxide nanoparticles synthesized using Tyr-Tyr-Cys are optical materials that combine chirality and magnetism and showed the versatile potential of chiral nanomaterials for application in industry by controlling the optical activity that was considered permanent after fabrication or synthesis.

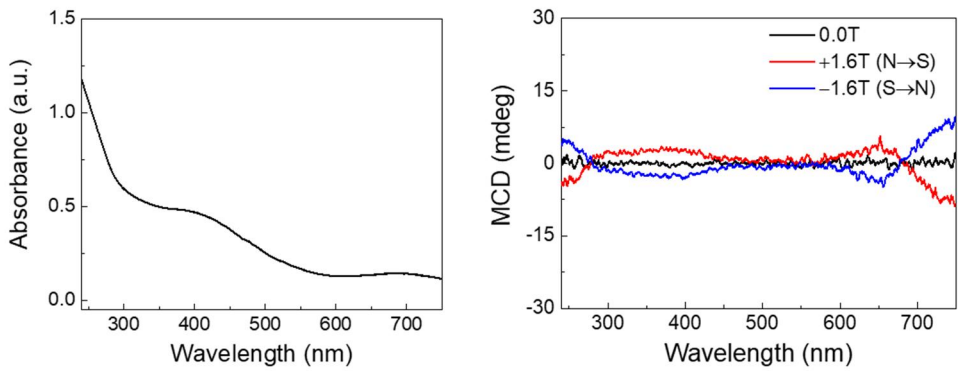

Figure 5.16 Absorbance (left) and MCD spectra (right) of achiral cobalt oxide nanoparticles synthesized by a hydrothermal method. The MCD measurement was conducted under an external magnetic field of 1.6 T in the forward (red line) and backward directions (blue line) of the light propagation.

5.7 Conclusion

In summary, chiral cobalt oxide nanoparticle with g-factor of 0.01 in visible range was synthesized using Tyr-Tyr-Cys ligand. Since chiral nanoparticles were evolved through the interaction between the peptide and the inorganic surfaces, synthesized nanoparticle exhibited mirror-symmetric chiroptic responses depending on the handedness of the peptides. The role of the chemical parameters that can determine the chirality evolution in the nanoparticles was elucidated and the synthetic condition was optimized for a large chiroptic response through experimental demonstration. In the synthesis of chiral cobalt oxide nanoparticles, peptide imparted chirality to nanoparticles and initiated the particle formation. Sodium borohydride affected the kinetics of particle formation and final yield of the nanoparticle, and citrate adjusted the particle yield and g-factor. In addition, the 2D NMR analysis revealed that the thiol group and carboxylic group of the Tyr-Tyr-Cys ligand were aligned in single direction on the nanoparticle, indicating their strong interaction with the nanoparticle surfaces. Furthermore, the sequence effect of Tyr-Tyr-Cys developing chiral nanoparticle was analyzed. The C-terminal carboxylic group of the peptide exhibited a dominant effect on the chirality expression of the nanoparticle. The use of Cys-Tyr-Tyr and cysteine instead of Tyr-Tyr-Cys generated different chiroptic responses, which are expected to be the effect of exposed amine groups. Given the diversity of peptides, this suggests the infinite expandability of the synthesis method utilizing peptide ligand. Due to the magnetic properties of chiral cobalt oxide nanoparticle, the chiroptic properties could be modulated by an external magnetic field. The MCD measurement demonstrated that the CD response in the UV and visible region of the nanoparticles dramatically changed under a magnetic field of 1.6 T. The Tyr-Tyr-Cys-directed chiral cobalt oxide nanoparticle exhibiting chiroptic properties that can be controlled by an

external magnetic field is not only important for the fundamental studies on spintronics and magneto-optics, but also can be widely applied as opto-electronic devices, active displays and chiral catalysts.

Chapter 6. Circular Dichroism Manipulation based on Plasmonic Coupling of Chiral Nanostructures

6.1 Introduction

Chiral metamaterials, benefited from recent advances in nanophotonics, have been actively pursued for its exceptional light-manipulating capabilities such as, control over polarization state of light,[174,175] and bio-sensing.[143,176] As chirality is a true 3D nature, numerous efforts has been conducted to fabricate 3D chiral metamaterials using lithographic approaches and synthetic approaches at the subwavelength scale. Inspired by biological systems that evolve highly complex 3D chiral shape from molecular to macroscopic scale,[1,3] chiral metamaterials with continuous 3D morphology were chemically synthesized using organic molecules and exhibited strong chiroptical response.[128,177–181] However, the difficulty in modulation of the chiral response for desired purpose, along with a lacked flexibility in manipulating of the chiral structure at nanoscale, had restricted the translation of chiral metamaterials into practical devices.

Modulation of chirality and chiroptical response can be achieved through minute change in morphology in nanoscale. In this regard, many attempts have been made to control over chiroptical properties by changing size,[87] arrangement,[38] and structure of nano-building blocks.[181] In chemical synthesis, incorporation of different additive during the synthesis can generate divergent chiral nanostructures. Recently, evolution of chiral gold nanoparticle using wide ranges of multi-scale biological encoder was demonstrated using from amino acid to oligonucleotide.[87,129,152] Alterations of chiral additives involved in the synthesis affect the evolutionary

pathway of nanoparticle, resulting in completely different morphologies and chiroptic responses. In another approach, the optical response of a single plasmonic particle can be amplified and sensitively modulated using plasmonic coupling. When several nanoscale plasmonic particles are adjacent to each other, hybridization of particle resonance is induced, which significantly changes the resonance wavelength.[182] In plasmonic coupling, not only the distance but also the shape of the nanogap affects the optical signal, and through arraying and coupling with a metal film, a plasmon coupling mode that is not observed in single particles can be created.[183,184]

In Chapter 6, we demonstrate the fabrication of a helicoid-based metamaterials. We analyzed its chiral scattering properties through DRCD measurement along with conventional transmission-based CD spectroscopy. We demonstrated that it is possible to improve and modulate the CD response with simple gold nanolayer deposition in the helicoid-based metamaterial. Interestingly, in metal-layer incorporated helicoid film, the DRCD peak is inverted by creating a new mode in the visible region, exhibiting the same sign in transmitted CD peak and DRCD peak. In addition, we showed that the spectral shape of DRCD of helicoid-based metamaterial can be finely modulated by adjusting structural parameter such as the development of chiral gap of helicoid, the thickness of gold layer. Furthermore, synthesis of chiral gold-silica core-shell NPs was demonstrated, enabling versatile control of the structure and properties of plasmonic nanoparticles.

6.2 Chiroptical Property of Helicoid-Based Plasmonic Nanostructure

We designed an optical metamaterials utilizing 432 helicoid III, hereinafter called helicoid, synthesized from solution-based method using peptide. The helicoids exhibit a cube-like shape, in each face of the cube is implemented with four chiral arms evolving away from the center, breaking mirror and inversion symmetry for the 432 point group symmetry generation.[87] To fabricate helicoid NP film, the helicoids are coated onto quartz substrate by electrostatic coating method using charged particles and plasma-treated substrate. During the coating, CTAB molecules separate the NP spatially with little aggregation. The helicoid NP film was coated with gold layer of 10 to 50 nm by E-beam evaporation. Growth of gold layer on helicoid NP film creates a conformal hat structure that follows a pinwheel-like chiral motif on the helicoid, and nanogap structure at the bottom of the helicoid as shown in Figure 6.1.

In order to investigate the chiroptical properties of fabricated helicoid-based metamaterial, we utilized conventional transmission-based circular dichroism (CD) spectroscopy and diffuse reflectance circular dichroism (DRCD) spectroscopy that collect light scattered off a surface in different directions. Due to the high symmetry of helicoid unit, the helicoid films show a strong ensemble chiroptic response despite of the random deposition of NPs onto the film (Figure 6.2 and 6.3). Interestingly, our helicoid-based plasmonic metamaterial has the same sign in transmitted CD mode and diffuse-reflected CD mode in the visible region (Figure 6.3). Bare helicoid film exhibited three distinct peaks in the spectral range from visible to near-IR in transmitted CD spectrum. The strongest CD mode in 600nm

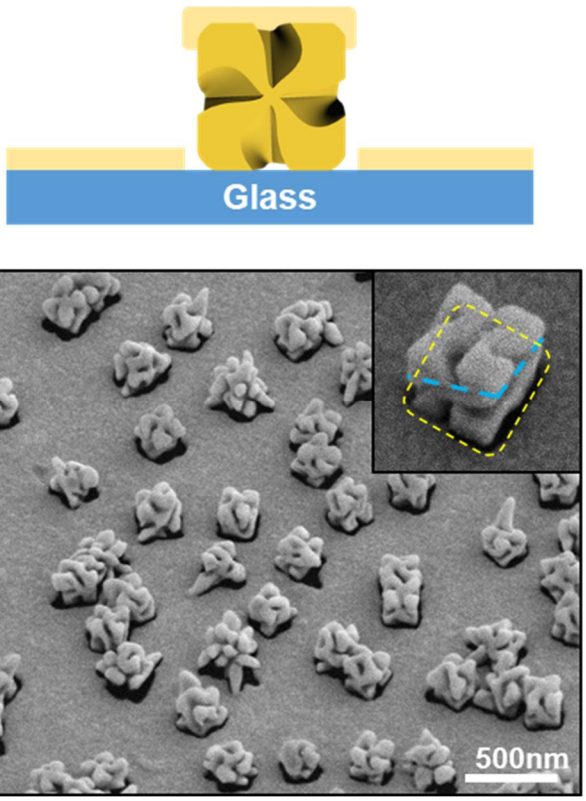

Figure 6.1 Schematic illustration (top) and SEM images (bottom) of helicoid-based plasmonic metamaterial. Gold layer was deposited onto helicoid NPs film to create a hat structure on the helicoid and nanogap structure at the bottom. The hat and nanogap structures are shown in the inset.

appeared to be flipped when DRCD was observed (Figure 6.2). Another CD mode in NIR region also showed the opposite sign when measured in the forward and backward directions, whereas A CD peak around 400 nm maintained the same sign. The intensity of the main peak for transmitted CD was higher than DRCD, and the peak positions was red-shifted about 10nm when observed by DRCD.

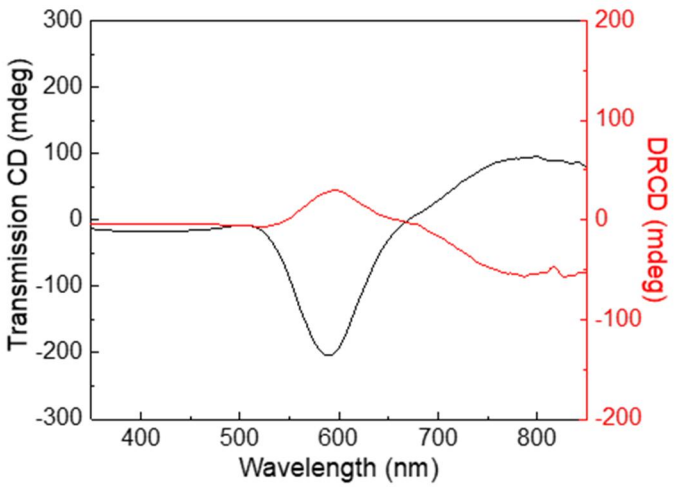

Figure 6.2 Transmittance CD spectrum (black line) and DRCD spectrum (red line) of bare helicoid film. Transmittance CD showed negative main peak, whereas DRCD exhibited positive main peak at around 600 nm.

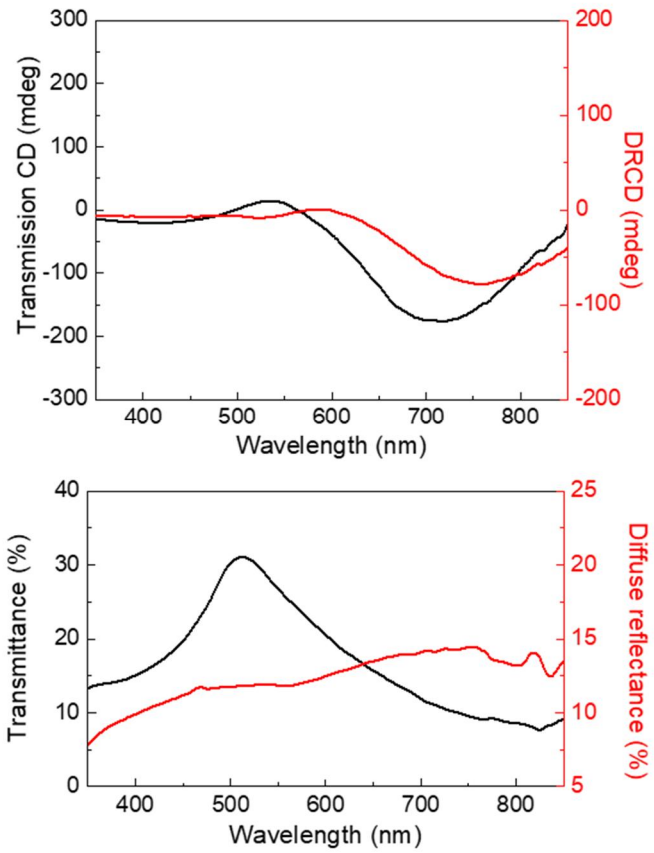

Figure 6.3 Transmittance CD spectrum (black line) and DRCD spectrum (red line) of helicoid-based metamaterial deposited with a 30 nm gold layer (top). Transmittance (black line) and diffuse reflectance (red line) of helicoid-based metamaterial (bottom).

The addition of gold layer improved the diffuse reflectance of the 30nm gold layer deposited helicoid film to 13%, with reduced transmittance of 15% at the wavelength of 600 nm (Figure 6.3). After the gold layer coating, the main peak positions have red-shifted about 40nm, and DRCD peak is observed in a longer wavelength than Trans CD, like the bare helicoid film. This peak shift can also be confirmed by red-shift in the dip in transmittance spectrum and peak in diffuse reflectance spectrum. Interestingly, the main peak sign in DRCD spectrum is shown to be flipped in metal-layer deposition helicoid film, exhibiting the same negative sign of the transmitted CD mode, which is a phenomenon that has been reported several times in optical metamaterials operating NIR but was not observed in the visible region. In addition, the intensity of both CD signal enhanced with the incorporation of gold layer. Especially, the increase rate of DRCD response was found to be 3 after deposition.

In order to understand the modulation in CD spectrum through plasmon coupling, mode shift effect was analyzed by observing the absorption spectra in the VIS-NIR region of the bare helicoid film and gold layer coated film. In bare helicoid film, an absorbance peak was observed at 550 nm (Figure 6.4). When the gold layer was deposited, the absorption mode was observed to be redshifted by plasmon coupling, as shown in Figure 6.4. Since the CD signal is generated by the excitation difference between LCP and RCP in each mode, it can be understood that CD modulation occurs due to the shift phenomenon of the plasmon coupled mode.

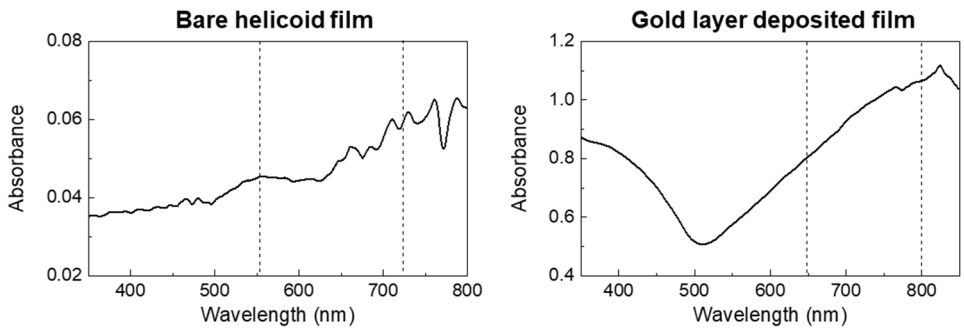

Figure 6.4 Absorbance spectra of bare helicoid film (left) and gold layer deposited film (right).

6.3 Effect of Chiral Gap Structure

To better understand the role of curved arms of helicoid NP in chiroptic response of helicoid-based metamaterials, we observed the change in transmission CD and DRCD spectra of the films as the plasmonic gap of helicoid gradually developed. As gsh molecule drives asymmetric growth of nanoparticles, the morphology evolution of the chiral gaps of helicoid can be controlled by the concentration of gsh. Indeed, nanoparticles with more curved and deeper plasmonic gaps were synthesized as the gsh concentration increased from 3.3 to 5 μM (Figure 6.5). To fabricated helicoid-based metamaterials, the synthesized nanoparticles with different shapes were coated onto quartz substrates and deposited with 30 nm of gold layer by E-beam evaporation. As the gsh concentration involved in the synthesis increased, the main peak intensity of transmission CD signals of helicoid-based metamaterials gradually increased with redshifted chiral response and transmittance dip (Figure 6.6). The deeper and more twisted gaps of helicoid from high gsh concentration are expected to enhance the chirality of the hat structure on top of helicoid. In metamaterials based on a more distinct chiral motif, the intensity of flipped DRCD signal from plasmonic coupling with deposited gold layer structure as well as transmission CD is gradually intensified. In DRCD, the sign of the main peak was flipped due to the plasmonic coupling, and the intensity of the flipped DRCD signal also showed gradual increase and redshift when the chirality of helicoid increased (Figure 6.7).

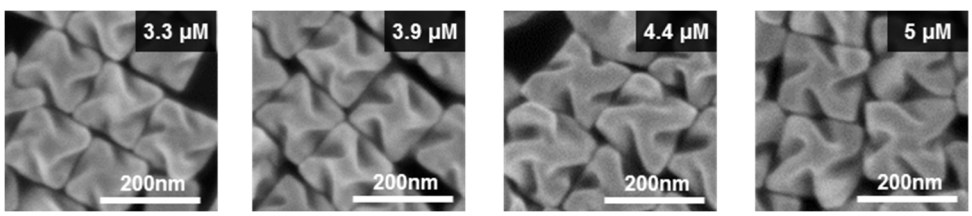

Figure 6.5 SEM images of different gap morphologies of helicoid NPs synthesized by the addition of 3.3 µM, 3.9 µM, 4.4 µM, and 5.5 µM L-gsh. As L-gsh concentration increased, nanoparticles with more curved with deeper plasmonic gaps were synthesized. The scale bars are 200 nm.

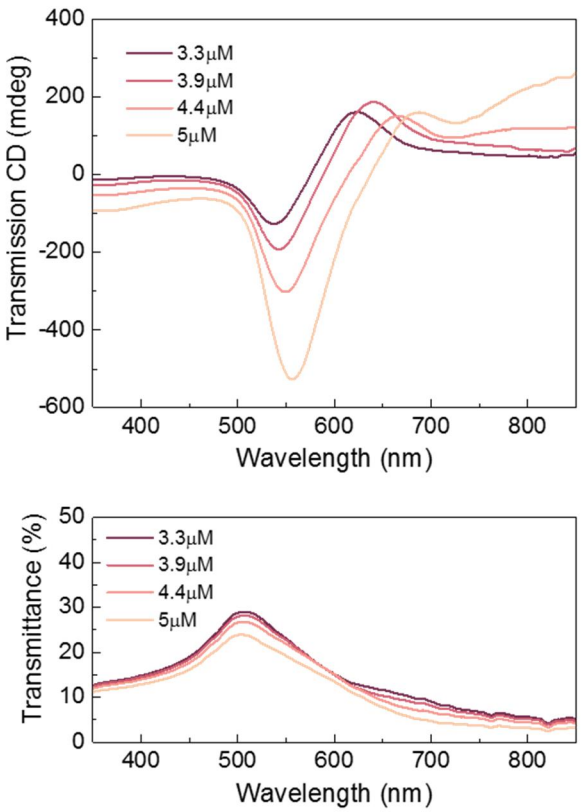

Figure 6.6 Transmittance CD spectra (top) and transmittance (bottom) of helicoid-based metamaterials with different chiral gap structure.

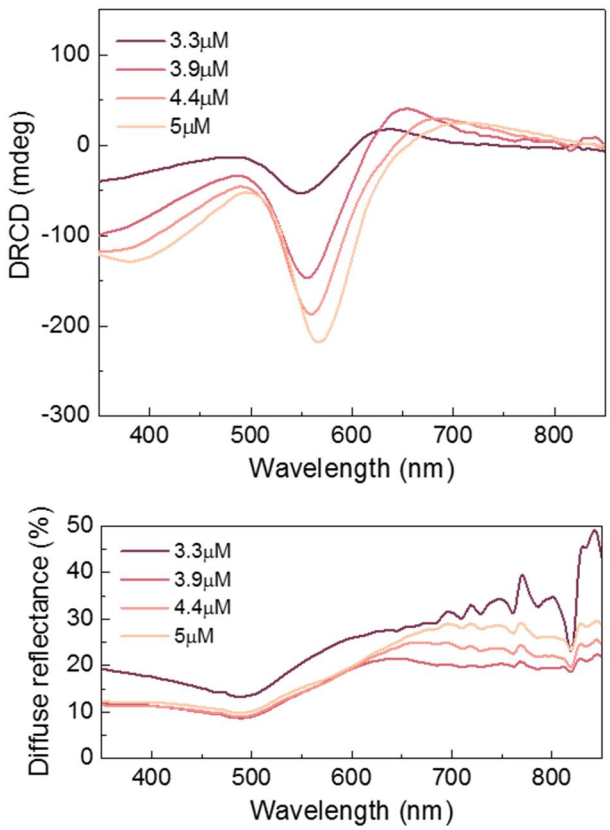

Figure 6.7 DRCD spectra (top) and diffuse reflectance (bottom) of helicoid-based metamaterials. The main CD peaks at 600 nm gradually increased with increasing gsh concentration.

6.4 Spectral Manipulation through Structural Parameter Control

In order to better elucidate the correlation between the nanostructure of helicoid-based metamaterials and the corresponding chiroptic response, we measured the Transmission CD and DRCD with varying gold layer thickness as shown in Figure 6.8. Evidently, spectral shape of helicoid-based metamaterials is closely dependent on the hat structure which is crucial to generate plasmonic coupling mode. For the measurement, 10 to 50 nm of gold layers were deposited onto helicoid film and compared to bare helicoid film without gold layer. Thicker gold layer increases the height of the hat structure of helicoid-based metamaterials. The thicker the gold layer, the greater the absorption and reflection of the gold layer, which reduces light transmittance and increases diffuse reflectance. When observed through DRCD, bare helicoid film showed a positive main peak at 600 nm, and negative peaks at around 400 nm and NIR region. When a hat and gap structure are gradually created by increasing gold layer thickness, CD peaks at around 400nm and NIR red-shifted as the gold layer becomes thicker without flip, whereas the main peak at 600nm changed and inverted gradually. In detail, addition of 10 nm of gold layer changed the spectral shape of helicoid film due to the excitation of coupled mode. In the case of 20 nm, generation of negative peak at 600nm is clearly shown. The intensity of the flipped CD peak reached maximum value at 40 nm gold layer case.

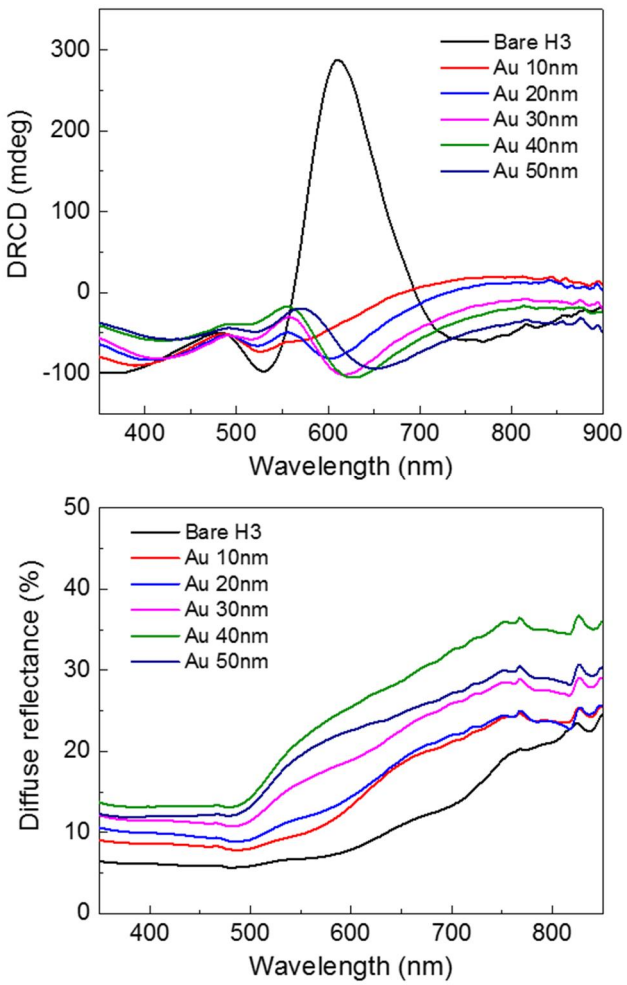

Figure 6.8 DRCD spectra (top) and diffuse reflectance spectra (bottom) of helicoid-based metamaterials with different gold layer thickness from 0 to 50 nm.

6.5 Synthesis of Chiral Gold-Silica Core-Shell Nanoparticles

Through the previous research results, it was found that the coupled plasmon mode changes significantly depending on the dimension, distance, and refractive index of the nanostructure. From this point of view, the facile control of the nanostructure and optical properties of plasmonic nanoparticle is important for practical applications in various fields. The properties of chiral gold nanoparticles can be improved through silica coating, which has excellent refractive index and stability. In order to synthesize chiral gold-silica core-shell nanoparticles, we utilized the stöber method, a chemical process for synthesizing silica in a water-ethanol mixed solvent (Figure 6.9). First, in order to disperse the helicoid nanoparticles in organic solvent, the CTAB ligands has exchanged to mPEG-SH. Then, a silica coupling agent was injected into the chiral nanoparticle solution to synthesize silica shell. A high pH environment promotes the condensation reaction and generates a uniform shell.

Through the introduction of silica shell, it is possible to adjust and improve the optical response of gold nanoparticles. *g*-factor spectrum of the chiral nanoparticle films coated with 0 to 20nm silica shell were measured as shown in Figure 6.10. In detail, *g*-factor spectrum was redshifted due to the increase of the peripheral refractive index as the silica shell became thicker. In addition, it was shown that the *g*-factor gradually increased as the silica shell became thicker.

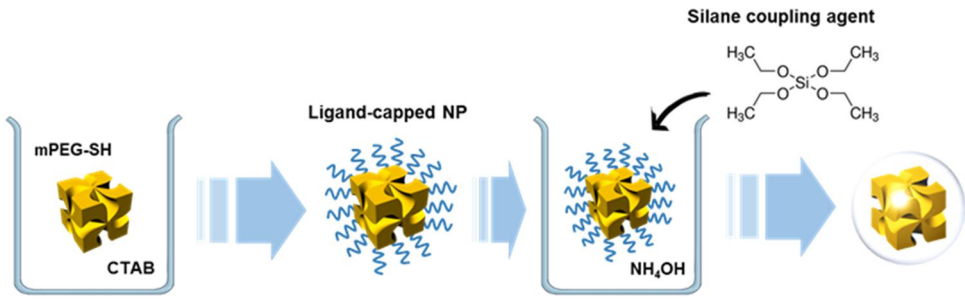

Figure 6.9 Schematic of synthesis of chiral gold-silica core-shell nanoparticle utilizing a modified stöber method.

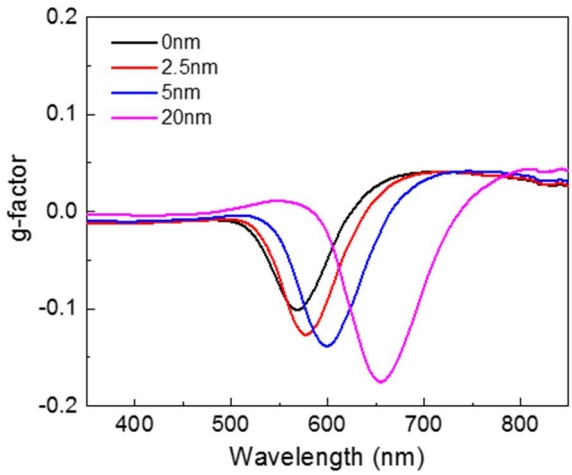

Figure 6.10 g-factor spectrum of chiral gold-silica core-shell nanoparticle films with different silica shell thickness.

6.6 Conclusion

In Chapter 6, circular dichroism manipulation was achieved by combining helicoid particles with a gold layer and synthesizing core-shell nanoparticles. We have fabricated optical metamaterial utilizing helicoid nanoparticle with strong intrinsic chirality, and analyzed its chiral scattering by DRCD measurement along with conventional transmission CD measurement. The highly sophisticated feature of helicoid nanoparticle and plasmonic property, and its well-defined electromagnetic coupling with conformally coated metal nanostructure modulate back-scattered light in the visible region to preserve the same handedness as the transmission. In addition, the spectral shape of DRCD can be finely controlled and even designed by structural parameters such as the development of chiral arms and the height of chiral hat structure. In addition, through the synthesis of chiral gold-silica core-shell nanoparticles, the chiroptic response of gold nanoparticles was enhanced and modulated. We believe the manipulation of optical response of plasmonic nanostructure can ultimately facilitate the application of chiral metamaterials into real devices.

Chapter 7. Concluding Remarks

In this thesis, we demonstrated modulation of a chiroptic response using plasmon coupling. The fundamental motivation of this research was inspired by biological pathway for nanoscale morphology and chirality control. Based on understanding underlying mechanism and influential factors for chiroptic properties of nanomaterials, we diversified nanoparticle morphology using peptide molecules and modulated its optical response utilizing plasmonic coupling of nanostructures. First, we focused on the role of peptide ligand and its functional group in developing chirality in nanoparticles. Second, we presented the circular dichroism modulation through plasmon coupling which has been studied to control optical properties in achiral nanostructure.

Fascinating physical phenomena of inorganic plasmonic nanomaterials have led to numerous attempts to fabricate chiral nanostructures using state-of-the-art lithographic techniques and molecular assembly scaffolds. Among them, the implementation of a chiral structure through interacts with an inorganic interface and a biomolecule gives an inspiration for the development of a chiral nanostructure. Since biomolecules with intrinsic chirality can be self-assembled in chiral geometries, chiral plasmonic building blocks can be assembled into chiral microscopic assemblies to fabricate chiral nanostructures such as spirals, twisted rods and asymmetric pyramids. In this thesis, we reported the fabrication of chiral nanostructures through chirality transfer from organic to inorganic at the interface of high Miller-index planes of inorganic crystals and biomolecules. Understanding of interactions and optical response at the nanoscale is a cornerstone for modulation of CD responses to improve the applicability of chiral metamaterials.

Firstly, chiral morphology and resulting optical response were manipulated by changing ligands molecules involved in synthesis. To understand and control chirality evolution in gold NPs, we demonstrated the synthesis of chiral gold nanoparticles using dipeptide γ-Glu-Cys and Cys-Gly. The dramatic difference of two dipeptides on chiral development were analyzed in terms of the final morphology, growth pathway, and peptide concentration. The representative morphology of γ-Glu-Cys-directed nanoparticles showed a cube-like outline with protruded chiral wing with 4-fold symmetry. On the other hand, the nanoparticle synthesized in the presence of Cys-Gly exhibited a rhombic dodecahedron-like outline, with curved edges and elliptical cavities on each face. In addition, tntermediate morphology anslysis indicated gold nanoparticles synthesized with γ-Glu-Cys followed an intermediate morphology of concave hexoctahedron, while the nanoparticle synthesized with Cys-Gly formed a concave rhombic dodecahedron. These two clearly distinct intermediate morphologies provided a separate starting point for chiral development. Resulting from the morphological differences, two nanoparticles displayed diverging chiroptic response as γ-Glu-Cys produced a positive main peak and Cys-Gly produced a negative main peak. This suggests that the chiral structure and resulting chiroptic response can be modulated through understanding the interaction between peptides and gold surfaces.

Role of peptides in evolving chirality to materials can vary and be diversified depending on the material. We presented synthesis of chiral cobalt oxide nanoparticle with g-factor of 0.01 in visible range using Tyr-Tyr-Cys ligand. The role of the chemical parameters that can determine the chirality evolution in the nanoparticles was elucidated and the synthetic condition was optimized for a large chiroptic response through experimental demonstration. In addition, the 2D NMR analysis revealed that the thiol group and carboxylic group of the Tyr-Tyr-Cys ligand were aligned in single direction on the nanoparticle, indicating their strong

interaction with the nanoparticle surfaces. Furthermore, the sequence effect of Tyr-Tyr-Cys developing chiral nanoparticle was analyzed. The C-terminal carboxylic group of the peptide exhibited a dominant effect on the chirality expression of the nanoparticle. The use of Cys-Tyr-Tyr and cysteine instead of Tyr-Tyr-Cys generated different chiroptic responses, which are expected to be the effect of exposed amine groups. Interestingly, due to the magnetic properties of chiral cobalt oxide nanoparticle, the chiroptic properties could be modulated by an external magnetic field. The MCD measurement demonstrated that the CD response in the UV and visible region of the nanoparticles dramatically changed under a magnetic field of 1.6 T. The study on Tyr-Tyr-Cys-directed chiral cobalt oxide nanoparticle suggests that the role of the peptides can vary depending on the interacting material, which imparts tunability to chiroptic properties and thus makes it possible to be applied to optoelectronic devices, active displays, and chiral catalysts.

Through plasmon coupling, the chiroptic properties of plasmonic nanostructure can be amplified and sensitively controlled. We demonstrated the fabrication of metamaterial by coating chiral gold nanoparticles on a substrate and depositing a nanoscale plasmonic metal layer, and investigate its optical responses. In order to investigate changes in optical properties due to plasmon coupling, diffuse reflectance CD spectroscopy was utilized along with conventional transmission-based CD spectroscopy. Through this, it was confirmed that the resonance position, magnitude, and sign of the CD spectrum were largely changed by plasmon coupling. In addition, the change in coupled plasmon mode were related to structural parameter in nanoscale, such as the dimension, distance, and refractive index of the nanostructure. Furthermore, we demonstrated the modulation of the structure and optical properties of plasmonic nanoparticles by synthesizing chiral gold-silica core-shell NPs, facilitating their application to tailored plasmon coupling.

From this study, I believe it was possible to understand the role of peptides in developing chiral structure. Furthermore, based on this understanding, manipulation of circular dichroism of chiral nanostructures and establishment of effective platform for tailored plasmon coupling were possible. Insights from this study could provide theoretical guidelines for designing chiro-optical responses for the integration of chiral metamaterials into practical devices, shah as active displays, holography, chirality sensing, chiral catalyst and all-angle negative-refractive-index materials.

References

(1) Schilthuizen, M.; Davison, A. The Convoluted Evolution of Snail Chirality. *Naturwissenschaften* **2005**, *92* (11), 504–515. https://doi.org/10.1007/s00114-05-0045-2.

(2) Schröder-Turk, G. E.; Wickham, S.; Averdunk, H.; Brink, F.; Fitz Gerald, J. D.; Poladian, L.; Large, M. C. J.; Hyde, S. T. The Chiral Structure of Porous Chitin within the Wing-Scales of Callophrys Rubi. *J. Struct. Biol.* **2011**, *174* (2), 290–295. https://doi.org/10.1016/j.jsb.2011.01.004.

(3) Inaki, M.; Liu, J.; Matsuno, K. Cell Chirality: Its Origin and Roles in Left-Right Asymmetric Development. *Philos. Trans. R. Soc. B Biol. Sci.* **2016**, *371* (1710). https://doi.org/10.1098/rstb.2015.0403.

(4) Tee, Y. H.; Shemesh, T.; Thiagarajan, V.; Hariadi, R. F.; Anderson, K. L.; Page, C.; Volkmann, N.; Hanein, D.; Sivaramakrishnan, S.; Kozlov, M. M.; Bershadsky, A. D. Cellular Chirality Arising from the Self-Organization of the Actin Cytoskeleton. *Nat. Cell Biol.* **2015**, *17* (4), 445–457. https://doi.org/10.1038/ncb3137.

(5) Jiang, W.; Yi, X.; McKee, M. D. Chiral Biomineralized Structures and Their Biomimetic Synthesis. *Mater. Horizons* **2019**, *6* (10), 1974–1990. https://doi.org/10.1039/c9mh00431a.

(6) Levin, M. Left-Right Asymmetry in Embryonic Development: A Comprehensive Review. *Mech. Dev.* **2005**, *122* (1), 3–25. https://doi.org/10.1016/j.mod.2004.08.006.

(7) Mason, S. F. Origins of Biomolecular Handedness. *Nature* **1984**, *311*

(5981), 19–23. https://doi.org/10.1038/311019a0.

(8) Brown, N. A.; Wolpert, L. The Development of Handedness in Left/Right Asymmetry. *Development* **1990**, *109* (1), 1–9.

(9) Salam, A. The Role of Chirality in the Origin of Life. *J. Mol. Evol.* **1991**, *33*, 105–113.

(10) Morrow, S. M.; Bissette, A. J.; Fletcher, S. P. Transmission of Chirality through Space and across Length Scales. *Nat. Nanotechnol.* **2017**, *12* (5), 410–419. https://doi.org/10.1038/nnano.2017.62.

(11) Lebreton, G.; Géminard, C.; Lapraz, F.; Pyrpassopoulos, S.; Cerezo, D.; Spéder, P.; Ostap, E. M.; Noselli, S. Molecular to Organismal Chirality Is Induced by the Conserved Myosin 1D. *Science* **2018**, *362* (6417), 949–952. https://doi.org/10.1126/science.aat8642.

(12) Wharton, S. J.; Basu, S. P.; Ashe, H. L. Body Handedness Is Directed by Genetically Determined Cytoskeletal Dynamics in the Early Embryo. *Curr. Biol.* **2004**, *14*, 1550–1558. https://doi.org/10.1016/j.

(13) Lekner, J. Optical Properties of Isotropic Chiral Media. *Pure Appl. Opt. J. Eur. Opt. Soc. Part A* **1996**, *5* (4), 417–443. https://doi.org/10.1088/0963-9659/5/4/008.

(14) Glazer, A. M.; Stadnicka, K. On the Origin of Optical Activity in Crystal Structures. *J. Appl. Crystallogr.* **1986**, *19* (2), 108–122. https://doi.org/10.1107/S0021889886089823.

(15) Wang, P.; Yu, S.-J.; Govorov, A. O.; Ouyang, M. Cooperative Expression of Atomic Chirality in Inorganic Nanostructures. *Nat. Commun.* **2017**, *8* (1), 14312. https://doi.org/10.1038/ncomms14312.

(16) Hazen, R. M. Chiral Crystal Faces of Common Rock-Forming Minerals. In *Progress in Biological Chirality*; Elsevier, 2004; pp 137–151. https://doi.org/10.1016/B978-008044396-6/50013-7.

(17) Horvath, J. D.; Gellman, A. J. Naturally Chiral Surfaces. *Top. Catal.* **2003**, *25* (1–4), 9–15. https://doi.org/10.1023/B:TOCA.0000003094.07345.d1.

(18) Gibbs, R. E. Structure of Formula Quartz. *Proc. R. Soc. A Math. Phys. Eng. Sci.* **2006**, *110* (754), 443–455. https://doi.org/10.1098/rspa.1926.0025.

(19) Hazen, R. M.; Sholl, D. S. Chiral Selection on Inorganic Crystalline Surfaces. *Nat. Mater.* **2003**, *2* (6), 367–374. https://doi.org/10.1038/nmat879.

(20) Pendry, J. B. A Chiral Route to Negative Refraction. *Science* **2004**, *306* (5700), 1353–1355. https://doi.org/10.1126/science.1104467.

(21) Hendry, E.; Carpy, T.; Johnston, J.; Popland, M.; Mikhaylovskiy, R. V.; Lapthorn, A. J.; Kelly, S. M.; Barron, L. D.; Gadegaard, N.; Kadodwala, M. Ultrasensitive Detection and Characterization of Biomolecules Using Superchiral Fields. *Nat. Nanotechnol.* **2010**, *5* (11), 783–787. https://doi.org/10.1038/nnano.2010.209.

(22) Gansel, J. K.; Thiel, M.; Rill, M. S.; Decker, M.; Bade, K.; Saile, V.; Von Freymann, G.; Linden, S.; Wegener, M. Gold Helix Photonic Metamaterial

as Broadband Circular Polarizer. *Science* **2009**, *325* (5947), 1513–1515. https://doi.org/10.1126/science.1177031.

(23) Zhang, H.; Zheng, X.; Kwok, R. T. K.; Wang, J.; Leung, N. L. C.; Shi, L.; Sun, J. Z.; Tang, Z.; Lam, J. W. Y.; Qin, A.; Tang, B. Z. In Situ Monitoring of Molecular Aggregation Using Circular Dichroism. *Nat. Commun.* **2018**, *9* (1), 4961. https://doi.org/10.1038/s41467-018-07299-3.

(24) Greenfield, N. J. Using Circular Dichroism Spectra to Estimate Protein Secondary Structure. *Nat. Protoc.* **2006**, *1* (6), 2876–2890. https://doi.org/10.1038/nprot.2006.202.

(25) Hoffmann, M.; Grajewski, J.; Gawronski, J. Extending the Applications of Circular Dichroism in Structure Elucidation: Aqueous Environment Breaks the Symmetry of Tartrate Dianion. *New J. Chem.* **2010**, *34* (9), 2020. https://doi.org/10.1039/c0nj00072h.

(26) Xiong, W.; Mazid, R.; Yap, L. W.; Li, X.; Cheng, W. Plasmonic Caged Gold Nanorods for Near-Infrared Light Controlled Drug Delivery. *Nanoscale* **2014**, *6* (23), 14388–14393. https://doi.org/10.1039/C4NR04400B.

(27) Liu, S.-D.; Liu, J.-Y.; Cao, Z.; Fan, J.-L.; Lei, D. Dynamic Tuning of Enhanced Intrinsic Circular Dichroism in Plasmonic Stereo-Metamolecule Array with Surface Lattice Resonance. *Nanophotonics* **2020**, *9* (10), 3419–3434. https://doi.org/10.1515/nanoph-2020-0130.

(28) Zhang, S.; Zhou, J.; Park, Y.-S.; Rho, J.; Singh, R.; Nam, S.; Azad, A. K.; Chen, H.-T.; Yin, X.; Taylor, A. J.; Zhang, X. Photoinduced Handedness

Switching in Terahertz Chiral Metamolecules. *Nat. Commun.* **2012**, *3* (1), 942. https://doi.org/10.1038/ncomms1908.

(29) Meinzer, N.; Barnes, W. L.; Hooper, I. R. Plasmonic Meta-Atoms and Metasurfaces. *Nat. Photonics* **2014**, *8* (12), 889–898. https://doi.org/10.1038/nphoton.2014.247.

(30) Plum, E.; Zhou, J.; Dong, J.; Fedotov, V. A.; Koschny, T.; Soukoulis, C. M.; Zheludev, N. I. Metamaterial with Negative Index Due to Chirality. *Phys. Rev. B* **2009**, *79* (3), 035407. https://doi.org/10.1103/PhysRevB.79.035407.

(31) Zhang, S.; Park, Y.-S.; Li, J.; Lu, X.; Zhang, W.; Zhang, X. Negative Refractive Index in Chiral Metamaterials. *Phys. Rev. Lett.* **2009**, *102* (2), 023901. https://doi.org/10.1103/PhysRevLett.102.023901.

(32) Tang, Y.; Cohen, A. E. Optical Chirality and Its Interaction with Matter. *Phys. Rev. Lett.* **2010**, *104* (16), 163901. https://doi.org/10.1103/PhysRevLett.104.163901.

(33) Hendry, E.; Carpy, T.; Johnston, J.; Popland, M.; Mikhaylovskiy, R. V.; Lapthorn, A. J.; Kelly, S. M.; Barron, L. D.; Gadegaard, N.; Kadodwala, M. Ultrasensitive Detection and Characterization of Biomolecules Using Superchiral Fields. *Nat. Nanotechnol.* **2010**, *5* (11), 783–787. https://doi.org/10.1038/nnano.2010.209.

(34) Yu, N.; Genevet, P.; Kats, M. A.; Aieta, F.; Tetienne, J.-P.; Capasso, F.; Gaburro, Z. Light Propagation with Phase Discontinuities: Generalized Laws of Reflection and Refraction. *Science* **2011**, *334* (6054), 333–337.

https://doi.org/10.1126/science.1210713.

(35) Zheng, G.; Mühlenbernd, H.; Kenney, M.; Li, G.; Zentgraf, T.; Zhang, S. Metasurface Holograms Reaching 80% Efficiency. *Nat. Nanotechnol.* **2015**, *10* (4), 308–312. https://doi.org/10.1038/nnano.2015.2.

(36) Karimi, E.; Schulz, S. A.; De Leon, I.; Qassim, H.; Upham, J.; Boyd, R. W. Generating Optical Orbital Angular Momentum at Visible Wavelengths Using a Plasmonic Metasurface. *Light Sci. Appl.* **2014**, *3* (5), e167–e167. https://doi.org/10.1038/lsa.2014.48.

(37) Gansel, J. K.; Latzel, M.; Frölich, A.; Kaschke, J.; Thiel, M.; Wegener, M. Tapered Gold-Helix Metamaterials as Improved Circular Polarizers. *Appl. Phys. Lett.* **2012**, *100* (10), 101109. https://doi.org/10.1063/1.3693181.

(38) Hentschel, M.; Schäferling, M.; Weiss, T.; Liu, N.; Giessen, H. Three-Dimensional Chiral Plasmonic Oligomers. *Nano Lett.* **2012**, *12* (5), 2542–2547. https://doi.org/10.1021/nl300769x.

(39) Radke, A.; Gissibl, T.; Klotzbücher, T.; Braun, P. V.; Giessen, H. Three-Dimensional Bichiral Plasmonic Crystals Fabricated by Direct Laser Writing and Electroless Silver Plating. *Adv. Mater.* **2011**, *23* (27), 3018–3021. https://doi.org/10.1002/adma.201100543.

(40) Decker, M.; Zhao, R.; Soukoulis, C. M.; Linden, S.; Wegener, M. Twisted Split-Ring-Resonator Photonic Metamaterial with Huge Optical Activity. *Opt. Lett.* **2010**, *35* (10), 1593. https://doi.org/10.1364/ol.35.001593.

(41) Soukoulis, C. M.; Wegener, M. Past Achievements and Future Challenges

in the Development of Three-Dimensional Photonic Metamaterials. *Nat. Photonics* **2011**, *5* (9), 523–530. https://doi.org/10.1038/nphoton.2011.154.

(42) Valev, V. K.; Baumberg, J. J.; Sibilia, C.; Verbiest, T. Chirality and Chiroptical Effects in Plasmonic Nanostructures: Fundamentals, Recent Progress, and Outlook. *Adv. Mater.* **2013**, *25* (18), 2517–2534. https://doi.org/10.1002/adma.201205178.

(43) Dietrich, K.; Lehr, D.; Helgert, C.; Tünnermann, A.; Kley, E. B. Circular Dichroism from Chiral Nanomaterial Fabricated by On-Edge Lithography. *Adv. Mater.* **2012**, *24* (44), 321–325. https://doi.org/10.1002/adma.201203424.

(44) Frank, B.; Yin, X.; Schäferling, M.; Zhao, J.; Hein, S. M.; Braun, P. V.; Giessen, H. Large-Area 3D Chiral Plasmonic Structures. *ACS Nano* **2013**, *7* (7), 6321–6329. https://doi.org/10.1021/nn402370x.

(45) Hou, Y.; Li, S.; Su, Y.; Huang, X.; Liu, Y.; Huang, L.; Yu, Y.; Gao, F.; Zhang, Z.; Du, J. Design and Fabrication of Three-Dimensional Chiral Nanostructures Based on Stepwise Glancing Angle Deposition Technology. *Langmuir* **2013**, *29* (3), 867–872. https://doi.org/10.1021/la304122f.

(46) Xia, Y.; Zhou, Y.; Tang, Z. Chiral Inorganic Nanoparticles: Origin, Optical Properties and Bioapplications. *Nanoscale* **2011**, *3* (4), 1374–1382. https://doi.org/10.1039/c0nr00903b.

(47) Ben-Moshe, A.; Maoz, B. M.; Govorov, A. O.; Markovich, G. Chirality and Chiroptical Effects in Inorganic Nanocrystal Systems with Plasmon and Exciton Resonances. *Chem. Soc. Rev.* **2013**, *42* (16), 7028–7041.

https://doi.org/10.1039/c3cs60139k.

(48) Wang, Z.; Cheng, F.; Winsor, T.; Liu, Y. Optical Chiral Metamaterials: A Review of the Fundamentals, Fabrication Methods and Applications. *Nanotechnology* **2016**, *27* (41), 412001. https://doi.org/10.1088/0957-4484/27/41/412001.

(49) Shekhar, P.; Atkinson, J.; Jacob, Z. Hyperbolic Metamaterials: Fundamentals and Applications. *Nano Converg.* **2014**, *1* (1), 14. https://doi.org/10.1186/s40580-014-0014-6.

(50) Oh, S. S.; Hess, O. Chiral Metamaterials: Enhancement and Control of Optical Activity and Circular Dichroism. *Nano Converg.* **2015**, *2* (1), 24. https://doi.org/10.1186/s40580-015-0058-2.

(51) Tohgha, U.; Varga, K.; Balaz, M. Achiral CdSe Quantum Dots Exhibit Optical Activity in the Visible Region upon Post-Synthetic Ligand Exchange with d- or l-Cysteine. *Chem. Commun.* **2013**, *49* (18), 1844–1846. https://doi.org/10.1039/c3cc37987f.

(52) Gao, X.; Zhang, X.; Zhao, L.; Huang, P.; Han, B.; Lv, J.; Qiu, X.; Wei, S. H.; Tang, Z. Distinct Excitonic Circular Dichroism between Wurtzite and Zincblende CdSe Nanoplatelets. *Nano Lett.* **2018**, *18* (11), 6665–6671. https://doi.org/10.1021/acs.nanolett.8b01001.

(53) Tohgha, U.; Deol, K. K.; Porter, A. G.; Bartko, S. G.; Choi, J. K.; Leonard, B. M.; Varga, K.; Kubelka, J.; Muller, G.; Balaz, M. Ligand Induced Circular Dichroism and Circularly Polarized Luminescence in Cdse Quantum Dots. *ACS Nano* **2013**, *7* (12), 11094–11102.

https://doi.org/10.1021/nn404832f.

(54) Cheng, J.; Hao, J.; Liu, H.; Li, J.; Li, J.; Zhu, X.; Lin, X.; Wang, K.; He, T. Optically Active CdSe-Dot/CdS-Rod Nanocrystals with Induced Chirality and Circularly Polarized Luminescence. *ACS Nano* **2018**, *12* (6), 5341–5350. https://doi.org/10.1021/acsnano.8b00112.

(55) Ben-Moshe, A.; Teitelboim, A.; Oron, D.; Markovich, G. Probing the Interaction of Quantum Dots with Chiral Capping Molecules Using Circular Dichroism Spectroscopy. *Nano Lett.* **2016**, *16* (12), 7467–7473. https://doi.org/10.1021/acs.nanolett.6b03143.

(56) Ben Moshe, A.; Szwarcman, D.; Markovich, G. Size Dependence of Chiroptical Activity in Colloidal Quantum Dots. *ACS Nano* **2011**, *5* (11), 9034–9043. https://doi.org/10.1021/nn203234b.

(57) Naito, M.; Iwahori, K.; Miura, A.; Yamane, M.; Yamashita, I. Circularly Polarized Luminescent CDs Quantum Dots Prepared in a Protein Nanocage. *Angew. Chemie - Int. Ed.* **2010**, *49* (39), 7006–7009. https://doi.org/10.1002/anie.201002552.

(58) Zhou, Y.; Zhu, Z.; Huang, W.; Liu, W.; Wu, S.; Liu, X.; Gao, Y.; Zhang, W.; Tang, Z. Optical Coupling between Chiral Biomolecules and Semiconductor Nanoparticles: Size-Dependent Circular Dichroism Absorption. *Angew. Chemie - Int. Ed.* **2011**, *50* (48), 11456–11459. https://doi.org/10.1002/anie.201103762.

(59) Gao, X.; Zhang, X.; Deng, K.; Han, B.; Zhao, L.; Wu, M.; Shi, L.; Lv, J.; Tang, Z. Excitonic Circular Dichroism of Chiral Quantum Rods. *J. Am.*

Chem. Soc. **2017**, *139* (25), 8734–8739. https://doi.org/10.1021/jacs.7b04224.

(60) Yang, G.; Kazes, M.; Oron, D. Chiral 2D Colloidal Semiconductor Quantum Wells. *Adv. Funct. Mater.* **2018**, *28* (28), 1–9. https://doi.org/10.1002/adfm.201802012.

(61) Govorov, A. O.; Fan, Z.; Hernandez, P.; Slocik, J. M.; Naik, R. R. Theory of Circular Dichroism of Nanomaterials Comprising Chiral Molecules and Nanocrystals: Plasmon Enhancement, Dipole Interactions, and Dielectric Effects. *Nano Lett.* **2010**, *10* (4), 1374–1382. https://doi.org/10.1021/nl100010v.

(62) Tanaka, T.; Ishikawa, A. Towards Three-Dimensional Optical Metamaterials. *Nano Converg.* **2017**, *4* (1), 34. https://doi.org/10.1186/s40580-017-0129-7.

(63) Cai, C.; Lin, J.; Lu, Y.; Zhang, Q.; Wang, L. Polypeptide Self-Assemblies: Nanostructures and Bioapplications. *Chem. Soc. Rev.* **2016**, *45* (21), 5985–6012. https://doi.org/10.1039/c6cs00013d.

(64) Wang, Y.; Xu, J.; Wang, Y.; Chen, H. Emerging Chirality in Nanoscience. *Chem. Soc. Rev.* **2013**, *42* (7), 2930–2962. https://doi.org/10.1039/c2cs35332f.

(65) Hazen, R. M.; Filley, T. R.; Goodfriend, G. A. Selective Adsorption of L- and D-Amino Acids on Calcite: Implications for Biochemical Homochirality. *Proc. Natl. Acad. Sci.* **2001**, *98* (10), 5487–5490. https://doi.org/10.1073/pnas.101085998.

(66) Edward Salisbury Dana, W. E. F. *A Textbook of Mineralogy*, 4th Ed.; Wiley, New York, 1958.

(67) Teng, H. H. Thermodynamics of Calcite Growth: Baseline for Understanding Biomineral Formation. *Science* **1998**, *282* (5389), 724–727. https://doi.org/10.1126/science.282.5389.724.

(68) Orme, C. A.; Noy, A.; Wierzbicki, A.; McBride, M. T.; Grantham, M.; Teng, H. H.; Dove, P. M.; DeYoreo, J. J. Formation of Chiral Morphologies through Selective Binding of Amino Acids to Calcite Surface Steps. *Nature* **2001**, *411* (6839), 775–779. https://doi.org/10.1038/35081034.

(69) Yuya Oaki, H. I. Amplification of Chirality from Molecules into Morphology of Crystals through Molecular Recognition. *J. Am. Chem. Soc.* **2004**, *126* (30), 9271–9275. https://doi.org//10.1021/ja048661.

(70) Ben-Moshe, A.; Wolf, S. G.; Sadan, M. B.; Houben, L.; Fan, Z.; Govorov, A. O.; Markovich, G. Enantioselective Control of Lattice and Shape Chirality in Inorganic Nanostructures Using Chiral Biomolecules. *Nat. Commun.* **2014**, *5* (1), 4302. https://doi.org/10.1038/ncomms5302.

(71) Fan, Z.; Govorov, A. O. Chiral Nanocrystals: Plasmonic Spectra and Circular Dichroism. *Nano Lett.* **2012**, *12* (6), 3283–3289. https://doi.org/10.1021/nl3013715.

(72) Jiang, W.; Pacella, M. S.; Athanasiadou, D.; Nelea, V.; Vali, H.; Hazen, R. M.; Gray, J. J.; McKee, M. D. Chiral Acidic Amino Acids Induce Chiral Hierarchical Structure in Calcium Carbonate. *Nat. Commun.* **2017**, *8* (1), 15066. https://doi.org/10.1038/ncomms15066.

(73) Jiang, W.; Pacella, M. S.; Vali, H.; Gray, J. J.; McKee, M. D. Chiral Switching in Biomineral Suprastructures Induced by Homochiral L-Amino Acid. *Sci. Adv.* **2018**, *4* (8), eaas9819. https://doi.org/10.1126/sciadv.aas9819.

(74) Duan, Y.; Liu, X.; Han, L.; Asahina, S.; Xu, D.; Cao, Y.; Yao, Y.; Che, S. Optically Active Chiral CuO "Nanoflowers." *J. Am. Chem. Soc.* **2014**, *136* (20), 7193–7196. https://doi.org/10.1021/ja500197e.

(75) Duan, Y.; Han, L.; Zhang, J.; Asahina, S.; Huang, Z.; Shi, L.; Wang, B.; Cao, Y.; Yao, Y.; Ma, L.; Wang, C.; Dukor, R. K.; Sun, L.; Jiang, C.; Tang, Z.; Nafie, L. A.; Che, S. Optically Active Nanostructured ZnO Films. *Angew. Chemie - Int. Ed.* **2015**, *54* (50), 15170–15175. https://doi.org/10.1002/anie.201507502.

(76) Cho, N. H.; Lee, H.; Ahn, H.; Lee, Y. Y.; Im, S. W.; Kim, H.; Nam, K. T. Cysteine Induced Chiral Morphology in Palladium Nanoparticle. *Part. Part. Syst. Charact.* **2019**, *36* (5), 1900062. https://doi.org/10.1002/ppsc.201900062.

(77) Lee, H.-E.; Lee, J.; Ju, M.; Ahn, H.-Y.; Lee, Y. Y.; Jang, H.-S.; Nam, K. T. Identifying Peptide Sequences That Can Control the Assembly of Gold Nanostructures. *Mol. Syst. Des. Eng.* **2018**, *3* (3), 581–590. https://doi.org/10.1039/C7ME00091J.

(78) Kong, X. T.; Besteiro, L. V.; Wang, Z.; Govorov, A. O. Plasmonic Chirality and Circular Dichroism in Bioassembled and Nonbiological Systems: Theoretical Background and Recent Progress. *Adv. Mater.* **2018**, *1801790*, 1–14. https://doi.org/10.1002/adma.201801790.

(79) Yan, J.; Chen, Y.; Hou, S.; Chen, J.; Meng, D.; Zhang, H.; Fan, H.; Ji, Y.; Wu, X. Fabricating Chiroptical Starfruit-like Au Nanoparticles via Interface Modulation of Chiral Thiols. *Nanoscale* **2017**, *9* (31), 11093–11102. https://doi.org/10.1039/C7NR03712K.

(80) Maoz, B. M.; Van Der Weegen, R.; Fan, Z.; Govorov, A. O.; Ellestad, G.; Berova, N.; Meijer, E. W.; Markovich, G. Plasmonic Chiroptical Response of Silver Nanoparticles Interacting with Chiral Supramolecular Assemblies. *J. Am. Chem. Soc.* **2012**, *134* (42), 17807–17813. https://doi.org/10.1021/ja309016k.

(81) Shemer, G.; Krichevski, O.; Markovich, G.; Molotsky, T.; Lubitz, I.; Kotlyar, A. B. Chirality of Silver Nanoparticles Synthesized on DNA. *J. Am. Chem. Soc.* **2006**, *128* (34), 11006–11007. https://doi.org/10.1021/ja063702i.

(82) Hirai, K.; Yeom, B.; Sada, K. Pyrolysis of Helical Coordination Polymers for Metal-Sulfide-Based Helices with Broadband Chiroptical Activity. *ACS Nano* **2017**, *11* (6), 5309–5317. https://doi.org/10.1021/acsnano.7b00103.

(83) Cheng, J.; Le Saux, G.; Gao, J.; Buffeteau, T.; Battie, Y.; Barois, P.; Ponsinet, V.; Delville, M. H.; Ersen, O.; Pouget, E.; Oda, R. GoldHelix: Gold Nanoparticles Forming 3D Helical Superstructures with Controlled Morphology and Strong Chiroptical Property. *ACS Nano* **2017**, *11* (4), 3806–3818. https://doi.org/10.1021/acsnano.6b08723.

(84) Lee, H.-E.; Ahn, H.-Y.; Lee, J.; Nam, K. T. Biomolecule-Enabled Chiral Assembly of Plasmonic Nanostructures. *ChemNanoMat* **2017**, *3* (10), 685–697. https://doi.org/10.1002/cnma.201700208.

(85) Karagoz, B.; Payne, M.; Reinicker, A.; Kondratyuk, P.; Gellman, A. J. A Most Enantioselective Chiral Surface: Tartaric Acid on All Surfaces Vicinal to Cu(110). *Langmuir* **2019**, *35* (50), 16438–16443. https://doi.org/10.1021/acs.langmuir.9b02476.

(86) Ahmadi, A.; Attard, G.; Feliu, J.; Rodes, A. Surface Reactivity at "Chiral" Platinum Surfaces. *Langmuir* **1999**, *15* (7), 2420–2424. https://doi.org/10.1021/la9810915.

(87) Lee, H.-E.; Ahn, H.-Y.; Mun, J.; Lee, Y. Y.; Kim, M.; Cho, N. H.; Chang, K.; Kim, W. S.; Rho, J.; Nam, K. T. Amino-Acid- and Peptide-Directed Synthesis of Chiral Plasmonic Gold Nanoparticles. *Nature* **2018**, *556* (7701), 360–365. https://doi.org/10.1038/s41586-018-0034-1.

(88) Ahn, H.-Y.; Lee, H.-E.; Jin, K.; Nam, K. T. Extended Gold Nano-Morphology Diagram: Synthesis of Rhombic Dodecahedra Using CTAB and Ascorbic Acid. *J. Mater. Chem. C* **2013**, *1* (41), 6861. https://doi.org/10.1039/c3tc31135j.

(89) Lee, H.-E.; Yang, K. D.; Yoon, S. M.; Ahn, H.-Y.; Lee, Y. Y.; Chang, H.; Jeong, D. H.; Lee, Y.-S.; Kim, M. Y.; Nam, K. T. Concave Rhombic Dodecahedral Au Nanocatalyst with Multiple High-Index Facets for CO 2 Reduction. *ACS Nano* **2015**, *9* (8), 8384–8393. https://doi.org/10.1021/acsnano.5b03065.

(90) Ahn, H.-Y.; Lee, H.-E.; Jin, K.; Nam, K. T. Extended Gold Nano-Morphology Diagram: Synthesis of Rhombic Dodecahedra Using CTAB and Ascorbic Acid. *J. Mater. Chem. C* **2013**, *1* (41), 6861. https://doi.org/10.1039/c3tc31135j.

(91) Lee, W.; Tonelli, M.; Markley, J. L. NMRFAM-SPARKY: Enhanced Software for Biomolecular NMR Spectroscopy. *Bioinformatics* **2015**, *31* (8), 1325–1327. https://doi.org/10.1093/bioinformatics/btu830.

(92) Herrmann, T.; Güntert, P.; Wüthrich, K. Protein NMR Structure Determination with Automated NOE Assignment Using the New Software CANDID and the Torsion Angle Dynamics Algorithm DYANA. *J. Mol. Biol.* **2002**, *319* (1), 209–227. https://doi.org/10.1016/S0022-2836(02)00241-3.

(93) Baimuratov, A. S.; Gun'ko, Y. K.; Shalkovskiy, A. G.; Baranov, A. V.; Fedorov, A. V.; Rukhlenko, I. D. Optical Activity of Chiral Nanoscrolls. *Adv. Opt. Mater.* **2017**, *5* (16), 1600982. https://doi.org/10.1002/adom.201600982.

(94) Hao, C.; Xu, L.; Kuang, H.; Xu, C. Artificial Chiral Probes and Bioapplications. *Adv. Mater.* **2019**, *16* (3), 1802075. https://doi.org/10.1002/adma.201802075.

(95) Esposito, M.; Todisco, F.; Bakhti, S.; Passaseo, A.; Tarantini, I.; Cuscunà, M.; Destouches, N.; Tasco, V. Symmetry Breaking in Oligomer Surface Plasmon Lattice Resonances. *Nano Lett.* **2019**, *19* (3), 1922–1930. https://doi.org/10.1021/acs.nanolett.8b05062.

(96) Wu, Z.; Zheng, Y. Moiré Chiral Metamaterials. *Adv. Opt. Mater.* **2017**, *5* (16), 1700034. https://doi.org/10.1002/adom.201700034.

(97) Ahn, H.-Y.; Yoo, S.; Cho, N. H.; Kim, R. M.; Kim, H.; Huh, J.-H.; Lee, S.; Nam, K. T. Bioinspired Toolkit Based on Intermolecular Encoder toward

Evolutionary 4D Chiral Plasmonic Materials. *Acc. Chem. Res.* **2019**, *52* (10), 2768–2783. https://doi.org/10.1021/acs.accounts.9b00264.

(98) Zhang, S.; Park, Y.-S.; Li, J.; Lu, X.; Zhang, W.; Zhang, X. Negative Refractive Index in Chiral Metamaterials. *Phys. Rev. Lett.* **2009**, *102* (2), 023901. https://doi.org/10.1103/PhysRevLett.102.023901.

(99) Schäferling, M.; Yin, X.; Engheta, N.; Giessen, H. Helical Plasmonic Nanostructures as Prototypical Chiral Near-Field Sources. *ACS Photonics* **2014**, *1* (6), 530–537. https://doi.org/10.1021/ph5000743.

(100) Tullius, R.; Karimullah, A. S.; Rodier, M.; Fitzpatrick, B.; Gadegaard, N.; Barron, L. D.; Rotello, V. M.; Cooke, G.; Lapthorn, A.; Kadodwala, M. "Superchiral" Spectroscopy: Detection of Protein Higher Order Hierarchical Structure with Chiral Plasmonic Nanostructures. *J. Am. Chem. Soc.* **2015**, *137* (26), 8380–8383. https://doi.org/10.1021/jacs.5b04806.

(101) Wen, D.; Yue, F.; Li, G.; Zheng, G.; Chan, K.; Chen, S.; Chen, M.; Li, K. F.; Wong, P. W. H.; Cheah, K. W.; Yue Bun Pun, E.; Zhang, S.; Chen, X. Helicity Multiplexed Broadband Metasurface Holograms. *Nat. Commun.* **2015**, *6* (1), 8241. https://doi.org/10.1038/ncomms9241.

(102) Khorasaninejad, M.; Ambrosio, A.; Kanhaiya, P.; Capasso, F. Broadband and Chiral Binary Dielectric Meta-Holograms. *Sci. Adv.* **2016**, *2* (5), e1501258. https://doi.org/10.1126/sciadv.1501258.

(103) Jack, C.; Karimullah, A. S.; Leyman, R.; Tullius, R.; Rotello, V. M.; Cooke, G.; Gadegaard, N.; Barron, L. D.; Kadodwala, M. Biomacromolecular Stereostructure Mediates Mode Hybridization in Chiral Plasmonic

Nanostructures. *Nano Lett.* **2016**, *16* (9), 5806–5814. https://doi.org/10.1021/acs.nanolett.6b02549.

(104) Zhao, Y.; Askarpour, A. N.; Sun, L.; Shi, J.; Li, X.; Alù, A. Chirality Detection of Enantiomers Using Twisted Optical Metamaterials. *Nat. Commun.* **2017**, *8* (1), 14180. https://doi.org/10.1038/ncomms14180.

(105) Tullius, R.; Platt, G. W.; Khosravi Khorashad, L.; Gadegaard, N.; Lapthorn, A. J.; Rotello, V. M.; Cooke, G.; Barron, L. D.; Govorov, A. O.; Karimullah, A. S.; Kadodwala, M. Superchiral Plasmonic Phase Sensitivity for Fingerprinting of Protein Interface Structure. *ACS Nano* **2017**, *11* (12), 12049–12056. https://doi.org/10.1021/acsnano.7b04698.

(106) Kelly, C.; Tullius, R.; Lapthorn, A. J.; Gadegaard, N.; Cooke, G.; Barron, L. D.; Karimullah, A. S.; Rotello, V. M.; Kadodwala, M. Chiral Plasmonic Fields Probe Structural Order of Biointerfaces. *J. Am. Chem. Soc.* **2018**, *140* (27), 8509–8517. https://doi.org/10.1021/jacs.8b03634.

(107) Duan, X.; Kamin, S.; Sterl, F.; Giessen, H.; Liu, N. Hydrogen-Regulated Chiral Nanoplasmonics. *Nano Lett.* **2016**, *16* (2), 1462–1466. https://doi.org/10.1021/acs.nanolett.5b05105.

(108) Liu, Z.; Du, H.; Li, J.; Lu, L.; Li, Z.-Y.; Fang, N. X. Nano-Kirigami with Giant Optical Chirality. *Sci. Adv.* **2018**, *4* (7), eaat4436. https://doi.org/10.1126/sciadv.aat4436.

(109) Haynes, C. L.; Van Duyne, R. P. Plasmon-Sampled Surface-Enhanced Raman Excitation Spectroscopy †. *J. Phys. Chem. B* **2003**, *107* (30), 7426–7433. https://doi.org/10.1021/jp027749b.

(110) Lan, X.; Lu, X.; Shen, C.; Ke, Y.; Ni, W.; Wang, Q. Au Nanorod Helical Superstructures with Designed Chirality. *J. Am. Chem. Soc.* **2015**, *137* (1), 457–462. https://doi.org/10.1021/ja511333q.

(111) Mastroianni, A. J.; Claridge, S. A.; Alivisatos, A. P. Pyramidal and Chiral Groupings of Gold Nanocrystals Assembled Using DNA Scaffolds. *J. Am. Chem. Soc.* **2009**, *131* (24), 8455–8459. https://doi.org/10.1021/ja808570g.

(112) Kuzyk, A.; Schreiber, R.; Fan, Z.; Pardatscher, G.; Roller, E.-M.; Högele, A.; Simmel, F. C.; Govorov, A. O.; Liedl, T. DNA-Based Self-Assembly of Chiral Plasmonic Nanostructures with Tailored Optical Response. *Nature* **2012**, *483* (7389), 311–314. https://doi.org/10.1038/nature10889.

(113) Mokashi-Punekar, S.; Walsh, T. R.; Rosi, N. L. Tuning the Structure and Chiroptical Properties of Gold Nanoparticle Single Helices via Peptide Sequence Variation. *J. Am. Chem. Soc.* **2019**, *141* (39), 15710–15716. https://doi.org/10.1021/jacs.9b08798.

(114) Querejeta-Fernández, A.; Chauve, G.; Methot, M.; Bouchard, J.; Kumacheva, E. Chiral Plasmonic Films Formed by Gold Nanorods and Cellulose Nanocrystals. *J. Am. Chem. Soc.* **2014**, *136* (12), 4788–4793. https://doi.org/10.1021/ja501642p.

(115) Quan, Z.; Wang, Y.; Fang, J. High-Index Faceted Noble Metal Nanocrystals. *Acc. Chem. Res.* **2013**, *46* (2), 191–202. https://doi.org/10.1021/ar200293n.

(116) Langille, M. R.; Personick, M. L.; Zhang, J.; Mirkin, C. A. Defining Rules for the Shape Evolution of Gold Nanoparticles. *J. Am. Chem. Soc.* **2012**,

134 (35), 14542–14554. https://doi.org/10.1021/ja305245g.

(117) Ahn, H. Y.; Lee, H. E.; Jin, K.; Nam, K. T. Extended Gold Nano-Morphology Diagram: Synthesis of Rhombic Dodecahedra Using CTAB and Ascorbic Acid. *J. Mater. Chem. C* **2013**, *1* (41), 6861–6868. https://doi.org/10.1039/c3tc31135j.

(118) Chen, Q.; Jia, Y.; Xie, S.; Xie, Z. Well-Faceted Noble-Metal Nanocrystals with Nonconvex Polyhedral Shapes. *Chem. Soc. Rev.* **2016**, *45* (11), 3207–3220. https://doi.org/10.1039/c6cs00039h.

(119) Zhang, H.; Jin, M.; Xia, Y. Noble-Metal Nanocrystals with Concave Surfaces: Synthesis and Applications. *Angew. Chemie - Int. Ed.* **2012**, *51* (31), 7656–7673. https://doi.org/10.1002/anie.201201557.

(120) Smith, J. D.; Bladt, E.; Burkhart, J. A. C.; Winckelmans, N.; Koczkur, K. M.; Ashberry, H. M.; Bals, S.; Skrabalak, S. E. Defect-Directed Growth of Symmetrically Branched Metal Nanocrystals. *Angew. Chemie Int. Ed.* **2020**, *59* (2), 943–950. https://doi.org/10.1002/anie.201913301.

(121) Pang, X.; Zhao, L.; Han, W.; Xin, X.; Lin, Z. A General and Robust Strategy for the Synthesis of Nearly Monodisperse Colloidal Nanocrystals. *Nat. Nanotechnol.* **2013**, *8* (6), 426–431. https://doi.org/10.1038/nnano.2013.85.

(122) Fuller, M. A.; Köper, I. Biomedical Applications of Polyelectrolyte Caoated Spherical Gold Nanoparticles. *Nano Converg.* **2019**, *6* (1), 11. https://doi.org/10.1186/s40580-019-0183-4.

(123) Kang, Y. J.; Cutler, E. G.; Cho, H. Therapeutic Nanoplatforms and Delivery Strategies for Neurological Disorders. *Nano Converg.* **2018**, *5* (1), 35. https://doi.org/10.1186/s40580-018-0168-8.

(124) Zhu, Z.; Guan, Z.; Jia, S.; Lei, Z.; Lin, S.; Zhang, H.; Ma, Y.; Tian, Z.-Q.; Yang, C. J. Au@Pt Nanoparticle Encapsulated Target-Responsive Hydrogel with Volumetric Bar-Chart Chip Readout for Quantitative Point-of-Care Testing. *Angew. Chemie Int. Ed.* **2014**, n/a-n/a. https://doi.org/10.1002/anie.201405995.

(125) Im, S. W.; Ahn, H.; Kim, R. M.; Cho, N. H.; Kim, H.; Lim, Y.; Lee, H.; Nam, K. T. Chiral Surface and Geometry of Metal Nanocrystals. *Adv. Mater.* **2019**, 1905758. https://doi.org/10.1002/adma.201905758.

(126) Jana, N. R.; Gearheart, L.; Murphy, C. J. Seed-Mediated Growth Approach for Shape-Controlled Synthesis of Spheroidal and Rod-like Gold Nanoparticles Using a Surfactant Template. *Adv. Mater.* **2001**, *13* (18), 1389–1393. https://doi.org/10.1002/1521-4095(200109)13:18<1389::AID-ADMA1389>3.0.CO;2-F.

(127) Chang, H.; Lee, Y. Y.; Lee, H. E.; Ahn, H.-Y.; Ko, E.; Nam, K. T.; Jeong, D. H. Size-Controllable and Uniform Gold Bumpy Nanocubes for Single-Particle-Level Surface-Enhanced Raman Scattering Sensitivity. *Phys. Chem. Chem. Phys.* **2019**, *21* (18), 9044–9051. https://doi.org/10.1039/C9CP00138G.

(128) Lee, Y. Y.; Cho, N. H.; Im, S. W.; Lee, H.; Ahn, H.; Nam, K. T. Chiral 432 Helicoid II Nanoparticle Synthesized with Glutathione and Poly(T) 20 Nucleotide. *ChemNanoMat* **2020**, *6* (3), 362–367.

https://doi.org/10.1002/cnma.201900709.

(129) Kim, H.; Im, S. W.; Cho, N. H.; Seo, D. H.; Kim, R. M.; Lim, Y.; Lee, H.; Ahn, H.; Nam, K. T. Γ-Glutamylcysteine- and Cysteinylglycine-Directed Growth of Chiral Gold Nanoparticles and Their Crystallographic Analysis. *Angew. Chemie Int. Ed.* **2020**, *59* (31), 12976–12983. https://doi.org/10.1002/anie.202003760.

(130) Ocko, B. M.; Watson, G. M.; Wang, J. Structure and Electrocompression of Electrodeposited Iodine Monolayers on Gold (111). *J. Phys. Chem.* **1994**, *98* (3), 897–906. https://doi.org/10.1021/j100054a026.

(131) Lu, S. C. Glutathione Synthesis. *Biochim. Biophys. Acta - Gen. Subj.* **2013**, *1830* (5), 3143–3153. https://doi.org/10.1016/j.bbagen.2012.09.008.

(132) Gervais, C.; Hulliger, J. Impact of Surface Symmetry on Growth-Induced Properties. *Cryst. Growth Des.* **2007**, *7* (10), 1925–1935. https://doi.org/10.1021/cg0608054.

(133) Lee, H.-E.; Kim, R. M.; Ahn, H.-Y.; Lee, Y. Y.; Byun, G. H.; Im, S. W.; Mun, J.; Rho, J.; Nam, K. T. Cysteine-Encoded Chirality Evolution in Plasmonic Rhombic Dodecahedral Gold Nanoparticles. *Nat. Commun.* **2020**, *11* (1), 263. https://doi.org/10.1038/s41467-019-14117-x.

(134) Arago, F. J. D. *Memoires de La Classe Des Sciences Mathematiques et Physiques de l'Institut Imperial de France*; Didot, Paris, France, 1811.

(135) Syubaev, S.; Porfirev, A.; Zhizhchenko, A.; Vitrik, O.; Kudryashov, S.; Fomchenkov, S.; Khonina, S.; Kuchmizhak, A. Zero-Orbital-Angular-

Momentum Laser Printing of Chiral Nanoneedles. *Opt. Lett.* **2017**, *42* (23), 5022. https://doi.org/10.1364/OL.42.005022.

(136) Fan, J.; Kotov, N. A. Chiral Nanoceramics. *Adv. Mater.* **2020**, 1906738. https://doi.org/10.1002/adma.201906738.

(137) Yeom, J.; Santos, U. S.; Chekini, M.; Cha, M.; de Moura, A. F.; Kotov, N. A. Chiromagnetic Nanoparticles and Gels. *Science* **2018**, *359* (6373), 309–314. https://doi.org/10.1126/science.aao7172.

(138) Li, Y.; Cheng, J.; Li, J.; Zhu, X.; He, T.; Chen, R.; Tang, Z. Tunable Chiroptical Properties from the Plasmonic Band to Metal-Ligand Charge Transfer Band of Cysteine-Capped Molybdenum Oxide Nanoparticles. *Angew. Chemie* **2018**, *130* (32), 10393–10397. https://doi.org/10.1002/ange.201806093.

(139) Purcell-Milton, F.; McKenna, R.; Brennan, L. J.; Cullen, C. P.; Guillemeney, L.; Tepliakov, N. V.; Baimuratov, A. S.; Rukhlenko, I. D.; Perova, T. S.; Duesberg, G. S.; Baranov, A. V.; Fedorov, A. V.; Gun'ko, Y. K. Induction of Chirality in Two-Dimensional Nanomaterials: Chiral 2D MoS 2 Nanostructures. *ACS Nano* **2018**, *12* (2), 954–964. https://doi.org/10.1021/acsnano.7b06691.

(140) Jiang, S.; Chekini, M.; Qu, Z.-B.; Wang, Y.; Yeltik, A.; Liu, Y.; Kotlyar, A.; Zhang, T.; Li, B.; Demir, H. V.; Kotov, N. A. Chiral Ceramic Nanoparticles and Peptide Catalysis. *J. Am. Chem. Soc.* **2017**, *139* (39), 13701–13712. https://doi.org/10.1021/jacs.7b01445.

(141) Han, B.; Zhu, Z.; Li, Z.; Zhang, W.; Tang, Z. Conformation Modulated

Optical Activity Enhancement in Chiral Cysteine and Au Nanorod Assemblies. *J. Am. Chem. Soc.* **2014**, *136* (46), 16104–16107. https://doi.org/10.1021/ja506790w.

(142) Zhu, Z.; Liu, W.; Li, Z.; Han, B.; Zhou, Y.; Gao, Y.; Tang, Z. Manipulation of Collective Optical Activity in One-Dimensional Plasmonic Assembly. *ACS Nano* **2012**, *6* (3), 2326–2332. https://doi.org/10.1021/nn2044802.

(143) Zhu, F.; Li, X.; Li, Y.; Yan, M.; Liu, S. Enantioselective Circular Dichroism Sensing of Cysteine and Glutathione with Gold Nanorods. *Anal. Chem.* **2015**, *87* (1), 357–361. https://doi.org/10.1021/ac504017f.

(144) Lu, J.; Chang, Y.-X.; Zhang, N.-N.; Wei, Y.; Li, A.-J.; Tai, J.; Xue, Y.; Wang, Z.-Y.; Yang, Y.; Zhao, L.; Lu, Z.-Y.; Liu, K. Chiral Plasmonic Nanochains via the Self-Assembly of Gold Nanorods and Helical Glutathione Oligomers Facilitated by Cetyltrimethylammonium Bromide Micelles. *ACS Nano* **2017**, *11* (4), 3463–3475. https://doi.org/10.1021/acsnano.6b07697.

(145) Fu, X.; Wang, Y.; Huang, L.; Sha, Y.; Gui, L.; Lai, L.; Tang, Y. Assemblies of Metal Nanoparticles and Self-Assembled Peptide Fibrils—Formation of Double Helical and Single-Chain Arrays of Metal Nanoparticles. *Adv. Mater.* **2003**, *15* (11), 902–906. https://doi.org/10.1002/adma.200304624.

(146) Lee, J.; Huh, J.-H.; Kim, K.; Lee, S. DNA Origami-Guided Assembly of the Roundest 60-100 Nm Gold Nanospheres into Plasmonic Metamolecules. *Adv. Funct. Mater.* **2018**, *28* (15), 1707309. https://doi.org/10.1002/adfm.201707309.

(147) Schilthuizen, M.; Davison, A. The Convoluted Evolution of Snail Chirality. *Naturwissenschaften* **2005**, *92* (11), 504–515. https://doi.org/10.1007/s00114-05-0045-2.

(148) Schaaff, T. G.; Whetten, R. L. Giant Gold−Glutathione Cluster Compounds: Intense Optical Activity in Metal-Based Transitions. *J. Phys. Chem. B* **2002**, *104* (12), 2630–2641. https://doi.org/10.1021/jp993691y.

(149) Moloney, M. P.; Gun'ko, Y. K.; Kelly, J. M. Chiral Highly Luminescent CdS Quantum Dots. *Chem. Commun.* **2007**, *7345* (38), 3900. https://doi.org/10.1039/b704636g.

(150) Nakashima, T.; Kobayashi, Y.; Kawai, T. Optical Activity and Chiral Memory of Thiol-Capped CdTe Nanocrystals. *J. Am. Chem. Soc.* **2009**, *131* (30), 10342–10343. https://doi.org/10.1021/ja902800f.

(151) Ma, W.; Xu, L.; De Moura, A. F.; Wu, X.; Kuang, H.; Xu, C.; Kotov, N. A. Chiral Inorganic Nanostructures. *Chem. Rev.* **2017**, *117* (12), 8041–8093. https://doi.org/10.1021/acs.chemrev.6b00755.

(152) Kim, H.; Im, S. W.; Kim, R. M.; Cho, N. H.; Lee, H.-E.; Ahn, H.-Y.; Nam, K. T. Chirality Control of Inorganic Materials and Metals by Peptides or Amino Acids. *Mater. Adv.* **2020**, *1* (4), 512–524. https://doi.org/10.1039/D0MA00125B.

(153) Lee, J.; Choe, I. R.; Kim, Y.-O.; Namgung, S. D.; Jin, K.; Ahn, H.-Y.; Sung, T.; Kwon, J.-Y.; Lee, Y.-S.; Nam, K. T. Proton Conduction in a Tyrosine-Rich Peptide/Manganese Oxide Hybrid Nanofilm. *Adv. Funct. Mater.* **2017**, *27* (35), 1702185. https://doi.org/10.1002/adfm.201702185.

(154) Lee, J.; Ju, M.; Cho, O. H.; Kim, Y.; Nam, K. T. Tyrosine-Rich Peptides as a Platform for Assembly and Material Synthesis. *Adv. Sci.* **2019**, *6* (4), 1801255. https://doi.org/10.1002/advs.201801255.

(155) Cherny, I.; Gazit, E. Amyloids: Not Only Pathological Agents but Also Ordered Nanomaterials. *Angew. Chemie Int. Ed.* **2008**, *47* (22), 4062–4069. https://doi.org/10.1002/anie.200703133.

(156) Wei, G.; Su, Z.; Reynolds, N. P.; Arosio, P.; Hamley, I. W.; Gazit, E.; Mezzenga, R. Self-Assembling Peptide and Protein Amyloids: From Structure to Tailored Function in Nanotechnology. *Chem. Soc. Rev.* **2017**, *46* (15), 4661–4708. https://doi.org/10.1039/C6CS00542J.

(157) Hamill, S. J.; Cota, E.; Chothia, C.; Clarke, J. Conservation of Folding and Stability within a Protein Family: The Tyrosine Corner as an Evolutionary Cul-de-Sac 1 1Edited by J. M. Thornton. *J. Mol. Biol.* **2000**, *295* (3), 641–649. https://doi.org/10.1006/jmbi.1999.3360.

(158) McConnell, I.; Li, G.; Brudvig, G. W. Energy Conversion in Natural and Artificial Photosynthesis. *Chem. Biol.* **2010**, *17* (5), 434–447. https://doi.org/10.1016/j.chembiol.2010.05.005.

(159) Sevier, C. S.; Kaiser, C. A. Formation and Transfer of Disulphide Bonds in Living Cells. *Nat. Rev. Mol. Cell Biol.* **2002**, *3* (11), 836–847. https://doi.org/10.1038/nrm954.

(160) Jang, H.-S.; Lee, J.-H.; Park, Y.-S.; Kim, Y.-O.; Park, J.; Yang, T.-Y.; Jin, K.; Lee, J.; Park, S.; You, J. M.; Jeong, K.-W.; Shin, A.; Oh, I.-S.; Kwon, M.-K.; Kim, Y.-I.; Cho, H.-H.; Han, H. N.; Kim, Y.; Chang, Y. H.; Paik, S.

R.; Nam, K. T.; Lee, Y.-S. Tyrosine-Mediated Two-Dimensional Peptide Assembly and Its Role as a Bio-Inspired Catalytic Scaffold. *Nat. Commun.* **2014**, *5* (1), 3665. https://doi.org/10.1038/ncomms4665.

(161) Kim, H.; Bang, K.-M.; Ha, H.; Cho, N. H.; Namgung, S. D.; Im, S. W.; Cho, K. H.; Kim, R. M.; Choi, W. Il; Lim, Y.-C.; Shin, J.-Y.; Song, H. K.; Kim, N.-K.; Nam, K. T. Tyrosyltyrosylcysteine-Directed Synthesis of Chiral Cobalt Oxide Nanoparticles and Peptide Conformation Analysis. *ACS Nano* **2021**, *15* (1), 979–988. https://doi.org/10.1021/acsnano.0c07655.

(162) Engel, J.; Liehl, E.; Sorg, C. Circular Dichroism, Optical Rotatory Dispersion and Helix Coil Transition of Polytyrosine and Tyrosine Peptides in Non-Aqueous Solvents. *Eur. J. Biochem.* **1971**, *21* (1), 22–30. https://doi.org/10.1111/j.1432-1033.1971.tb01435.x.

(163) Antosiewicz, J. M.; Shugar, D. UV–Vis Spectroscopy of Tyrosine Side-Groups in Studies of Protein Structure. Part 1: Basic Principles and Properties of Tyrosine Chromophore. *Biophys. Rev.* **2016**, *8* (2), 151–161. https://doi.org/10.1007/s12551-016-0198-6.

(164) Alrehaily, L. M.; Joseph, J. M.; Biesinger, M. C.; Guzonas, D. A.; Wren, J. C. Gamma-Radiolysis-Assisted Cobalt Oxide Nanoparticle Formation. *Phys. Chem. Chem. Phys.* **2013**, *15* (3), 1014–1024. https://doi.org/10.1039/C2CP43094K.

(165) Gu, F.; Li, C.; Hu, Y.; Zhang, L. Synthesis and Optical Characterization of Co3O4 Nanocrystals. *J. Cryst. Growth* **2007**, *304* (2), 369–373. https://doi.org/10.1016/j.jcrysgro.2007.03.040.

(166) Sivo, V.; D'Abrosca, G.; Russo, L.; Iacovino, R.; Pedone, P. V.; Fattorusso, R.; Isernia, C.; Malgieri, G. Co(II) Coordination in Prokaryotic Zinc Finger Domains as Revealed by UV-Vis Spectroscopy. *Bioinorg. Chem. Appl.* **2017**, *2017*, 1–7. https://doi.org/10.1155/2017/1527247.

(167) May, Sheldon W., and J.-Y. K. Preparation and Properties of Cobalt (II) Rubredoxin. *Biochemistry* **1978**, *17* (16), 3333–3338.

(168) Nitsche, C.; Otting, G. Pseudocontact Shifts in Biomolecular NMR Using Paramagnetic Metal Tags. *Prog. Nucl. Magn. Reson. Spectrosc.* **2017**, *98–99*, 20–49. https://doi.org/10.1016/j.pnmrs.2016.11.001.

(169) Cavins, J. F.; Krull, L. H.; Friedman, M.; Gibbs, D. E.; Inglett, G. E. Spectrophotometric Cysteine Analysis. *J. Agric. Food Chem.* **1972**, *20* (6), 1124–1126. https://doi.org/10.1021/jf60184a026.

(170) Werth, M. T., Tang, S. F., Formicka, G., Zeppezauer, M., & Johnson, M. K. Magnetic Circular Dichroism and Electron Paramagnetic Resonance Studies of Cobalt-Substituted Horse Liver Alcohol Dehydrogenase. *Inorg. Chem.* **1995**, *34* (1), 218–228.

(171) BERGMAN, T.; JORNVALL, H.; HOLMQUIST, B.; VALLEE, B. L. A Synthetic Peptide Encompassing the Binding Site of the Second Zinc Atom (the "structural" Zinc) of Alcohol Dehydrogenase. *Eur. J. Biochem.* **1992**, *205* (2), 467–470. https://doi.org/10.1111/j.1432-1033.1992.tb16802.x.

(172) Xu, H.; Zeng, H. C. Self-Generation of Tiered Surfactant Superstructures for One-Pot Synthesis of Co 3O 4 Nanocubes and Their Close-and Non-Close-Packed Organizations. *Langmuir* **2004**, *20* (22), 9780–9790.

https://doi.org/10.1021/la049164.

(173) George, G.; Anandhan, S. A Comparative Study on the Physico–Chemical Properties of Sol–Gel Electrospun Cobalt Oxide Nanofibres from Two Different Polymeric Binders. *RSC Adv.* **2015**, *5* (99), 81429–81437. https://doi.org/10.1039/C5RA11135H.

(174) Yoo, S.; Cho, M.; Park, Q.-H. Globally Enhanced Chiral Field Generation by Negative-Index Metamaterials. *Phys. Rev. B* **2014**, *89* (16), 161405. https://doi.org/10.1103/PhysRevB.89.161405.

(175) Schäferling, M.; Dregely, D.; Hentschel, M.; Giessen, H. Tailoring Enhanced Optical Chirality: Design Principles for Chiral Plasmonic Nanostructures. *Phys. Rev. X* **2012**, *2* (3), 031010. https://doi.org/10.1103/PhysRevX.2.031010.

(176) Mohammadi, E.; Tsakmakidis, K. L.; Askarpour, A. N.; Dehkhoda, P.; Tavakoli, A.; Altug, H. Nanophotonic Platforms for Enhanced Chiral Sensing. *ACS Photonics* **2018**, *5* (7), 2669–2675. https://doi.org/10.1021/acsphotonics.8b00270.

(177) Rafiei Miandashti, A.; Khosravi Khorashad, L.; Kordesch, M. E.; Govorov, A. O.; Richardson, H. H. Experimental and Theoretical Observation of Photothermal Chirality in Gold Nanoparticle Helicoids. *ACS Nano* **2020**, *14* (4), 4188–4195. https://doi.org/10.1021/acsnano.9b09062.

(178) Lee, H.-E.; Kim, R. M.; Ahn, H.-Y.; Lee, Y. Y.; Byun, G. H.; Im, S. W.; Mun, J.; Rho, J.; Nam, K. T. Cysteine-Encoded Chirality Evolution in Plasmonic Rhombic Dodecahedral Gold Nanoparticles. *Nat. Commun.*

2020, *11* (1), 263. https://doi.org/10.1038/s41467-019-14117-x.

(179) González-Rubio, G.; Mosquera, J.; Kumar, V.; Pedrazo-Tardajos, A.; Llombart, P.; Solís, D. M.; Lobato, I.; Noya, E. G.; Guerrero-Martínez, A.; Taboada, J. M.; Obelleiro, F.; MacDowell, L. G.; Bals, S.; Liz-Marzán, L. M. Micelle-Directed Chiral Seeded Growth on Anisotropic Gold Nanocrystals. *Science* **2020**, *368* (6498), 1472–1477. https://doi.org/10.1126/science.aba0980.

(180) Merg, A. D.; Boatz, J. C.; Mandal, A.; Zhao, G.; Mokashi-Punekar, S.; Liu, C.; Wang, X.; Zhang, P.; Van Der Wel, P. C. A.; Rosi, N. L. Peptide-Directed Assembly of Single-Helical Gold Nanoparticle Superstructures Exhibiting Intense Chiroptical Activity. *J. Am. Chem. Soc.* **2016**, *138* (41), 13655–13663. https://doi.org/10.1021/jacs.6b07322.

(181) Lu, J.; Xue, Y.; Bernardino, K.; Zhang, N.-N.; Gomes, W. R.; Ramesar, N. S.; Liu, S.; Hu, Z.; Sun, T.; de Moura, A. F.; Kotov, N. A.; Liu, K. Enhanced Optical Asymmetry in Supramolecular Chiroplasmonic Assemblies with Long-Range Order. *Science* **2021**, *371* (6536), 1368–1374. https://doi.org/10.1126/science.abd8576.

(182) Kim, M.; Kwon, H.; Lee, S.; Yoon, S. Effect of Nanogap Morphology on Plasmon Coupling. *ACS Nano* **2019**, *13* (10), 12100–12108. https://doi.org/10.1021/acsnano.9b06492.

(183) Khlopin, D.; Laux, F.; Wardley, W. P.; Martin, J.; Wurtz, G. A.; Plain, J.; Bonod, N.; Zayats, A. V.; Dickson, W.; Gérard, D. Lattice Modes and Plasmonic Linewidth Engineering in Gold and Aluminum Nanoparticle Arrays. *J. Opt. Soc. Am. B* **2017**, *34* (3), 691.

https://doi.org/10.1364/JOSAB.34.000691.

(184) Moreau, A.; Ciracì, C.; Mock, J. J.; Hill, R. T.; Wang, Q.; Wiley, B. J.; Chilkoti, A.; Smith, D. R. Controlled-Reflectance Surfaces with Film-Coupled Colloidal Nanoantennas. *Nature* **2012**, *492* (7427), 86–89. https://doi.org/10.1038/nature11615.

초 록

카이랄 메타 물질은 뛰어난 광 물질 상호 작용으로 인하여 나노 광자 분야에서 큰 관심을 받아왔다. 다년간의 연구를 통하여 최첨단 리소그래피 기술과 분자 조립 스캐폴드를 사용하여 카이랄 나노구조가 제작되어 왔다. 기하학적 비대칭성을 지니는 카이랄 무기 금속 나노 물질은 대칭성을 가지는 나노 물질에서 얻을 수 없었던 독특한 물리적 현상을 나타낼 수 있다. 카이랄 나노 구조는 음의 굴절률, 분자 감지 및 광대역 원형 편광과 같은 광학적 효과를 나타내기 위해 사용될 수 있다. 이러한 카이랄 메타 물질의 뛰어난 광학 특성을 실제 장치에 통합하기 위해서는 섬세하게 설계된 광학적 성질을 가지는 카이랄 구조를 달성하는 것이 필요하다. 그러나 고가의 제조비용 및 설비, 복잡한 제조 과정 및 제한된 해상도로 인해 카이랄 메타 물질을 실제 장치로 통합하는 데 제한이 있어왔다. 이러한 한계를 극복하기 위해서는 카이랄 나노 구조 제어를 위한 유연한 방법론을 개발하는 것이 요구된다. 본 학위 연구 에서는 펩타이드를 이용한 나노 입자 형태의 다양화와 나노 구조에서의 플라즈몬 커플링을 이용한 광학적 반응의 추가적인 조절이 앞서 언급한 한계를 해결하기 위한 유망한 대안이 될 수 있음을 제안한다. 본 학위 논문은 카이랄 나노 구조의 발달에 대한 이해와 조절을 통해 플라즈몬 커플링을 이용하여 카이랄 광학 응답을 조절할 수 있는 플랫폼을 제시한다.

생체분자를 이용한 플라즈몬 나노 입자의 콜로이드 합성에 대한 최근 연구결과는 합성 과정에 관여하는 카이랄성 인코더인 분자를 변경함으로써 새로운 형태와 광학적 특성을 가진 나노입자를 합성할 수 있음을 시사한다. 또한 단일 플라즈몬 입자의 광학 응답은 플라즈몬 커플링을 사용하여 증폭되고 민감하게 변조될 수 있다. 여러 플라즈몬 나노 입자가 인접할 경우, 입자

공명의 혼성화가 유도되어 공명을 크게 변화시킨다. 플라즈몬 나노 구조의 형태와 카이랄성을 제어하기 위한 새로운 전략을 수립하기 위하여, 우리는 먼저 생체분자에 의해 유도되는 무기 카이랄성에 초점을 맞추었다. 무기 표면에서의 원자 왜곡 또는 거시적 재구성을 통한 카이랄성의 진화에 대한 기존 연구는 카이랄 나노 구조 제어를 위한 새로운 전략 수립에 중요한 통찰력을 제공한다. 본 학위논문에서는 카이랄 광학 반응의 이해와 조절을 단일 나노 입자와 시스템적 제어의 두 가지 관점에서 소개한다.

나노 재료 공학의 발전으로 나노 규모에서 정확한 형태학적 제어가 가능한 콜로이드 합성 방법이 개발되었다. 다양한 할로겐화물 이온, 금속 이온 및 유기 분자를 흡착제로 사용하면 특정 Miller 지수로 결정면을 부동태화하여 결정면과 나노입자 형태를 손쉽게 제어할 수 있다. 또한 종자 매개 방법은 높은 Miller-index 결정면을 높은 균일도로 생성할 수 있으므로 나노 입자의 형태를 제어하는 중요한 전략으로 사용된다. 우리는 합성에 첨가하는 유기 분자를 변경하여 금 나노 입자의 성장 및 카이랄성 진화에 대한 광범위한 이해를 제공한다. 이를 위하여 γ-글루타밀시스테인(γ-Glu-Cys) 및 시스테이닐글리신(Cys-Gly) 을 사용하여 합성된 금 나노 입자의 성장 경로와 키랄성 진화가 결정학적 관점에서 분석되었다. γ-Glu-Cys 을 이용하여 합성된 금 나노 입자의 경우 돌출된 카이랄 날개를 가지는 정육면체 구조로 발달한다. 반면에, Cys-Gly 을 이용하여 합성된 나노입자의 경우 타원형의 공동 구조를 가진 마름모꼴 12 면체로 발달하며, 이로 인해 두 나노 입자는 서로 다른 카이랄 광학 반응을 보인다. 시간에 따른 나노 입자의 성장 분석을 통해 γ-Glu-Cys 와 Cys-Gly 가 서로 다른 중간 형태를 지니며 생성한다는 것을 알 수 있었다. γ-Glu-Cys 는 오목한 육팔면체 모양의 중간체를 유도하는 반면 Cys-Gly 는 오목한 마름모꼴 십이면체의 중간체를 보인다. 이러한 결과는 펩타이드와 금 표면 간의 상호 작용을 이해함으로써 카이랄 구조와 그에 따른 광학 반응을 조절할 수 있음을 시사한다.

생체 분자를 이용한 카이랄 나노구조의 합성은 주로 플라즈몬 물질에서 연구되어 왔지만, 촉매 활성을 지녀 카이랄 촉매로 사용될 수 있는 카이랄 금속 산화물을 합성하려는 시도 또한 카이랄 물질의 응용 확대를 위한 새로운 방향으로 제시되고 있다. 생체 분자를 이용한 카이랄 금속 산화물 합성에서의 기존 연구는 단일 아미노산에 국한되어 있지만, 카이랄성 발달을 이해하고 확장 가능한 합성 전략을 수립하기 위해서는 펩타이드로의 서열 확장이 요구된다. 본 연구에서는 Tyr-Tyr-Cys 펩타이드를 서열확장을 위한 리간드로 선택하여, 코발트 산화물에서 펩타이드를 이용한 카이랄성 발현을 탐구하였다. 펩타이드 리간드를 이용하여 합성된 카이랄 코발트 산화물 나노 입자는 자외선 및 가시광선 영역에서 0.01 의 뛰어난 비대칭 인자를 나타냈다. 또한, 2D NMR 분광 분석을 통해 나노 입자 표면의 펩타이드 리간드의 3 차원 입체구조를 규명하였다. 또한 펩타이드 리간드의 시퀀스에 따른 카이랄 코발트 산화물 나노 입자의 발달을 분석하여 Tyr-Tyr-Cys 리간드의 싸이올 그룹과 카복실 그룹이 카이랄성 발달에 중요한 역할을 담당함을 규명하였다. 본 연구 결과는 무기 결정에 카이랄성을 발현하는 펩타이드의 역할이 상호 작용하는 물질에 따라 달라질 수 있으며, 카이랄 광학 특성의 변화를 야기할 수 있음을 시사한다.

단일 플라즈몬 나노 입자의 광학 신호는 플라즈몬 커플링을 통하여 증폭되고 민감하게 제어될 수 있다. 여러 개의 플라즈몬 나노 입자가 인접할 경우, 입자 공명의 혼성화가 일어나 공명을 크게 변화시킨다. 이러한 맥락에서, 본 연구에서는 플라즈몬 커플링을 카이랄 플라즈몬 나노 입자에 적용하여 카이랄 광학 특성을 제어하고자 하였다. 이를 위하여 카이랄 금 나노 입자를 기판에 코팅하고 나노 크기의 플라즈몬 금속 층을 증착하여 메타 물질을 제작하였다. 플라즈몬 결합으로 인한 광학 특성의 변화는 투과 기반 및 확산 반사 기반 원편광 이색성 (cirular dichroism, CD) 분광법을 통해 분석되었다. 카이랄 금속 나노 입자 기반 메타 물질의 광학적 분석을 통해 CD

스펙트럼의 피크 위치, 세기 및 부호가 플라즈몬 커플링에 의해 변화함을 알 수 있었다. 또한, 플라즈몬 커플링에 의해 생성된 모드는 나노구조체의 크기, 거리 및 주변 굴절률에 따라 크게 변화하였다. 더 나아가, 카이랄 금 나노입자에 실리카 쉘의 플라즈몬 나노입자의 광학 특성 및 안정성의 제어가 가능함을 규명하였다.

본 학위 연구에서는 나노 입자의 카이랄성 발달에 펩타이드 리간드가 미치는 역할을 이해함으로써 단일 나노 입자 수준에서 CD 신호의 제어를 달성하였다. 또한 플라즈몬 커플링을 사용하여 카이랄 나노 구조의 광학적 특성을 조절하는 방법론이 확립되었다. 본 연구를 통하여 개발된 카이랄 나노 구조에서 광학 특성의 조절을 위한 방법론은 카이랄 메타 물질을 실용적인 광학 장치로 통합하는 것을 용이하게 할 것으로 기대된다.

주요어: 원편광 이색성, 플라즈몬 커플링, 펩타이드, 금 나노입자, 코발트 산화물, 나노 구조 제어

학번: 2018-38618